Inorganic Nanoparticles for Functional Coating Applications

Von der Naturwissenschaftlichen Fakultät der
Gottfried Wilhelm Leibniz Universität Hannover
zur Erlangung des Grades

Doktor der Naturwissenschaften
Dr. rer. nat.

genehmigte Dissertation
von

Dipl.-Chem. Florian Waltz

geboren am 19.01.1983 in Hildesheim

2012

Referent: Prof. Dr. Peter Behrens

Korreferent: Prof. Dr. Franz Renz

Tag der Promotion: 05.10.2012

Danksagung

Nun, am Ende meiner Doktorarbeit schaue ich rückblickend auf mein Studium, und stelle fest, dass ich an dieser Stelle einer Menge Leute danken möchte, ohne die all dies nicht möglich gewesen wäre.

Zu allererst ist hier natürlich Herr Prof. Dr. Behrens zu nennen, der mich in seinen Arbeitskreis aufgenommen hat, und der mir ein sehr abwechslungsreiches, vor allem aber auch spannendes Aufgabenfeld übertrug. Herrn Prof. Dr. Renz und Herrn Prof. Dr. Buhl möchte ich für die Übernahme des Koreferats bzw. der Drittprüferschaft danken.

An dieser Stelle möchte ich meinen Kooperationspartnern, ohne die ich diese Arbeit niemals hätte anfertigen können, danken, auch für die tolle Atmosphäre. Dies sind aus dem VWS-Projekt Mark A. Swider und Dr. Thomas Hassel, mit denen ich nicht nur mehrere Tagungen verbringen durfte, sondern in deren Maschinenhallen ich mich auch immer willkommen gefühlt habe.

Vergessen werde ich in diesem Zusammenhang auch nicht unsere Fahrten zum Suspensionsplasmaspritzen nach Witten – ein großes Dankeschön an Martin Erne für die Gastlichkeit im „Bunker".

Abwechslung in meinen Uni-Alltag brachte unsere Kooperation mit BTS. Für die exzellente Zusammenarbeit, den konstruktiven Gedankenaustausch und die stets gute Stimmung bei unseren Projekttreffen möchte ich Prof. Dr. Peter Behrens, Priv.-Doz. Dr. Stefanie Eiden, Dr. Andreas M. Schneider, Hans-Christoph Schwarz und Robert Zahn danken.

Die Arbeitsatmosphäre während meiner Promotion kann ich nur als ausgezeichnet bezeichnen. Mein ganz besonderer Dank gilt daher den ehemaligen und aktuellen Mitgliedern des Arbeitskreises Behrens, die für mich enge Freunde denn bloße Mitarbeiter waren. Ich kann mir auch kaum vorstellen, dass die Zusammenarbeit auf engstem Raum damals in Lab 7 so reibungslos mit Anderen verlaufen wäre. Gerne denke ich auch an unsere gemeinsamen Ausflüge, Boßeltouren, Videoabende, Kanufahrten, Grillfeste oder auch an die Kaffeepausen zurück. Daher kann ich nur hoffen, irgendwann wieder auch nur halb so gute Kollegen zu haben. Vielen Dank Leute! Unvergessen, vor allem in den Knochen, bleiben mir auch unsere Trainings-Einheiten/Kaffeekränzchen mit „Team Muskel(kater)". Life's a

glitch, oder auch nicht – vollkommen egal, die kurzen Pausen bei Hans im Labor waren mir immer eine willkommene Ablenkung.

Natürlich möchte ich mich auch bei meinen präparativen Helfern, meinen Hiwis bedanken. Die nun folgende Liste führt hoffentlich nicht zur Annahme dass ich einen unangemessen hohen Verschleiß derer hatte – vielmehr gab es genügend zu tun: Robert Zahn, Jan Hartwig, David Käter, Viktor Sauer, Kim-Dana Kreisköther und Niklas Burblies.

Für zahllose Orthographie- und Stil-Korrekturen an dieser Arbeit möchte ich Janosch Cravillon und vor allem Julia Sürth danken – ohne die beiden sähen die folgenden Seiten wohl doch etwas anders aus.

Selbstverständlich werde ich auch nicht die Zeit vor der Doktorarbeit vergessen. Dass das Studium die beste Zeit meines Lebens war und dass ich immer irgendwann erfahren habe, wann wichtige Termine anstehen oder man sich für etwas anmelden muss, verdanke ich meinen Kommilitonen Caroline Behrens, Janosch Cravillon, Georg Platz, Jens Wegner, Andreas Kipke, Melanie Minnermann, Clarissa Baumanis und Thomas Schmidt (Catzy). Schade, dass unser gemeinsames „Fremdessen" am Mittwoch jetzt, da alle fertig werden, ausstirbt.

Während des Studiums war die wohl ungewöhnlichste Wohngemeinschaft, zusammen mit Christian Berner und Hendrik Busche, mein Zuhause. Vielen Dank Jungs für unsere gemeinsame Zeit in der TKS7.

Vielen Dank auch an Julia Sürth, für die gemeinsame Zeit und die Unterstützung in jeder Lebenslage.

Ich weiß schon jetzt, dass die Danksagung wohl der einzige Teil dieser Arbeit sein wird, den die Menschen, denen sie an dieser Stelle gewidmet ist, lesen werden. Dementsprechend schwer fällt es mir nun, die passenden Worte zu finden. Ein einfaches Dankeschön würde wohl der Unterstützung meiner Familie bestehend aus Sieglinde, Heinz, Beate, Jürgen, Christin, Dirk, Susanne, Jannis und Julia nicht gerecht werden. Euch unendlichen Dank für die Unterstützung zeitlebens – und schaut euch ruhig auch die folgenden Seiten an.

Abstract

The present work addresses the syntheses and application of inorganic nanoparticles as constituents of functional surfaces which are used for different purposes. It contains three original research articles of which I am the first author. The first paper encompasses the development of stable suspensions of nanocrystalline magnesium fluoride (MgF$_2$) and their use as liquid feedstock in a plasma-based deposition process which is part of a hybrid joining and coating process. MgF$_2$ coatings are applied to welded seams of the magnesium alloy AZ31 in order to enhance their corrosion resistance. The newly developed hybrid tool, constructed by the project partners from the Institut für Werkstoffkunde of the Leibniz University of Hannover, consists of a tungsten inert gas (TIG) welder and a suspension plasma sprayer (SPS) for subsequent coating. In a first step, we synthesized MgF$_2$ nanoparticles with particle sizes below 10 nm via a polyol-mediated approach and have then formulated these as aqueous suspensions. This approach was scaled up to supply sufficient amount of suspension for conducting initial hybrid joining and coating tests. Coatings of MgF$_2$ on welded seams were characterized and the corrosion resistances were evaluated by potentiodynamic polarization measurements. The results show that the hybrid SPS/TIG process employing MgF$_2$ nanoparticle suspensions could remarkably enhance the corrosion resistance of magnesium joints. Two articles attend to the issue of morphology control in the formation of zinc oxide (ZnO) particles and films via wet-chemical approaches with the assistance of natural polysaccharides (PS). This investigation was motivated by the high potential of doped ZnO in transparent conductive films. General aspects of the influence of the PSs hyaluronic acid and chondroitin-6-sulfate were examined in precipitation experiments. The addition of PSs led to the formation of highly symmetric ZnO mesocrystals with different morphologies. A mechanistic model for their formation was developed. The findings derived from the precipitation study were then used to tailor the morphology of ZnO films grown via chemical bath deposition. By systematic addition of hyaluronic acid to the bath solution, the film morphology and hence the optical and electrical properties could be tailored. Optimized ZnO films display excellent electrical (photo-) conductivities and very good transparencies. This work shows that careful chemical preparation of nanoparticles can result in functional coatings with very different properties which are well adapted to the applications aimed at.

Keywords: functional coatings; zinc oxide; magnesium fluoride; corrosion; magnesium; mesocrystals; polysaccharides; transparent conductive films.

Kurzzusammenfassung

Die vorliegende Arbeit befasst sich mit der Synthese von anorganischen Nanopartikeln und ihrer Applikation zur Herstellung funktionaler Oberflächen für unterschiedliche Einsatzzwecke. Die Dissertation basiert auf drei meiner Publikationen als Erstautor. Hierbei thematisiert die erste Publikation die Entwicklung stabiler Suspensionen von nanokristallinem Magnesiumfluorid (MgF_2) und deren Verwendung in einem plasmabasiertem Abscheidungsprozess, der wiederum Teil eines kombinierten Schweiß- und Beschichtungsverfahrens ist. Dabei werden MgF_2-Beschichtungen auf Schweißnähten der Magnesiumlegierung AZ31 aufgebracht um deren Korrosionsbeständigkeit zu verbessern. Das neu entwickelte Hybridgerät wurde von unseren Projektpartnern aus dem Institut für Werkstoffkunde der Leibniz Universität Hannover konstruiert, und besteht aus einem Wolfram-Inertgas-(WIG)-Schweißgerät und einem Suspensionsplasmaspritzer (SPS) zum anschließenden Beschichten. Wir haben in einem ersten Schritt MgF_2 Nanopartikel mit einer Partikelgröße von unter 10 nm mittels einer polyol-geführten Synthese hergestellt und daraus anschließend wässrige Suspensionen formuliert. Dieser Ansatz wurde hochskaliert um ausreichende Mengen an Suspension für erste kombinierte Schweiß- und Beschichtungsversuche zur Verfügung zu stellen. Die so produzierten MgF_2-Beschichtungen auf den Schweißnähten wurden charakterisiert und deren Korrosionsbeständigkeit evaluiert. Die Ergebnisse zeigen, dass das kombinierte SPS/WIG-Verfahren unter Verwendung von Suspensionen aus nanokristallinem MgF_2 die Korrosionseigenschaften von Schweißnähten beachtlich verbessern kann. Zwei weitere Publikationen befassen sich mit der Kontrolle der Morphologie von Zinkoxid-(ZnO)-Nanopartikeln und -Filmen über nasschemische Ansätze durch die Zugabe natürlicher Polysaccharide (PSe). Diese Untersuchung wurde motiviert durch das hohe Anwendungspotential von dotiertem ZnO als transparenter, leitfähiger Film. In Präzipitationsversuchen wurden generelle Aspekte der Einflüsse der PSe Hyaluronsäure und Chondroitin-4-sulfat untersucht. Die Zugabe der PSe führte zur Bildung hochsymmetrischer ZnO-Mesokristalle mit unterschiedlicher Morphologie. Ein mechanistisches Modell der Mesokristallbildung wurde entwickelt. Die daraus resultierenden Ergebnisse wurden eingesetzt, um die Morphologie von ZnO-Filmen, die über chemische Badabscheidung hergestellt wurden, zu beeinflussen. Durch systematische Zugabe von Hyaluronsäure zur Badlösung konnte die Morphologie und damit auch die optischen und elektrischen Eigenschaften der Filme eingestellt werden. Optimierte ZnO-Filme zeigen exzellente (photo-) elektrische

Leitfähigkeiten und sehr gute Tranzparenzen. Diese Arbeit zeigt, dass die sorgsame chemische Präparation von Nanopartikeln zu funktionalisierten Beschichtungen mit sehr unterschiedlichen, für die jeweilige Anwendung angepassten, Eigenschaften führen kann.

Schlagwörter: funktionelle Filme; Zinkoxid; Magnesiumfluorid; Korrosion; Magnesium; Mesokristalle; Polysaccharide; transparente leitfähige Filme.

Erklärung

Hierdurch erkläre ich, dass ich meine Dissertation mit dem Titel „Inorganic Nanoparticles for Functional Coating Applications" selbständig verfasst und die benutzten Hilfsmittel und Quellen sowie gegebenenfalls die zu Hilfeleistung herangezogenen Institutionen vollständig angegeben habe.

Die Dissertation wurde nicht schon als Masterarbeit, Diplomarbeit oder andere Prüfungsarbeit verwendet.

_____

(Florian Waltz)

Table of Content

1 Introduction

A long time has passed since the famous talk of Richard P. Feynman "There's plenty of room at the bottom" which can be considered as the beginning of nanotechnology.[1] In the last two decades a huge variety of nanoparticles and –structures have been developed in laboratories worldwide. However, only very few have emerged in practical applications. Especially in film applications nanotechnology has not yet shown its full potential.

The aim of this work was the deposition of nanostructured coatings and evaluation of their potential. For this purpose, two different but practical systems served as examples: First, nanoparticles were synthesized and then formulated as stable dispersions prior to their deposition on surfaces as dense films. Second, nanostructured films grown via polysaccharide-assisted chemical bath deposition served as support for a subsequent growth of dense films.

The first part of this thesis describes the corrosion protection of magnesium weld seams by coating with nanocrystalline films of MgF_2. Magnesium and magnesium alloys are eminently interesting structural materials for light-weight applications in the automobile as well as in the aerospace sector.[2] Assembly of different magnesium parts with welding techniques usually leads to a conspicuous increase of corrosion. This is mainly caused by the disturbance of the material structure in the heat-affected zone of the weld seam and by the different elemental compounding of the weld seam compared to the surrounding bulk material due to, e.g. burn-off losses, which can cause a galvanic coupling.[3,4] One of the most straightforward measures to prevent corrosion, is to immediately coat the weld seam. For this purpose the Institut für Werkstoffkunde (IW) and the Institut für Anorganische Chemie (ACI) of the Leibniz Universität Hannover have cooperated to develop a novel hybrid tool which combines the joining step and the application of an anti-corrosive coating of magnesium parts in a single processing step. This hybrid tool, which was designed and constructed by the IW, consists of a tungsten inert gas (TIG) torch for joining and an attached suspension plasma sprayer (SPS) for subsequent coating of the weld seam. The SPS allows the processing of feedstock suspensions with sub-micrometer particles and consequently produces fine-grained coatings with superior properties.[5]

---

1) Feynman RP, *Caltech Eng. Sci.* **1960**, *23*, 22-36.
2) Song G, *Adv. Eng. Mater.* **2005**, *7*, 563-585.
3) Zeng R-C, Chen J, Dietzel W, Zettler R, dos Santos JF, Nascimento ML, Kainer KU, *Corros. Sci.* **2009**, *51*, 1738-1746.
4) Xu RZ, Song G, Wang Z, *Mater. Res. Innov.* **2009**, *13*, 441-447.
5) Klillinger A, Gadow R, Mauer G, Guignard A, Vaßen R, Stöver D, *J. Therm. Spray Technol.* **2011**, *20*, 677-695.

Sub-10 nm-MgF$_2$ nanocrystals were synthesized and formulated in an aqueous suspension and employed as a feedstock for this process. By suspension plasma spraying of those suspensions, dense MgF$_2$ films on weld seams were obtained, which showed an increased corrosion resistance.

The second part of this thesis comprises zinc oxide and its application in transparent conductive films. Materials which are optical transparent and simultaneously provide good electrical conductivity are irreplaceably required for various optoelectronic devices such as photovoltaic cells, flat panel displays, and touch screens.[6] Besides extremely thin metal films, only the group of transparent conductive oxides (TCOs) fulfills these requirements. Well-established TCO materials such as indium tin oxide (ITO) display high price volatilities and the conventional physical vapor deposition methods for TCOs are expensive, have a limitation of scaling-up, and are carried out at high temperatures which limits the assortment of substrates.[7] Zinc oxide is a promising alternative as it can be deposited by low-cost and low-temperature chemical bath deposition (CBD) on large area substrates. Furthermore, the solution chemistry used in CBD permits the usage of additives which in turn can be used to alter film morphologies and hence film properties such as transparency and conductivity.

The synthesis of thin ZnO films by controlling the morphology via additive-assisted CBD was addressed in two work packages. In the first work package, the influence of organic additives on the growth of ZnO was investigated in precipitation experiments. The findings of these investigations were applied to CBD of ZnO films. For the precipitation experiments, two natural polysaccharides, hyaluronic acid (HYA) and chondroitin-6-sulfate (C6S) were employed. Depending on the polysaccharide, different ZnO mesocrystal morphologies were obtained. The origin of the different morphologies could be traced back to different interactions of the polysaccharides with ZnO during precipitation. In the second work package, HYA was employed in the CBD of ZnO on glass substrates. Here, the addition of HYA suppressed the *c* axis growth of ZnO and led to strongly intergrown ZnO films which display enhanced conductivities.

6) Gordon RG, *MRS Bull.* **2000**, *25*, 52-57.
7) Huang SM, Bian ZQ, Chu JB, Wang ZA, Zhang DW, Li XD, Zhu HB, Sun Z, *J. Phys. D: Appl. Phys.* **2009**, *42*, 055412.

2 General Principles

This chapter on General Principles provides the background for the scientific publications in chapter three to five. While the subsection 2.1 comprises the topic of corrosion protection of magnesium welds by the use of aqueous suspensions of magnesium fluoride, subsection 2.2 deals with transparent conductive films and the usage of morphology-tailored ZnO for these applications.

2.1 Corrosion-Protecting Coatings on Magnesium

The following subsections deal with different state-of-the-art and emerging applications of the light-weight metal magnesium and discuss magnesium's biggest drawback – its corrosion sensitivity. Furthermore, the importance of appropriate surface coatings is emphasized. Besides common corrosion protection coatings, which are addressed in this context, a new approach of magnesium surface coating by hybrid TIG/SPS process is introduced.

2.1.1 Applications of Magnesium and Magnesium Alloys

Besides some niche applications in aircrafts, sport and electronic goods, space explorations, and nuclear reactors (canning material with low neutrons absorption),[8] magnesium and magnesium alloys (further generally referred to as magnesium) are highly interesting for medical and automotive applications. The latter is the major driving force for alloy and processing development accounting for the consumption of approximately 90% of all magnesium.[9,10] In the course of this subsection the history of magnesium in both domains is given in order to explain significance of magnesium nowadays. Furthermore, the properties of magnesium which makes it such an attractive material for these applications are pointed out and are discussed.

At the beginning of the 20th century, magnesium was used as structural material in automotive applications for the first time. The first companies which utilized magnesium as parts of cars and trucks were Büssing in 1924 and Adlerwerk in 1927. Adlerwerk assembled magnesium casts and pressed parts with up to 86.8 kg per car.[10]

8) Eliezer D, Aghion E, Froes FH, *Adv. Perform. Mater.* **1998**, *5*, 201-212.
9) Mordike BL, Ebert T, *Mater. Sci. Eng. A* **2001**, *302*, 37-45.
10) Kulekci MK, *Int. J. Adv. Manuf. Technol.* **2008**, *39*, 851-865.

After the Second World War the use of magnesium in automotive application increased drastically, reaching its maximum when the mass production of the VW beetle started. However, with the production stop of the air cooled Mg power train of the VW beetle due to an increasing magnesium price in the 1970s, magnesiums long history in automotive applications almost came to an end and plenty of know-how was lost during the following years.[9-11] In the early 1990s, automotive manufactures were forced to decrease the energy consumption and the CO_2 emission of their carfleets due to stricter legislative regulations.[10] Since a vehicle weight reduction of 100 kg reduces the fuel consumption about 0.5 liters per 100 km,[10] weight saving is a very attractive strategy to meet those regulations. For this purpose, magnesium is the metal of choice due to its superior strength-to-density ratio compared to all other structural metals. However, it has to compete against other light-weight materials such as aluminum alloys and plastics.[11]

Nevertheless, automobile prices also have to be competitive and are thus a major criterion for the choice of material.[10,12] In this context magnesium has had the disadvantage of being comparatively expensive for a long period of time. But when the increasing production of magnesium in China led to a strong price competition with the three remaining magnesium primary producers in the western world (US Magnesium, Dead Sea Magnesium and Rima), the magnesium price steadily decreased.[13] Finally in 2005, the price per kg magnesium was less than that of aluminum.[10] Although the density of magnesium is 2/3 of aluminum, more material has to be used to assure the same stiffness of the workpiece, due to the comparably low Young's modulus of magnesium (elastic modulus in 10^6 Mpa: Mg $\approx$ 44 / Al $\approx$ 69 / Fe $\approx$ 207).[10,12] Taking the Young's modulus into account, usage of magnesium still saves 10-41% of weight compared to aluminum and 62% compared to steel and is thus very attractive in applications for which weight saving is of concern.[12] In addition to the price issue, the corrosion characteristics of magnesium are a major disadvantage and were sometimes referred to as "awful".[8] Heavy metal impurities such as nickel, iron, and copper in the magnesium alloys initiate galvanic coupling with the magnesium matrix.[8] Minimizing such impurities below a critical concentration led to high purity magnesium alloys (e.g. AZ91) which have been responsible for a major breakthrough in terms of corrosion characteristics.[8]

11) Blawert C, Hort N, Kainer KU, *Trans. Indian Inst. Met.* **2004**, *57*, 397-408.
12) Das S, *JOM-J. Min. Met. Mat. S.* **2003**, 22-26.
13) Beals RS, Tissington C, Zhang X, Kainer K, Petrillo J, Verbrugge M, Pekguleryuz, *JOM-J. Min. Met. Mat. S.* **2007**, 39-42.

Even though the price for magnesium is still high and galvanic corrosion is still of concern, magnesium consumption has steadily increased since the 1990s and is expected to increase further by at least 300% within the next 8-10 years.[8]

The use of magnesium in medical implants dates back even further than the application in the automotive industry. In 1878, the physician Edward C. Huse utilized magnesium wire ligatures to stop the bleeding of humans vessels and enthusiastically reported about their degradation behavior.[14] Since then, physicians have tried to extend the clinical use of magnesium e.g. as a temporary support for bone fractures. One of the most serious drawbacks, however, was again the corrosion of magnesium, this time *in vivo*, resulting in fast degradation and the formation of subcutaneous gas cavities of hydrogen.[14]Nevertheless, researchers have recognized the enormous potential of magnesium since there is a medical need for temporary implants. Implants can be divided into two groups: permanent and temporary implants. While permanent implants replace a diseased part permanently, temporary implants support the healing process as long as necessary. By using a temporary implant, a secondary surgery for removal can be avoided, thus minimizing the probability of complications. Additionally, patients benefit from magnesium implants due to their stimulating effects on bone growth and their non-toxic metabolism products (the average human body already contains approx. 35 g of magnesium as ions which take part in more than 300 enzymatic reactions).[16,17]

Although magnesium implants have been investigated for more than 130 years, only now first commercial magnesium implants appear on the market. So far, absorbable polymers such as poly-lactic acid are commonly used as biodegradable materials; these, however, are limited by their poor mechanical properties.[17] This has caused reconsideration of magnesium as an implant material, driven by the prospect of alloys with reduced impurities and novel surface coating techniques, both allowing to control the degradation behavior.[17]

14) Witte F, *Acta Biomaterialia* **2010**, *6*, 1680-1692.
15) Krause A, von der Höh N, Bormann D, Krause C, Bach FW, Windhage H, Meyer-Lindenberg A, *J. Mater. Sci.* **2010,** *45*, 624-632.
16) Song G, Song S, *Adv. Eng. Mater.* **2007**, *9*, 298-302.
17) Brar HS, Platt OP, Sarntinoranont M, Martin PI, Manuel MV, *JOM-J. Min. Met. Mat. S.* **2009**, *61*, 31-34.

2.1.2 Corrosion Behavior of Magnesium and Magnesium Alloys

While magnesium has a huge potential in diverse industrial as well as medical applications, its corrosion characteristics are a major problem which still restrict a widespread usage. Here, the corrosion behavior of magnesium is encompassed with regard to different forms of corrosion and in different media as well as in respect to its corrosion performance. Magnesium is placed at the bottom of the galvanic series with a standard potential of -2.37 V$_{NHE}$ (Mg(II)/Mg) and thus galvanic corrosion frequently occurs. Magnesium is a very reactive metal, used for example as a reduction agent in pyrometallurgical processes to produce metals like titanium, uranium and zirconium.[18] However, in diluted chloride solution magnesium displays a corrosion potential of approx. -1.7 V$_{NHE}$. The difference to the thermodynamic standard potential implies that magnesium has no direct contact to the reduction media – in this case the chloride solution. Indeed, a more or less crystalline magnesium hydroxide film immediately forms on the surface of magnesium upon contact with the aqueous environment, and serves as an anti-corrosive layer.[18]

As indicated by the difference of the thermodynamic potential of magnesium in diluted chloride solution compared to the standard potential, corrosion of materials strongly depends on the environment, e.g. solutes in aqueous media, atmospheric surrounding, or, for biomaterials, the human body. Therefore, corrosion performances must always be evaluated with regard to their specific application environments, since important factors such as formation of a protective film, the type of corrosive attack and presence of attacking species, e.g. oxygen, water or different ions play crucial roles.[18]

There are three major aspects of the magnesium corrosion mechanisms to be considered: General corrosion driven by the placement of magnesium in the electrochemical series, the phenomenon of the negative difference effect (NDE), and microgalvanic corrosion of magnesium alloys, occuring between the magnesium matrix and a secondary phase or impurities.

18) Song GL, Atrens A, *Adv. Eng. Mater.* **1999**, *1*, 11-33.

General Galvanic Corrosion

Galvanic corrosion, in general, requires at least the existence of a thin aqueous film. This is the reason why magnesium barely shows any corrosion in indoor environments or if it is processed thoroughly so that contact with water can be excluded. Examples for the latter are steering wheels or seat frames in cars. By contact with air a grayish film of magnesium hydroxide forms on the surface of magnesium which provides a protective layer against further corrosion, thus leading to superficial corrosion only.[19] Atmospheric corrosion of magnesium is almost negligible and occurs with an oxidation rate of approx. 10 nm per year.[20] However, it increases markedly with humidity.[18] If the humidity is above 90%, the former uniform and amorphous magnesium hydroxide film crystallizes and local corrosion spots appear.[18] Atmospheric trace gases like CO_2 and SO_2 (especially in industrial environments) can also have an effect on the composition of the surface film formed in damp air. They converse the quasi-protective film into the corresponding carbonates, sulfites and sulfates, which have high solubilities and which can easily be washed away by rain, leaving the surface unprotected from further corrosion.[19,20] In maritime environments, the breakdown of the quasi-protective film can be caused by salt water splats, containing chloride ions.

Corrosion of magnesium in aqueous solution depends on a variety of factors but is always directly related to prevention/breakdown of the formation of a protective film. The Pourbaix diagram (pH versus potential) for magnesium (Figure 1) depicts thermodynamic data based on the NERNST equation and marks a pH range (larger than > 11) in which the formation of a quasi-passivating magnesium hydroxide film is thermodynamically favored.[18,19] However, this approach does not include the presence of MgH_2 and the formation of monovalent Mg(I), which will be discussed later. The corrosion characteristic of magnesium in aqueous environment is strongly governed by the formation of a hydroxide film.[18]

19) Ghali E, Dietzel W, Kainer K-U, *J. Mater. Eng. Perform.* **2004**, *13*, 7-23.
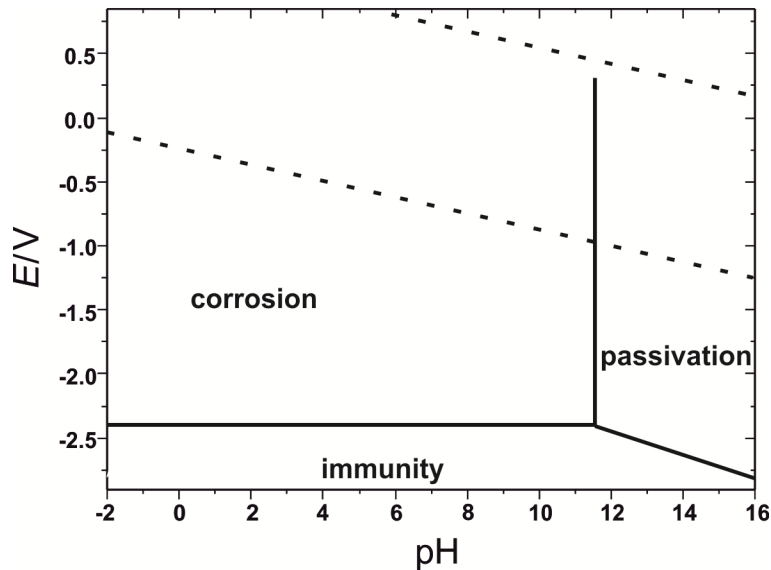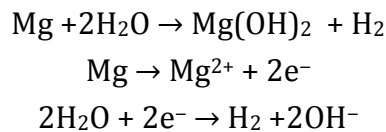20) Ferrando WA, *J. Mater. Eng.* **1989**, *11*, 299-313.

Fig. 1 Schematic Pourbaix diagram for the Mg–H$_2$O system at 25°C (adopted from [18]).

Upon contact with water, magnesium is oxidized to Mg(II), a redox process which is accompanied by the formation of hydrogen gas:

$$Mg + 2H_2O \rightarrow Mg(OH)_2 + H_2$$
$$Mg \rightarrow Mg^{2+} + 2e^-$$
$$2H_2O + 2e^- \rightarrow H_2 + 2OH^-$$

There is evidence that oxidation of magnesium proceeds via a univalent Mg(I) intermediate, which has a very short lifetime and immediately reacts with water to form Mg(II) and gaseous hydrogen. This may cause the negative difference effect (NDE), which will be discussed in detail later on.[18,19]

It is proposed, that upon contact with water a MgO film is formed which is then rapidly converted to a Mg(OH)$_2$ film. This Mg(OH)$_2$ film may be composed of crystalline brucite, however, the composition is slightly variable.[19] As already indicated in Figure 1, such a brucite layer is stable in alkaline media as a result of its low solubility at these conditions. Even if magnesium is exposed to neutral or more acidic solutions, such a film may serve as a corrosion barrier, since the local pH increases upon magnesium corrosion due to the formation of hydroxyl ions (see reaction equations above), i.e. the corrosion is to a certain extend self-limiting.[21]

21) Song G, Atrens A, *Adv. Eng. Mater.* **2003**, *5*, 837-858.

However, when the $Mg(OH)_2$ film breaks down, corrosion can extend beyond the local barrier. This breakdown can be caused by a strong movement of solution, compensating the local pH equilibrium and thus facilitating further corrosion. In practice however, breakdown of the $Mg(OH)_2$ film is mainly caused by anions in solution. Thus the solubility of the corresponding magnesium salt correlates with the extent of film destruction.[19] Whereas fluoride ions lead to the formation of an almost insoluble and passivating magnesium fluoride film, anions such as bromide, chloride, sulfate and perchlorate are soluble and consequently lead to film destruction and increased corrosion.[19]

Negative Difference Effect

Experiments have revealed that there is a systematic error between potentially measured corrosion rates of magnesium and hydrogen evolution, as well as the weight loss of magnesium. This was also observed for aluminum but not for other structural metals.[22] For both, aluminum and magnesium, more hydrogen gas is produced during corrosion than expected based on Faraday's Law. This phenomenon is called the "negative difference effect" (NDE). The difference between the expected and observed corrosion rates can be up to 30%.[23]

Although it appears that the NDE is an analytical problem, it has been found that the extent of the NDE correlates with corrosion rates: the higher the corrosion rates, the more pronounced the NDE.[18] Thus, the existence of the NDE indicates that there is a lack of knowledge concerning the basics of the corrosion mechanism.

The mechanism of the NDE is discussed controversially. There are at least six models which try to explain the NDE:[18,23,24]

- protective film breakdown
- monovalent magnesium
- magnesium hydride
- particle undermining
- magnesium self corrosion
- double cathodic process

Frequently, the intermediate formation of monovalent magnesium Mg(I) is referred to as an explanation for the NDE, often in combination with a breakdown of the protective film.[18,22,23] However, monovalent magnesium is otherwise not known in chemistry, rendering its (intermediate) formation highly unlikely from a chemist's point-of-view.

22) Liu LJ, Schlesinger M, *Corros. Sci.* **2009**, *51*, 1733-1737.
23) Atrens A, Dietzel W, *Adv. Eng. Mater.* **2007**, *9*, 292-297.
24) Bender S, Goellner J, Heyn A, Schmigalla S, *Mater. Corros.* **2011**, *62*, 1-6.

Recently, Bender and co-workers introduced a new model which denies the formation of monovalent magnesium and postulates the existence of two separated, electron-consuming processes. One results from the external polarization of the magnesium specimen during electrochemical measurement; this is the current which is measured. The other one can be traced back to the formation of magnesium hydroxide, causing an enrichment of hydrogen ions at the surface. These hydrogen ions discharge and form hydrogen gas; the corresponding current is not included in Faraday's Law.[24]

Microgalvanic Corrosion

Macrogalvanic corrosion occurs when magnesium is connected with another metal. Since magnesium is the most reactive structural metal used, magnesium is always the anode within such couples and consequently corrodes.[21] By elaborate engineering and manufacturing in order to avoid contact of magnesium with other metals, macrogalvanic corrosion can be excluded.

Microgalvanic corrosion, however, is a major issue in magnesium corrosion, especially for alloyed magnesium. The elemental composition of magnesium is crucial for corrosion, since alloying or impurity elements can form a galvanic couple with the magnesium matrix, whereupon the magnesium corrosion is enhanced (illustrated in Figure 2a). Thus the corrosion rate is influenced by the relative position of these elements in the electrochemical series, their concentration in the alloy, and their hydrogen overpotential.[18] Some elements can also have a beneficial effect, actually counteracting the corrosion process. For example, aluminum containing magnesium alloys show an enrichment of aluminum in the oxide surface film. Increasing the aluminum content in the alloy leads to thicker and aluminum enriched oxide films, accompanied by better corrosion performance.[19] Elements which markedly accelerate the corrosion rate (usually in the range of 10- to 100-fold) even in very small amounts are called "impurity elements". The concentration at which such impurity elements increase the corrosion rate significantly is called "tolerance limit" (as illustrated in Figure 2b). Impurity elements such as iron, copper, nickel, and cobalt have a very low tolerance limit of less than 0.2%, whereas silver, calcium, and zinc have a limit of approx. 0.5 to 5%.

In addition, the presence of further elements influence the tolerance limit of these impurity elements, e.g. aluminum decreases the tolerance limit of iron, probably by formation of a more reactive $FeAl_3$ intermetallic phase.[18] The origin of the tolerance limits is not fully understood, however, elements with low limits also show a low solubility in the solid magnesium phase. Thus, they probably segregate and act as cathodes.[18]
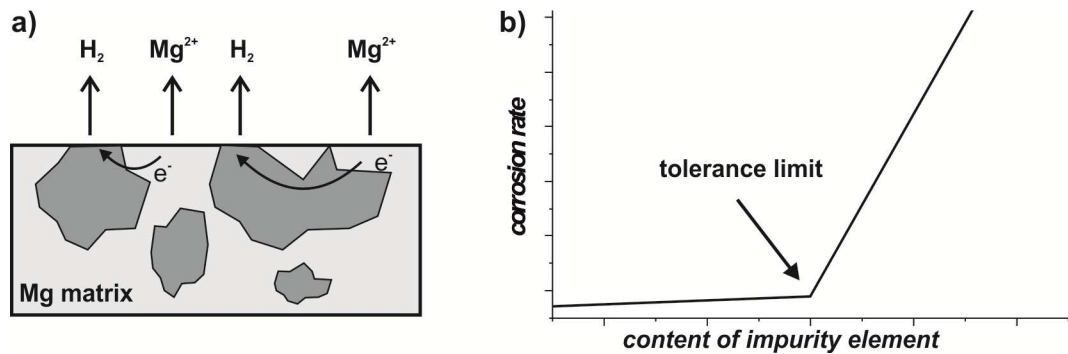

Fig. 2 a) Illustration of microgalvanic corrosion in magnesium alloys; b) schematic plot of the corrosion rate of magnesium in dependence of the impurity content (adopted from [18]).

The purity of magnesium and magnesium alloys is crucial for their corrosion resistance. In particular, former magnesium alloys suffered from microgalvanic attack due to large amounts of impurity elements. For example, contaminations with iron were introduced by the usage of steel melting pots.[18] Awareness of the tolerance limits has led to the development of high purity (HP) alloys, with improved corrosion resistances.[18]

The presence of other elements in the alloy often leads to the formation of secondary phases, which additionally influence corrosion characteristics. For example, aluminum impurities can form a secondary phase with the composition $Mg_{17}Al_{12}$. In principle, this phase has two opposing effects on the corrosion behavior. On the one hand, it can initiate galvanic coupling within the magnesium matrix, usually rendering the magnesium matrix anodic to the secondary phase and consequently leading to corrosion of magnesium. On the other hand, the $Mg_{17}Al_{12}$ phase shows a better passivity over a wider pH range than magnesium and aluminum individually. Thus, depending on the $Mg_{17}Al_{12}$ volume fraction and its distribution, this secondary phase could in principle enclose the magnesium matrix acting as a barrier to corrosion.[18,19]

Especially prone to corrosion are weld seams. This is in part caused by the disturbance of the material structure in the heat-affected zone of the weld seam, but is also due to the fact that the filler wire used in welding usually has a different elemental composition as the surrounding bulk material and that in addition compositional changes occur due to burn-off losses. Both circumstances can cause a galvanic coupling.[2,3]

Approaches for Corrosion Prevention
One of the most effective ways to minimize corrosion is to seal the material surface against the environment by coating. Coatings do not only improve corrosion resistance but also wear resistance, and can at the same time serve as a decorative finish of the workpiece. For decent corrosion protection, the coating must be uniform, pore-free and firmly adherent to the substrate. Furthermore, the coating must be self-healing for applications in which damage to the coating may occur.[25]

There are well-established coating techniques for magnesium and magnesium alloys available, each of which has its own advantages and disadvantages. Coating techniques can be distinguished by their application method. In the following paragraph, the most prominent coating techniques are described.

Electrochemical plating is a simple and cost-effective coating method in which a metallic layer is produced on the surface of the substrate by reduction of the corresponding metal ions in solution. For magnesium, usually Cu-Ni-Cr plating is used to provide sufficient corrosion and wear protection for in-door and mild exterior applications.[25]

Conversion coating is also a reasonably priced solution-based technique, in which the surface of the metallic substrate is converted into the corresponding metal oxides, phosphates or chromates. Chromium-based conversion coatings are well-established, but will be abandoned due to a high toxicity of the bath solution. Phosphate-permanganate and fluorozirconate conversion coatings are more environmentally friendly while the corrosion protection is comparable. Thus, these are promising alternatives to chromium conversion coatings. In general, the corrosion and wear resistances of conversion coatings are not sufficient for harsh conditions, but they provide a good support for additional coatings.[25]

---

25) Gray JE, Luan B, *J. Alloy Compd.* **2002**, *336*, 88-113.

The most common coating technique for magnesium and its alloys is anodizing, which provides superior corrosion protection and which encompasses proprietary processes like Magoxid and Anomag. Anodizing produces a stable ceramic layer on the surface of the substrate via plasma discharge in an electrolytic solution and subsequent short-term surface melting of the substrate. At present, none of the single coating techniques provides sufficient corrosion protection in harsh media. Thus, in most cases, several coating techniques are combined.[25]

A niche coating technique is the group of thermal spray processes, which includes plasma spraying. Although plasma spraying is a well-established process in the manufacturing industry, it is almost exclusively used for high-added value coatings, such as carbide coatings for compressor blades for air craft turbines.[26,27] Recently, studies have shown the enormous potential of plasma spraying on magnesium alloy substrates with regard to a significant improvement of wear and corrosion properties.[28,29] The basics of thermal spraying with a focus on plasma spraying are discussed in the following subsection.

26) Fauchais P, *J. Phys. D: Appl. Pys.* **2004**, *37*, 86-108.
27) Davis JR (Ed.), *Handbook of Thermal Spray Technolog*, ASM International **2004**, 3-13.
28) Tsujikawa M, Adachi S-i, Abe Y, Oki S, Nakata K, Kamita M, *Plasma Process. Polym.* **2007**, *4*, 593-596.
29) Zeng R, Dietzel W, Chen J, Huang W, Wang J, *Key Eng. Mater.* **2008**, *373-374*, 609-612.

2.1.3 Suspension Plasma Spraying

Suspension plasma spraying (SPS) has emerged from plasma spraying, which in turn, is a sub-class of thermal spray procedures.

General Aspects

Thermal spraying encompasses a group of coating processes in which material is sprayed in a molten or semi-molten state onto a substrate to form a coating. Depending on the heat source, thermal spray can be divided in three major categories: Flame spray, electric arc spray and plasma spray (Figure 3).[30] Generally, the heat source is utilized to transfer the coating material, which can be supplied as powder, wire or in liquid/dispersed form, into a molten or semi-molten state.
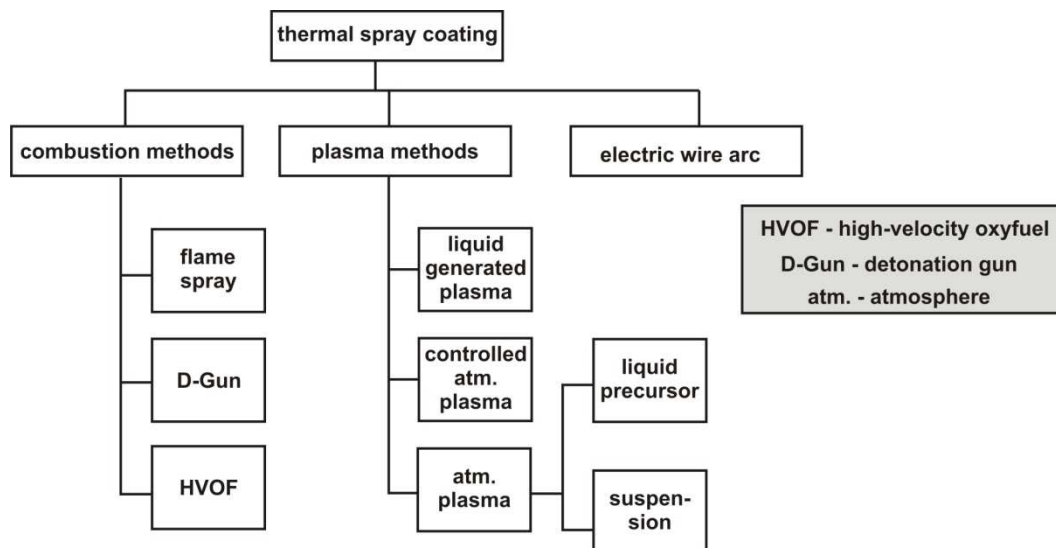
Fig. 3 Hierarchy of thermal spray methods (adapted from [30]).

These coating materials are rapidly accelerated towards the substrate due to the thermal expansion of the gas. Upon impact on the substrate, the material is solidified and consequently forms a coating.[30] The most important feature of thermal spray technologies is the opportunity to spray virtually any material that melts congruently, i.e. which does not decompose upon melting. However, for practical applications the melting point should be at least 300 °C below the vaporization or decomposition temperature in order to ensure efficient coating.[26] In addition, the heat input on the substrate is relatively low, thus a wide variety of substrates can be coated by these methods. Besides its application for coating processes, thermal spraying is also utilized for restoring and repairing worn components.[30]

---

30) Davis JR (Ed.), *Handbook of Thermal Spray Technology*, ASM International **2004**, 3-13.

The main disadvantage of all thermal spray processes is the line-of-sight nature, meaning that only parts which are accessible by the particle stream are coated. This limits efficient coating to components with rather simple geometries.[30] However, the outstanding flexibility of thermal spraying has led to its widespread application in the manufacturing industry nowadays.

Historical Background

The first record of thermal spraying dates back to the 1880s when Schoop introduced a coating technique which was based upon a modified oxyacetylene welding torch coupled with a wire-feed.[30] A chronological diagram of important developments in thermal spray is given in Figure 4. Due to the relative low temperature of the flame, this process was limited to metal feeds with melting points below 1600 °C such as tin and lead.[31] In 1908, the assortment of spray-able metals could be expanded with the introduction of electric arcs as a more powerful source of thermal energy. In 1939, the scope of applicable coating materials became virtually unlimited with the introduction of plasma spraying torches by Reinecke. Due to significantly higher temperatures of the plasma, even high-temperature ceramics became applicable for melted and processing.[30] The first industrial applications for plasma spraying emerged in the late 1950s and 60s for coatings of aerospace and aircraft engines.[31] In the following years, plasma spraying processes were increasingly used and have achieved great acceptance in the manufacturing industry. Further improvements of the process were realized in the 1980s and 90s by new torch designs as well as robot-assisted spraying. In 1983, high-velocity oxyfuel (HVOF) spraying was introduced by Browning.[26] This process allows very high gas velocities with up to 2000 m/s by deflagration of compressed hydrocarbons.[32] By 2004, HOVF spraying accounted for one fourth of the total spraying market and it was mainly used for WC-Co cermet coatings.[32] Reliability and reproducibility of plasma spraying were drastically increased in the 1990s by the implementation of on-line control using robust sensors for monitoring particle temperatures and velocities, as well as heat flux distributions.[26] Recent efforts are devoted to gain a better understanding of the mechanisms occurring during plasma spraying and to develop processes capable of the application of nanostructured coatings.

31) Fauchais P, Vardelle A, Dussoubs B, *J. Therm. Spray Technol.* **2001**, *10*, 44-66.
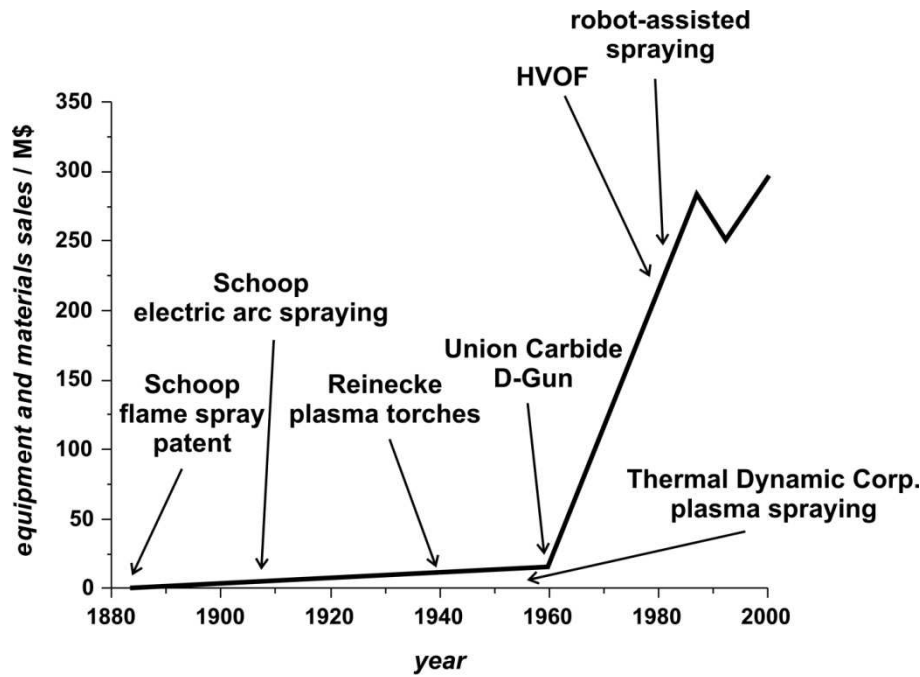32) Fauchais P, Montavon G, *Key Eng. Mater.* **2008**, *384*, 1-59.

Fig. 4 Chronological developments of thermal spraying and sales related to thermal spraying (adopted from [30,31]).

Plasma Spraying

As mentioned above, a wide variety of thermal spray methods are available. Figure 5 compares the most important methods with regard to process temperature and velocity. Plasma spraying is one of the most versatile thermal spray techniques as it covers a huge range of process temperatures and particle stream velocities. It has a market share of about 50% and is thus the most prominent and important thermal spray technique.[32]
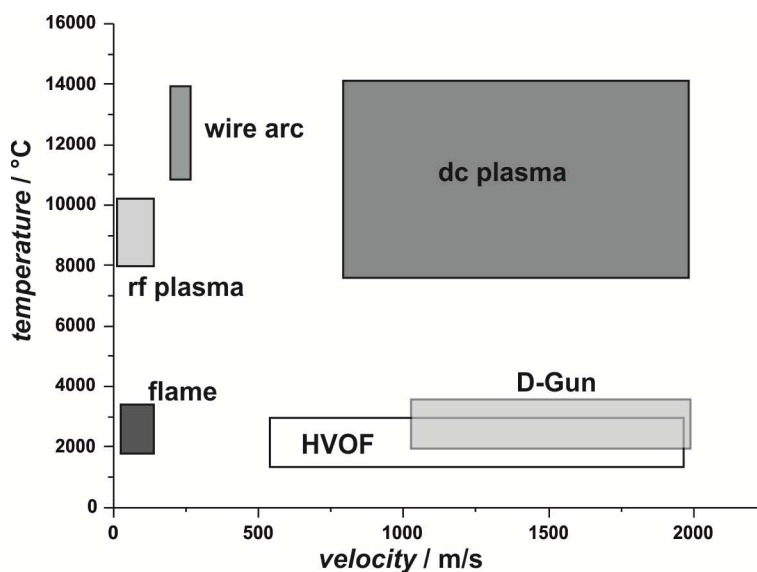

Fig. 5 Operating conditions of thermal spray methods with regard to their heat source temperature and particle velocity (adopted from [32]).

An electrical arc, initiated with typical power levels from 20 to 200 kW, is used in plasma torches to create plasmas with argon and mixtures of argon with noble or molecule gases such as nitrogen, hydrogen and oxygen.[33] The plasma temperatures, which depend on the plasma gases used, can reach up to 15.000 °C, significantly surpassing the melting point of any material.[30] Into the plasma jet, well flowable powder feedstocks are injected via a carrier gas, accelerated, and finally hit the target in a molten or mushy state to form the coating. According to torch design, plasma spraying can be divided into direct current (dc) and radio frequency (rf) plasma spraying (Figure 6). Over 99% of the industrial plasma spray equipment operates with dc plasmas, which are also referred to as atmospheric (APS) or conventional (CPS) plasma spraying.[26] The most prominent difference between both torch designs is the internal diameter of the torch. Dc plasma spraying operates at much smaller torch diameter, which results in significantly higher plasma jet velocities, since the velocity is roughly inversely proportional to the square of the torch diameter.[26] Typical velocities range from 600 to 2.300 m/s for dc and are below 100 m/s for rf plasma torches.[26]
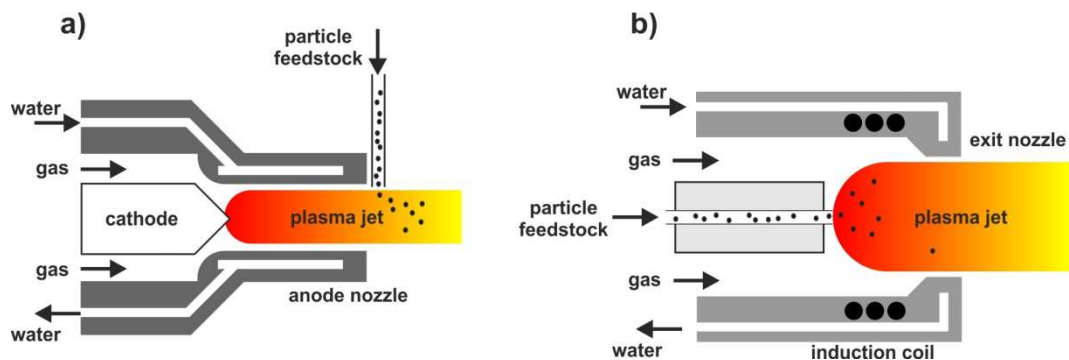
Fig. 6 Schematic diagram of a dc plasma torch (a) and an rf plasma torch (b) (adopted from [26,33]).

Furthermore, rf torches are exclusively used in controlled atmosphere. The comparably low velocity of rf plasmas leads to high residence times (up to tens of milliseconds) of the particles in the plasma and thus to a high heat input.[26] For these reasons, rf plasma spraying is used for processing of large particles (up to 200 μm) and/or for materials which are sensitive to oxygen.[34] Generally, in dc plasma spraying much smaller particle feedstocks with sizes between 10 and 100 μm are used.[35] Due to the high velocity, those particles have short residence times in the plasma jet between 0.1 and a few milliseconds.[26]

33) Chawla V, Sidhu BS, Puri D, Prakash S, *Mater. Forum* **2008**, *32*, 137-143.
34) Fauchais P, Montavon G, Vardelle M, Cedelle J, *Surf. Coat. Technol.* **2006**, *201*, 1908-1921.
35) Vaßen R, Kaßner H, Mauer G, Stöver D, *J. Therm. Spray Technol.* **2010**, *19*, 219-225.

In contrast to rf plasmas, where the particles can be injected via a water-cooled injection probe along the torch axis, the feedstock in dc plasmas is usually radially injected outside of the plasma plume to avoid clogging due to the higher energy density of dc plasmas.[26,36] Coatings are formed by successive impacts of particles, which ideally are in a mushy or molten state. Upon impact on the target, the particles form splats which rapidly solidify before the next impact of particles occurs.[26] Therefore, the coating is formed by layering splats as illustrated in Figure 7a.[26] These splats adhere to the substrate and to previous splats mainly via mechanical forces.[37] Typical plasma spray coatings have thicknesses of 100 μm to 1 mm and can display porosities of up to 20%.[36] Coating properties strongly depend on the substrate preparation, the plasma jet, the particle parameters upon impact (size, temperature, velocity and number flux), and the splat layering.[26]

Usually feedstocks provide a certain non-negligible particle size distribution, which is a matter of prize. Particles prefer different trajectories within the plasma jet depending on their inertia. This can result in a mixture of molten and not fully molten particles hitting the target, thus leading to a situation illustrated in Figure 7b in which unmolten particles are embedded into the coating forming voids.[30]

However, inhomogeneously molten particles which result in porous coatings can be beneficial for some applications, such as the preparation of thermal barrier coatings (TBCs).[26]
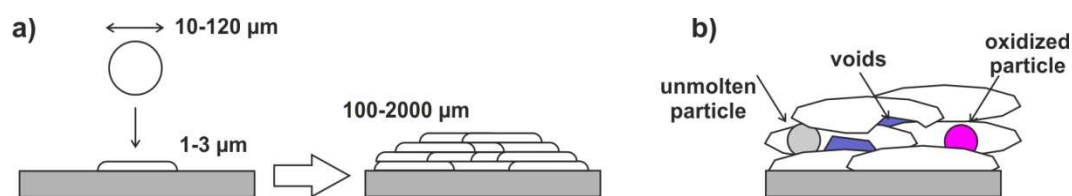

Fig. 7 a) Principle of plasma spraying coating formation; b) scheme of coating structure (b) (inspired by [26,32]).

36) Fauchais P, Rat V, Delbos C, Coudert JF, Chartier T, Bianchi L, *IEEE Trans. Plasma Sci.* **2005**, *33*, 920-930.

37) Fauchais P, Etchart-Salas R, Rat V, Coudert JF, Caron N, Wittman-Ténèze K, *J. Therm. Spray* **2008**, *17*, 31-59.

TBCs for advanced gas turbines have been a major application field for plasma spraying since the 1960s. Cobalt-based Laves phases, WC-Co, SiC, TiO_2, ZrO_2, and Cr_3C_2/20-30NiCr cermets are frequently used as feedstocks in high-added value coatings to improve wear, heat, and corrosion resistances.[30,34] Although diverse coating architectures can be obtained by plasma spraying, the coating microstructure is strongly governed by the feedstock.[35] Furthermore, minimum coating thicknesses are limited to about 10 μm.[35]The demand for finer and thinner structured coatings has forced the development of several novel coating techniques since the mid 1990s.[37] Using smaller sized feedstock in conventional plasma spraying is not straightforward, since with decreasing particle size of the feedstock, the carrier gas velocity has to be increased drastically (proportional to the negative third power of the particle diameter) and a high carrier gas flow disturbs the plasma jet.[26] Critical gas flow rates are typically reached with particle sized below 10 μm.[26] Dry powders with particle sizes below 10 μm tend to agglomerate in the solid state, which hampers decent feeding. Furthermore, the trajectories of such small particles with low inertia in the plasma jet are quite unfavorable.[38] First approaches towards nanostructured coatings were based on spraying of agglomerated particles. Those particles preserve their nanostructure within the coating by carefully adjusting the spraying parameters thus only the external shell of the agglomerates is melted (Figure 8a).[37]

A relatively new approach is the injection of a liquid feedstock which can be either liquid precursors or dispersed particles. In solution precursor plasma spraying (SPPS), dissolved precursors such as nitrates or isopropoxides are injected into the plasma jet. The mechanism involved in SPPS is illustrated in Figure 8b. Precipitation starts due to the evaporation of the liquid phase. Small droplets precipitate completely, while large ones precipitate in shells, which in turn can cause fragmentation. Additionally, sintering and pyrolysis can occur before molten particles impact on the target and finally crystallize.[32] Coatings produced via SPPS however, display a more or less powder-like architecture, and hence have to be densified afterwards via tempering. Such tempering can cause grain growth and consequently the loss of the nanostructure of the coating.[26]
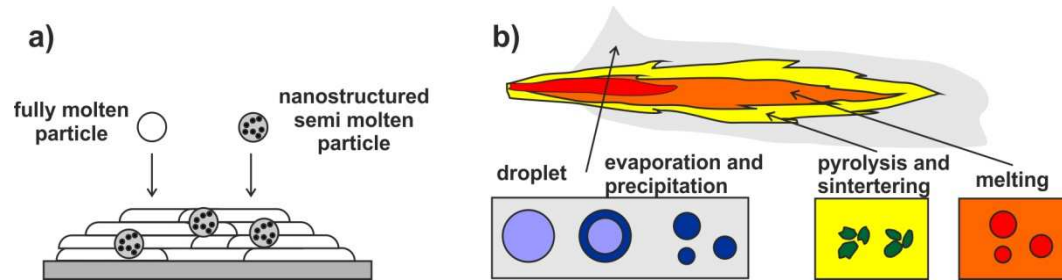
38) Pawlowski L, *Surf. Coat. Technol.* **2009**, *203*, 2807-2829.

Fig. 8 a) Scheme of the spray process of agglomerated nanoparticles; b) scheme of liquid solution precursor spraying (adopted from [32]).

Suspension Plasma Spraying

In suspension plasma spraying, the coating material is fed into the plasma jet via aqueous or alcoholic suspensions of sub-micrometer particles. This allows the processing of particle sizes below 10 μm. Two possible injection methods are commonly used, either gas atomization resulting in a broad droplet size distribution between 10 and 100 μm and velocities up to 100 m/s, or mechanical injection.[26,34] In the latter, droplets sizes and velocities strongly depend on the nozzle diameter.[34] Phenomena involved at injection are extremely complex, but are crucial for SPS coating properties.[39] Once the suspension penetrates the dc plasma jet, it is accelerated and the plasma momentum disrupts the droplets into smaller ones with sizes of a few μm in a process called secondary breakup.[37,38] In rf plasmas this secondary fragmentation does not occur due to low velocities of the jets and thus vaporization of the drops is dominant.[37] As a result, the particles within the drops injected in rf plasmas are sintered and melted, resulting in sizes very similar to conventional spraying.[37] However, by the adaption of supersonic nozzles to rf plasma torches, it was recently shown to be possible to obtain nanostructured coatings.[37] In the following paragraph, only the results of SPS performed with dc plasmas are discussed. The stages involved in SPS spraying with dc plasmas are illustrated in Figure 9 and encompass droplet breakup, evaporation of the fluid, sintering and melting of the solid content, evaporation from the melted particles, and finally crystallization upon impact on the target.[38]

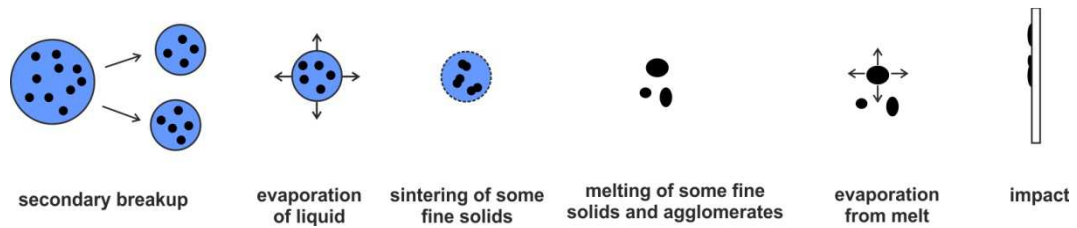39) Bartuli C, *Surf. Eng.* **2009**, *25*, 343-345.

Fig. 9 Scheme of the processes involved in suspension plasma spraying (adopted from [38]).

Fragmentation is strongly influenced by the surface tension of the droplets, i.e. the higher the surface tension of the liquid media, the longer vaporization takes place and the less energy is available for melting of the suspension particles.[37] Simultaneously to the secondary breakup, the droplet diameters decrease due to rapid evaporation of the liquid.[38] The evaporation of the liquid phase is linked to an energy consumption of about 10 to 20% of that of the plasma. However, enough energy remains for melting and acceleration of the particles.[26] After evaporation of the liquid, the particles are in direct contact with the plasma jet and sintering and melting can occur.[38] The spraying conditions have to be carefully adjusted to the suspension parameters in order to avoid complete particle evaporation.[37] For this reason, and because of the fast deceleration of the small particles, spraying distances in SPS are much shorter than in CPS (4-6 cm against 10-12 cm).[34,36] Upon impact, the particles in CPS usually form flower-like splats with long dendrites around.[38]

However, in SPS the splat morphology is rather pancake-like without dendrites, which is caused by the lower kinetic energy of the small particles upon impact.[38] These ultrafine splats show an enhanced splat-to-splat bonding.[38] In thermal spraying, cooling of the coating causes thermal stress, which may relax in form of micro-cracks. Due to different relaxation processes, SPS coatings rather show segmented cracks and a reduced amount of micro-cracks than observed in CPS coatings (compare microstructure of SPS and CPS coatings in Figure 10).[35]
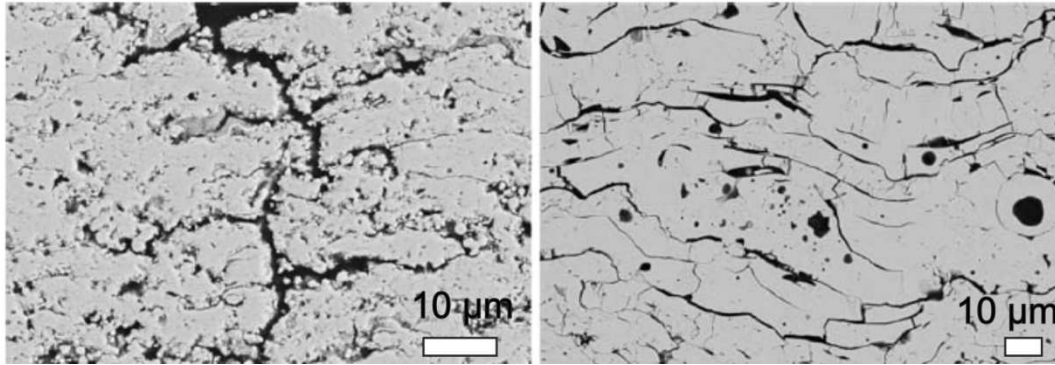
Fig. 10 SEM micrographs of suspension plasma sprayed coating displaying segmented cracks (left) and conventional plasma sprayed coating with micro-cracks (right).[35]

Such segmented coatings (as shown in Figure 10 on the left) are beneficial for TBC applications, since they provide good thermal shock resistance, a high thermal reflectivity and low thermal conductivity, and thus significantly reduce the component heating.[35] This is the reason why the application of TBC coatings by SPS is a major application field. SPS coatings were also found to be promising for Graetzel cells. By the application of fine, nanostructured TiO_2 coatings with large surface areas the quantum efficiency of the cells could be enhanced.[35,38] Solid oxide fuel cells (SOFCs) are another emerging application field for SPS. Here, higher porosities and thinner electrolytes, applied with SPS resulted in enhanced efficiency, lower operating temperatures, and thus led to an overall enhanced lifetime of the cells.[35,36,39] Despite these promising applications for SPS, it is a new technique and the scientific basis needs to be further established.[33,38]

2.1.4 Syntheses of Nanoparticles of Inorganic Fluorides

The following section gives a short overview of synthesis strategies to obtain inorganic fluorides with particle sizes on the nanoscale. Furthermore, some examples for classical as well as emerging applications of fluorides are briefly presented.

General Aspects and Applications

Inorganic fluorides have a long history in metallurgical applications as slag formers, in isotope separation (uranium purification) as well as in optical materials (scintillators, luminophores, anti-reflective coatings, etc.).[40] However, the above-mentioned examples are applications which utilized bulk fluorides. Emerging biomedical and opto-electronical technologies have led to an increased interest in nanoscopic fluorides, especially in the rare earth (RE) fluorides due to their up- and down-converting luminescence properties. In biology and biomedicine, fluorescence labeling is widely used for assays and imaging. State-of-the-art labeling systems are mainly based on organic dyes, which suffer from photobleaching, and semiconductor quantum dots (e.g. CdSe, CdSe), which can cause cytotoxicity due to release of Cd(II) ions.[41] In contrast, RE fluorides show low toxicity and a superior photostability. Furthermore, they offer additional benefits: Quantum efficiencies of nanocrystalline RE fluorides are usually higher than in most other inorganic matrixes due to low phonon energy of the host material (improbability of nonradiative relaxation). They have large Stoke's or anti-Stoke's shifts, respectively, combined with sharp emission peak profiles, which enhances the detectability.[41] Up-converting nanomaterials are expected to have a huge impact in biomedical applications like multimodal bioimaging, photodynamic therapy (PDT) and drug delivery in the future.[41] PDT is an emerging therapy for various diseases, such as cancer, and a typical concept involves an up-converting material equipped with light-sensitive molecules (called photosensitizer), and antibodies for targeting. After delivery to the target site, e.g. tumor cells, and irradiation with an appropriate wavelength, the up-converting material emits visible light which activates the photosensitizer. The activated photosensitizer produces reactive oxygen species and consequently kills the surrounding cells (illustrated in Figure 11).[41]

---

40) Fedrov PP, Luginia AA, Kuznetsov SV, Osiko VV, *J. Fluorine Chem.* **2011**, *132*, 1012-1039.
41) Li C, Lin J, *J. Mater. Chem.* **2010**, *20*, 6831-6847.

Nanocrystalline β-NaYF$_4$ fluorides co-doped with Yb/Er or Yb/Tm are known to be the most efficient up-converting materials.[41] Noteworthy, light emission of those materials can be exited with infrared light, which has a penetration depth of a few centimeters in soft tissue (about one order of magnitude deeper than visible light).[42]
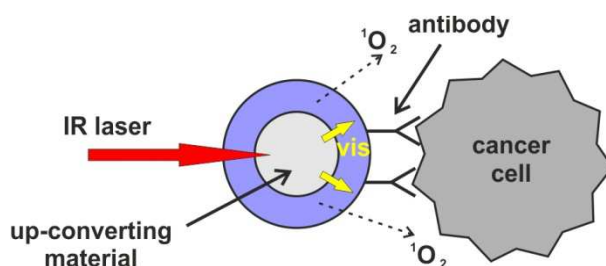

Fig. 11 Concept of up-converting nanocrystalline RE fluorides in photodynamic cancer therapy. Upon near-infrared excitation the up-converting RE fluoride nanoparticle emits visible light which causes oxygen radical formation in a photosensitizer and consequently the death of nearby cancer cells (adopted from [41]).

A further emerging application exploits the catalytic properties of nanoscopic magnesium and aluminum fluorides (MgF$_2$ and AlF$_3$). Introduced in 2003 by Kemnitz and co-workers, the so-called high-surface (HS) fluorides are characterized by their high surface area and poor crystallinity.[43] Consequently, due to uncoordinated metal ions, the HS fluorides provide extremely high Lewis acidity (e.g. HS-AlF$_3$ is one of the strongest Lewis acid).[44] Such high acidities render HS fluorides as excellent heterogenic catalysts. HS-AlF$_3$ have been successfully utilized as catalysts in diverse reactions, such as dismutations, isomerisations and dehydrofluorinations where they have shown high reactivity and selectivity.[44]

In 2009, Lellouche and co-workers presented the potential of nanocrystalline magnesium fluoride coatings to inhibit bacterial colonization on surfaces.[45] Such sterile coatings could be beneficial for application in medicine, especially considering the increasing occurrence of antibiotic resistances among bacteria.[45]

42) Chatterjee DK, Gnanasammandhan MK, Zhang Y, *small* **2010**, *6*, 2781-2795.
43) Kemnitz E, Gro U, Rüdiger S, Shekar CS, *Angew. Chem. Int. Ed.* **2003**, *42*, 4254.
44) Rüdiger S, Kemnitz E, *Dalton Trans.* **2008**, *9*, 1117-1127.
45) Lellouche J, Kahana E, Elias S, Gedanken A, Banin E, *Biomater.* **2009**, *30*, 5969-5978.

Synthesis Routes for Nanoscopic Fluorides

The synthesis of nanocrystalline fluorides can be achieved via diverse chemical and physical methods. However, in this chapter focus is put on chemical methods. Basic principles from syntheses of, e.g. oxides nanoparticles can to a certain extend be applied to fluorides, though some modifications have to be made.

Nanoparticles are accessible by solution-based approaches if either the reaction volume is restricted to the nanoscale e.g. within micelles or via surface capping surfactants, or if the number of nucleating species is very high through high initial supersaturation (initial burst). The latter often comes along with the addition of surfactants in order to avoid Ostwald ripening and/or to control the morphology by selective adsorption of the surfactant. Reference [40] provides an excellent review of synthesis strategies for nanoscopic fluorides naming numerous examples. In the following, the most important methods are categorized and discussed:

Thermolysis

Thermolysis involves the decomposition of appropriate precursor compounds at elevated temperatures in a hot-boiling solvent, often in the presence of capping ligands. Trifluoroacetates (TFAs) and fluoroammonium complexes of the corresponding metals are most frequently used as single or multi source precursors in thermolysis. In typical protocols, hot-boiling solvents such as oleic acid (OA), oleylamine (OM) and trioctylphosphine oxide (TOPO), or mixtures of these, are heated to temperatures between 250 and 370 °C under inert gas atmosphere. At such conditions, the metal-oxygen bonds are replaced by metal-fluoride bonds followed by subsequent nucleation and growth.[40] The first thermolysis of fluorides was reported by the Yan group in 2005.[46] By decomposition of a La(III) trifluoroacetate single source precursor in a mixture of octadecene and oleic acid at 280 °C, they obtained remarkable uniform LaF_3 triangular-shaped nanocrystals (Figure 12a).[46] In the same year, Zhuravleva and co-workers succeeded in the preparation of EuF_3 nanoparticles with a size distribution of approx. 3-10 nm by thermal decomposition of the corresponding trifluoroacetate in TOPO.[47] The Sun group also investigated the mechanism of thermal decomposition and was able to gain control over the phase, size, and shape of the fluorides by carefully adjusting the synthesis parameters, such as solvent composition, temperature and time (mechanism in Figure 12b).[48]

46) Zhang Y-W, Sun A, Si R, You L-P, Yan C-H, *J. Am. Chem. Soc.* **2005**, *127*, 3260-3261.
47) Zhuravleva NG, Eliseev AA, Sapoletova NA, Lukashin AV, Kynast U, Tretyakov YD, *Mater. Sci. Eng. C* **2005**, *25*, 549-552.
48) Sun X, Zhang Y-W, Du Y-P, Yan, Z-G, Si R, You L-P, Yan C-H, *Chem. Eur. J.* **2007**, *13*, 2320-2332.
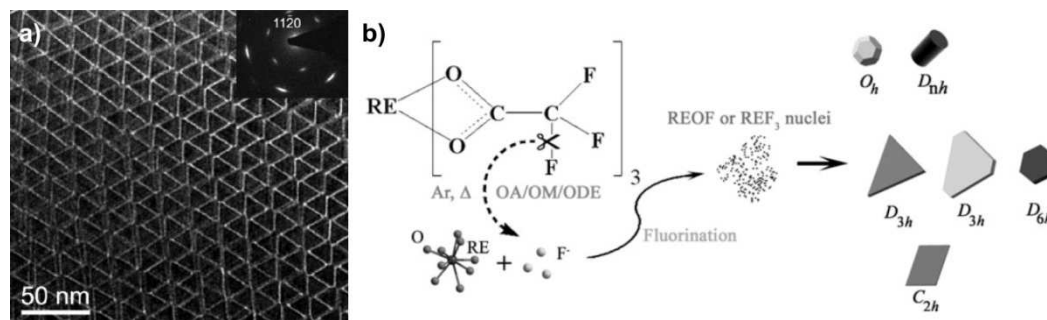
Fig. 12 a) TEM micrograph of triangular-shaped LaF_3 particles obtained via the thermal decomposition route; b) the proposed mechanism of thermal decomposition.[46,48]

Inspired by these reports, the Yan, Yi, and Capobianco groups, independently from one another, synthesized up-converting $NaYF_4$:Yb,Er,Tm nanoparticles by thermolysis.[41] In the last years, thermolysis has successfully been used for the syntheses of doped and undoped MF_2 type as well as AMF_3 and AMF_4 type fluorides, for example $\alpha NaMF_4$ (M = Dy, Ho, Er, Tm, Y, Yb, and Lu), $\beta NaMF_4$ (M = Pr, Nd, Sm, Eu, Gd, Tb, Dy, Ho, Er, Tm, Y, Yb, and Lu), MF_2 (M = Mg, Ca, and Sr), MF_2 (M = Ca, Sr, Ba), and CaF_2:Tb, $NaMF_3$ (M = Mn, Co, Ni, Mg) and $LiMAlF_6$ (M = Ca, Sr).[49-52] In general, thermolysis is a versatile synthesis route for diverse nanoscopic fluorides with narrow particle size distribution, and with excellent control over size and morphology. However, it has major disadvantages. In most cases the procedure involves the use of surfactants, which are strongly adsorbed onto the surface of the fluorides. Thus, the obtained nanocrystalline fluorides are well-dispersible in unpolar solvents, but post-synthetic steps are necessary in order to yield dispersability in polar solvents for e.g. biological applications.[41] Furthermore, the protocols are rigorous in terms of high synthesis temperatures, , inert gas atmospheres and the absence of water; also suitable precursors have to be available.[41]

49) Zhang F, Li J, Shan J, Xu L, Zhao D, *Chem. Eur. J.* **2009**, *15*, 11010-11019.
50) Du Y-P, Sun X, Zhang Y-W, Yan Z-G, Sun L-D, Yan C-H, *Cryst. Growth Des.* **2009**, *9*, 2013-2019.
51) Quan Z, Yang D, Yang P, Zhang X, Lian H, Liu X, Lin J, *Inorg. Chem.* **2008**, *47*, 9509-9517.
52) Du Y-P, Zhang Y-W, Yan Z-G, Sun L-D, Gao S, Yan C-H, *Chem. Asian J.* **2007**, *2*, 965-974.

Polyol-Mediated Synthesis

The polyol-mediated synthesis emerged from the polyol process (patented by Figlarz, Fievet, and Lagier) for the preparation of nanoscale metal particles and was initially used for the synthesis of nanocrystalline oxide particles.[53-55] It involves the use of high-boiling poly-alcohols, so-called polyols, which simultaneously act as solvent and surfactant. Among these, diethylene glycol (DEG) is the most frequently utilized polyol. In 2004, Eiden-Assmann and Maret reported the first successful synthesis of CeF_3 nanoparticles in polyol.[56] Although this synthesis route allows less control over particle size and shape, it has found wide acceptance. Nanocrystalline fluorides such as CaF_2, CaF_2:Ce,Tb, LaF_3:Yb,Er, $CeF3$:Tb/SiO_2 (core/shell) particles, CeF_3, CeF_3:Tb, YF_3, $NaYF_4$, and CeF_3:Tb/LaF_3 (core/shell) particles have been synthesized via this route.[57-61] The procedure is relatively facile, allows for large-scale synthesis, and yields particles which are well-dispersible in polar solvents, such as alcohols and water.

Sol-Gel Process

The sol-gel process is widely used for the synthesis of metal oxides. It is based on hydrolysis and condensation of metal alkoxides in ethanolic solutions containing appropriate amounts of water. In 2003, the Kemnitz group applied this basic concept to the preparation of fluorides and invented the so-called fluorolytic sol-gel synthesis.[43] In these syntheses, alkoxides react with anhydrous HF instead of water and consequently undergo fluorolysis. Similar to the classical sol-gel process, the condensation remains often incomplete and thus post-fluorination is required, e.g. with CCl_2F_2 at 350 °C.[43,44] The fluorolytic sol-gel approach usually yields X-ray amorphous metal fluorides with high surface areas (about 150-350 m^2/g).[40] Furthermore, due to the highly disordered structure, products, such as MgF_2 and AlF_3 show enhanced and tunable Lewis acidity and are successfully used in diverse heterogeneous catalysis processes.[44] Nanoscale CaF_2:Eu was synthesized in an water-containing alcoholic solution by fluoridation of the corresponding precursors with trifluoroacetic acid, and ultrasonication.[62] The sol-gel method, however, provides low control of particle size and shape, and often leads to amorphous products.[40]

53) Figlarz et al.; France-Patent 563621; **1982**
54) Merikhi J, Jungk H-O, Feldmann C, *J. Mater. Chem.* **2000**, *10*, 1311-1314.
55) Feldmann C, *Adv. Mater.* **2001**, *13*, 1301-1303.
56) Eiden-Assmann S, Maret G, *Mater. Res. Bull.* **2004**, *39*, 21-24.
57) Feldmann C, Roming M, Trampert K, *small* **2006**, *2*, 1248-1250.
58) Wei Y, Lu F, Zhang X, Chen D, *Mater. Lett.* **2007**, *61*, 1337-1340.
59) Kong DY, Wang ZL, Lin CK, Quan ZW, Li YY, Li CX, Lin J, *Nanotechnol.* **2007**, *18*, 075601.
60) Wang ZL, Quan ZW, Jia PY, Lin CK, Luo Y, Chen Y, Fang J, Zhou W, O'Connor CJ, Lin J, *Chem. Mater.* **2006**, *18*, 2030-2037.
61) Qin R, Song H, Pan G, Hu L, Yu H, Li S, Bai X, Fan L, Dai Q, Ren X, Zhao H,Wang T, *Mater. Res. Bull.* **2008**, *43*, 2130-2136.
62) Hong B-C, Kawano K, *Opt. Mater.* **2008**, *30*, 952-956.

Co-Precipitation

Co-precipitation is the most frequently used synthesis route, based on ion exchange and subsequent precipitation of the insoluble product.[40] Berzelius, who also discovered HF, was probably the first one to utilize co-precipitation for the preparation of fluorides.[63] Typical procedures for the preparation of nanoscopic fluorides by co-precipitation include mixing of preheated metal source solutions with solutions containing fluorinating agents such as NH_4F, HF, NaF, and KF. Due to the low water solubility of most alkali earth and rare earth fluorides, water is most often used as solvent.[64] However, water can strongly adsorb onto the particle surfaces and can cause pyrohydrolysis (replacement of F^- by OH^- or O^{2-}), especially in the case of nanoscopic fluorides.[64] In the following, a few examples of this widespread method are given. The Matijevic group synthesized uniform spherical MgF_2 and cubic $NaMgF_3$ particles with sizes in the µm range by carefully adjusting the molar ratios of the reactants, NaF and $MgCl_2$ (see Figure 13). In contrast to the cubic $NaMgF_3$ particles, they found the MgF_2 particles to be spherical aggregates composed of sub-micrometer particles and to contain up to 11% water.[65]
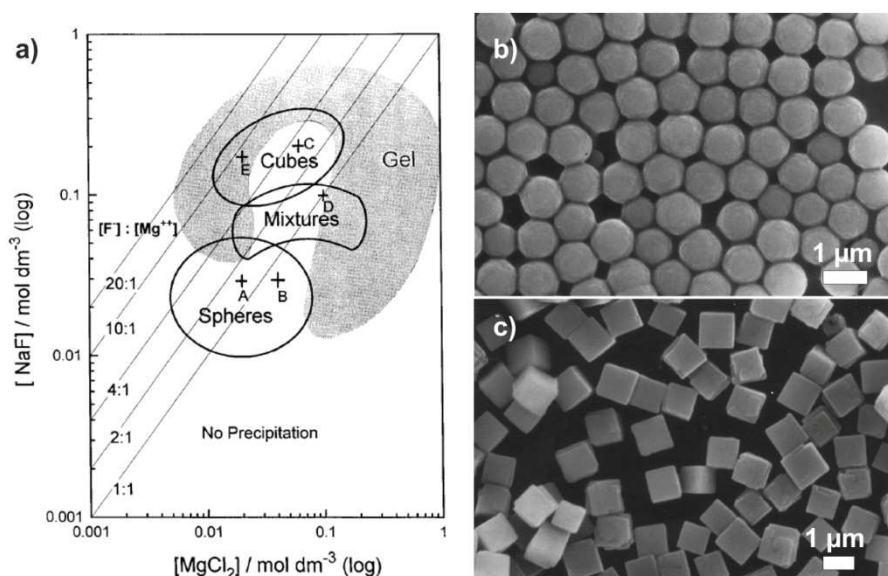

Fig. 13 a) Synthesis field diagram for reactions between NaF and $MgCl_2$. SEM micrographs of b) MgF_2 spherical aggregates and c) of $NaMgF_3$ cubes.[65]

MgF_2 spheres with diameters of 260-360 nm, were obtained by microwave-assisted co-precipitation from $Mg(NO_3)_2$ and NH_4F precursors.

63) Fedorov PP, Kuznetsov SV; Mayakova MN, Voronov VV, Ermakov RP, Baranchikov AE, Osiko VV, Russ. *J. Inorg. Chem.* **2011**, *56*, 1525-1531.
64) Kuznetsov SV, Osiko VV, Tkatchenko EA, Fedorov PP, *Russ. Chem. Rev.* **2006**, *75*, 1065-1082.
65) Hsu WP, Zhong Q, Matijevic E, *J. Colloid Interface Sci.* **1996**, *181*, 142-148.

Again, the spheres are composed of sub-micrometer particles and contain approx. 12% water.[66] Wu and co-workers prepared LaF_3, BaF_2 and NaF nanoparticles with sizes of 17, 80 and 600 nm, respectively, by co-precipitation in aqueous solution. They found a correlation between the solubility constant of the fluorides and the particle sizes, i.e. the higher the solubility, the larger the grain size.[67] MgF_2 particles with different sizes and morphologies were also synthesized by aqueous co-precipitation at 80 °C. By systematic adjusting of precursor concentrations and pH values, the formation mechanism could be switched from diffusion growth to aggregation, yielding cubic, prismatic, platelet-like particles, or spherical aggregates (see Figure 14).[68]
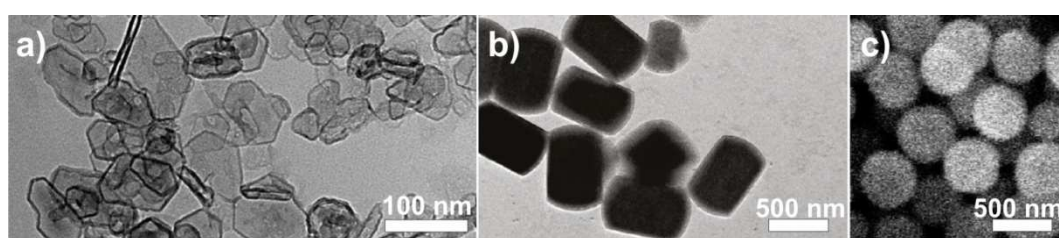

Fig. 14 SEM images of MgF_2 with different morphologies obtained by co-precipitation: a) platelet-like, b) prismatic, and c) spherical aggregates.[68]

Nandiyanto and co-workers were able to synthesize MgF_2 with different morphologies and sizes varying from 6 to 300 nm by simply adjusting the precursor ratios. Particle morphology was mainly influenced by the Mg^{2+} concentration. In line with the LaMer theory, they were able to predict the particle sizes as illustrated in Figure 15.[69]

66) Pietrowski M, Wojciechowska M, *J. Fluorine Chem.* **2007**, *128*, 219-223.
67) Wu D, Wu X, Lv Y, Wang H, *Mater. Lett.* **2008**, *62*, 3003-3006.
68) Sevonkaev I, Matijevic E, *Langmuir* **2009**, *25*, 10534-10539.
69) Nandiyano ABD, Iskandar F, Ogi T, Okuyama K, *Langmuir* **2010**, *26*, 12260-12266.
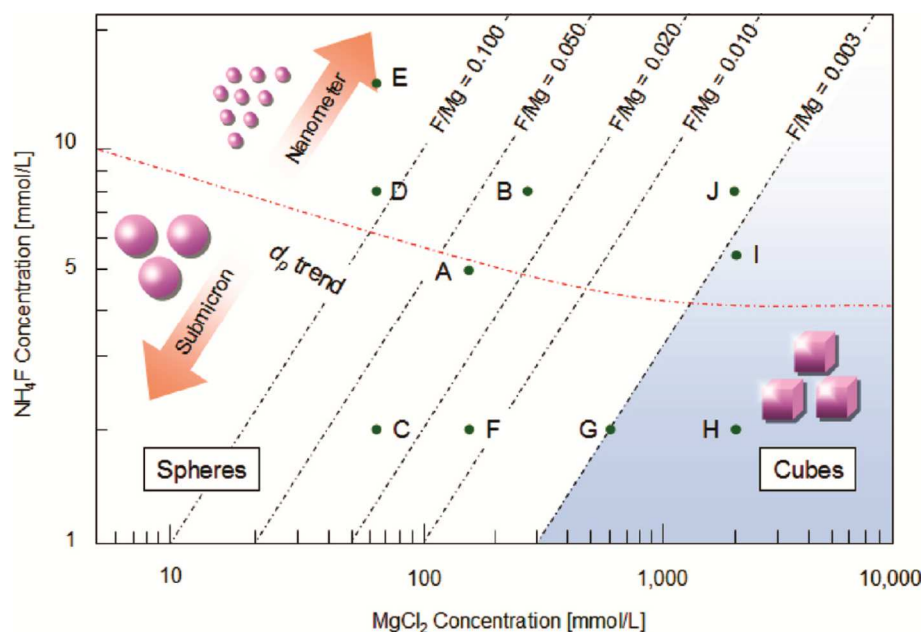
Fig. 15 Synthesis field diagram for the precipitation of MgF_2 particles with different size and morphology in dependence of precursor concentrations.[69]

Addition of surfactants can stabilize particle surfaces and thus influence the particle sizes and morphologies. For example, by adjusting the amount of ethylene diamine (EDTA), Yi and co-workers could tailor the size of $NaYF_4$:Yb,Er between 37 and 166 nm.[70] Further examples of nanoscopic fluorides synthesized via co-precipitation are reviewed in [40] and [64].

Hydro-/Solvothermal
Hydro-/solvothermal methods involve solutions at elevated temperatures and pressures in autoclaves, which lead to an increased solubility of almost any precursor and subsequent crystallization of the product.[41] Important parameters include temperature (usually 120 to 230 °C), pressure, pH value, surfactant, reaction time, autoclave design, and concentrations.[40] In general, particle sizes increase with increasing temperature and reaction time.[64] Typical solvothermal syntheses of nanoscopic fluorides take advantage of surfactants such as EDTA, trisodium citrate, and cethyl trimethyl ammonium bromide (CTAB) in order to control particle size and shape.[41] Solvothermal methods have been useful for the synthesis of different complex fluorides, e.g. $NaYF_4$, $NH_4Er_3F_{10}$, KMF_3 (M = Mn, Co, Ni, Zn or Mg), K_2LnF_5, $KLnF_4$, KLn_2F_7, KLn_3F_{10}, $LiYF_4$, KYF_4 and $BaBeF_4$.[64]

---

70) Yi G, Lu H, Zhao S, Ge Y, Yang W, Chen D, Guo L-H, *Nano Lett.* **2004**, *4*, 2191-2196.

A series of rare earth fluorides (MF_3 and $NaMF_4$ type) were synthesized by Wang and co-workers at temperatures between 100 to 200 °C in a water ethanol mixture treated with linoleate as a surfactant for 8 to 10 h. A strong correlation was observed between the crystal structure of the product and the morphology of the fluoride.[71] CaF_2 nanoparticles with sizes of 20-30 nm were prepared by the hydrothermal method at 160 °C for 24 h without addition of any surfactant. The same group also employed co-precipitation techniques and found less differences compared to the hydrothermal approach in terms of resulting particle sizes and shapes.[72] Previously synthesized MgF_2 nanorods could be converted into $KMgF_3$ nanorods by hydrothermal treatment preserving their morphology.[73]

Hydro-/solvothermal methods constitute a versatile route to nanocrystalline fluorides, the shapes and sizes of which can be controlled by adjusting reaction parameters. However, these methods are relatively time-consuming usually with reaction times up to few days.

Nanoreactors and Micelles

As a matter of course, the size of growing particles cannot exceed their reaction vessel. Thus, by controlling the vessel size, maximum particle size can be restricted. This basic concept of syntheses in so-called nanoreactors can be realized in porous templates such as zeolites, gels or opals, but more commonly self-organizing micelle systems are used.[64] Surface-active molecules like surfactants (long-chain hydrocarbon chains with a hydrophilic head) self-organize into micelles upon reaching a critical concentration. Depending on the surfactant concentration and the polarity of the solvent, micelles can feature different sizes and shapes, and thus influence resulting particles as well.[64] Depending on the system used, oil-in-water or water-in-oil, the hydrophilic heads are orientated outwards or inwards of the micelles, respectively. The latter, in which the water is encapsulated inside of the micelles, is called reverse micelle route. Reverse micelles routes can be performed via two commonly used protocols.

71) Wang X, Zhuang J, Peng Q, Li Y, *Inorg. Chem.* **2006**, *45*, 6661-6665.
72) Omolfajr N, Nasser S, Mahmood R, Kompany A, *J. Nanomedic. Nanotechnol.* **2011**, *2*, 1000116.
73) Cao M, Wang Y, Qi Y, Guo C, Hu C, *J. Solid State Chem.* **2004**, *177*, 2205-2209.

The first one involves the preparation of two different types of micelles, one filled with a fluoride source and another one containing the metal precursors. Upon mixing of these micelles, they can fuse, and subsequently exchange their starting materials leading to fluoride nucleation within the micelle. This mechanism is illustrated in Figure 16.[40]
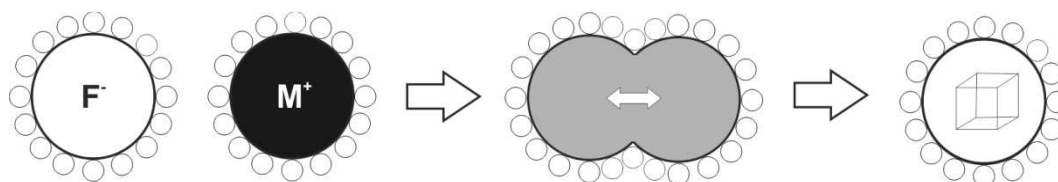

Fig. 16 Scheme of the mechanism involving mixing of reverse micelles containing different starting materials (adopted from [64]).

The second protocol is based on a reaction between components dissolved in the lyophilic media and those contained within the micelles.[40] In both cases, the resulting nanoscopic fluorides can be separated by centrifugation or flocculation upon addition of e.g. acetone or chloroform.[64] Saberi and co-workers prepared spherical MgF_2 with sizes between 9-11 nm by the reverse micelle route. They used polyethylene glycol *tert*-octylphenyl ether as a surfactant to form water in cyclohexane reversed micelles.[74] Nanocrystalline erbium doped BaF_2 was synthesized by reversed micelles in an *n*-butanol-*n*-octane-water mixture stabilized with CTAB. The resulting particles had sizes between 15 and 20 nm.[75] Zhang and co-workers used a mixture of two differently charged surfactants, namely di(2-ethylhexyl) phosphoric acid and a primary amine (N1923), leading to ultra-small micelles. Consequently, the prepared CeF_3 particles show a narrow particle size distribution of about 1.8 nm.[76] A non-aqueous route which involves isopropanol nanoreactors dispersed in polystyrene/THF solution was used for the synthesis of CaF_2 and CaF_3:Eu nanoparticles.[77]

The use of nanoreactors has gained a widespread acceptance for the synthesis of fluorides, and allows for tight control of particle size. However, a drawback of this method is the comparably low production scale as typically milimolar concentrations are used.[40]

74) Saberi A, Negahdari Z, Bouazza S, Willert-Porada M, *J. Fluorine Chem.* **2010**, *131*, 1353-1355.
75) Lian H, Liu J, Ye Z, Shi C, *Chem. Phys Lett.* **2004**, *386*, 291-294.
76) Zhang H, Li H, Li D, Meng S, *J. Colloid Interface Sci.* **2006**, *302*, 509-515.
77) Labéguerie J, Gredin P, Mortier M, Patriarche G, de Kozak A, *Z. Anorg. Allg. Chem.* **2006**, *632*, 1538-1543.

Further Methods

In addition to the strategies mentioned above, ionic liquid approaches have also been applied for the synthesis of nanoscopic fluorides.

Jacob and co-workers introduced a general route to nanoscopic fluorides involving microwave-mediated heating of precursors in ionic liquids. By this method, they were able to produce a variety of fluorides like FeF_2, CoF_2, ZnF_2, LaF_3, YF_3 and SrF_2.[78] Here, ionic liquids can simultaneously serve as solvent, fluoride source, and surfactant. Non-uniform shaped MgF_2 particles with sizes between 20 and 25 nm were synthesized by microwave-mediated ionic liquid synthesis.[45] Just recently, Xu and co-workers published an ionic liquid-based protocol for the synthesis of hollow microspheres of alkaline earth metal fluorides.[79] Besides having several advantages, the preparation of fluorides in ionic liquids appears to offer only reduced control of particle sizes   and   morphologies   compared   to   other   methods.[41]

78) Jacob DS, Bitton L, Grinblat J, Felner I, KoltypinY, Gedanken A, *Chem. Mater.* **2006**, *18*, 3162-3168.

79) Xu J-S, Zhu Y-J, *Cryst. Eng. Comm.* **2012**, *14*, 2630.

2.2 Solution-Based Growth of Thin ZnO Films

The following sections provide an overview of the applications of zinc oxide (ZnO) in transparent conductive thin films. First of all, ZnO and its films are addressed in terms of material properties and high-tech applications, followed by a description of thin films of transparent conductors including ZnO, and of the chemical bath synthesis route towards thin ZnO films.

2.2.1 ZnO and its Thin Films

Zinc oxide (ZnO) has long been known (at least 2000 BC) and ever since been used for applications such as the medical treatment of skin diseases.[80] The Chinese medicine book "Ben Cai Gang Mu" from the 16th century referred to the curing effect of ZnO on skin, eye, and tooth diseases.[81] In the 18th century a new white pigment, so-called "zinc white" or "Chinese white", was introduced to replace the commonly used "white lead" (lead carbonate), which suffers from darkening und toxicity.[80] With the beginning of industrialization, ZnO was used as an additive in the vulcanization process and as an anti-abrasive agent for rubber reinforcement which was later replaced by carbon black.[80] Nowadays, ZnO is widely used as vulcanization activator in the rubber industry, in ceramics such as tiles, as well as as a white pigment and for medical and cosmetic purposes.[80] Besides these applications, which take advantage of the properties of ZnO regarding color, UV absorbance, and hardness, zinc oxide features a wide range of additional properties, such as piezo- and pyroelectricity, which together with its environmental benignity, makes it extremely attractive for high-tech applications.

Structural and Material Properties

Among all materials, ZnO probably has the richest diversity in terms of morphologies as well as material properties.[82] ZnO, known as the mineral zincite, crystallizes in the non-centrosymmetric hexagonal wurtzite structure (point group $C6_v$, space group $P6_3mc$) which is illustrated in Figure 17.[83] Besides zincite, there are two more known crystal structures of ZnO, zinc blende and rock salt, the formation of both of which is not thermodynamically favored at standard conditions.[84]

80) Moezzi A, McDonagh AM, Cortie MB, *Chem. Eng. J.* **2012**, *185-186*, 1-22.
81) Cui J, *Mater. Charact.* **2012**, *64*, 43-52.
82) Hahn Y-B, Korean *J. Chem. Eng.* **2011**, *28*, 1797-1813.
83) Klingshirn C, Fallert J, Zhou H, Sartor J, Thiele C, Maier-Flaig F, Schneider D, Kalt H, *Phys. Status Solidi B* **2010**, *247*, 1424-1447.
84) Wu J, Xue D, *Sci. Adv. Mater.* **2011**, *3*, 127-149.

The zincite structure can be described as hexagonal close-packing oxide ions with half of the tetrahedral sites occupied by zinc cations. From another point-of-view, the structure can also be perceived as a hexagonal diamond (lonsdaleite) structure, where the tetrahedrally coordinated sites are alternatively occupied Zn^{2+} and O^{2-} ions. The main feature of interest of this structure is its polarity, resulting in two oppositely charged basal planes, the positively charged (001) and the negatively charged (00-1) plane.[84] This polarity is in line with the hexagonal symmetry, with the sixfold axis corresponding to the polar axis. The hexagonal crystal systems allows for the formation of anisotropic crystals, with the actual habit depending on the relative growth of the prismatic and the basal planes. Under normal conditions (i.e. in the absence of additives) the growth rate for the different faces decrease in the order [-100] > [-101] > [001] ≈ [00-1].[85]
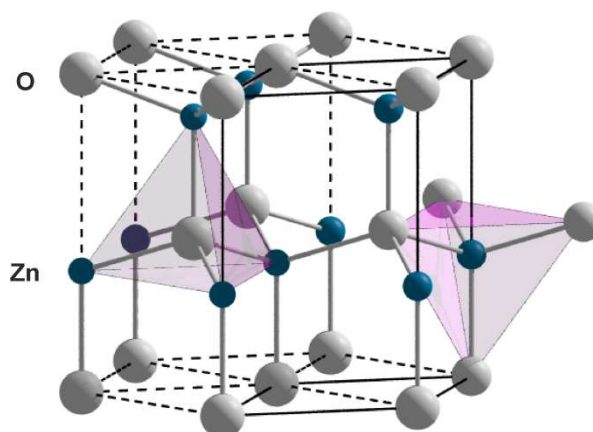

Fig. 17 Hexagonal wurtzite-type structure of ZnO (zincite).

An important structure-related property of ZnO is its piezoelectricity. ZnO possesses the highest piezoelectric constant among all tetrahedrally bounded semiconductors.[81] The structural basic of piezoelectricity is illustrated in Figure 18. In short: Applying of an external mechanical force leads to a lattice distortion which displaces the centers of charge resulting in an external electric potential and *vice versa*.[84] Piezo- and pyroelectricity are used in a variety of applications such as transducers, actuators, and sensors.[82,86] Recently, so-called "nanogenerators" based upon the piezoelectricity of ZnO nanowires were designed. Such systems could be employed as a power supply or engine for nanodevices.[84]

85) Vayssieres L, Keis K, Hagfeldt A, Lindquist S-E, *Chem. Mater.* **2001**, *13*, 4395-4398.
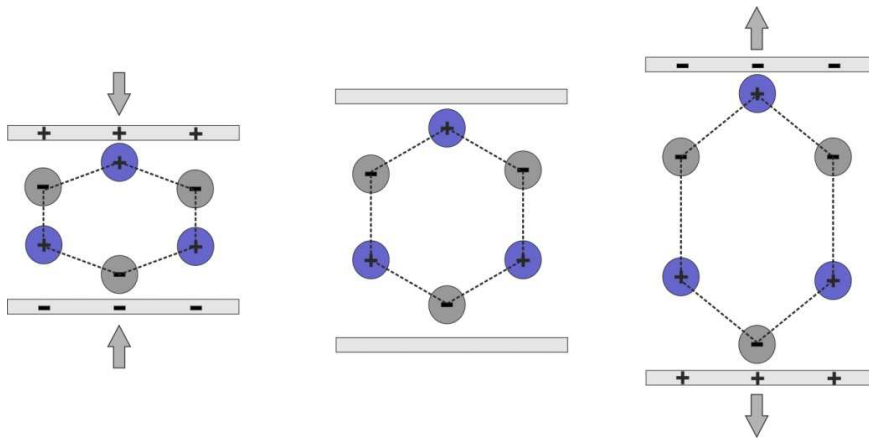86) Janotti A, Van de Walle CG, *Rep. Prog. Phys.* **2009**, *72*, 126501.

Fig. 18 Piezoelectricity: Scheme of electrical polarization induced by application of a mechanical force; the inverse piezoelectric effect functions the other way around (adopted from [84]).

Zincite crystals show a strong change in conductivity in the presence of adsorbed species on their surface.[86] For this reason, ZnO films have been employed for gas-sensing purposes.[88-90] Recent developments aim at the usage of ZnO as bio-sensor for e.g. cholesterol and glucose at minimum sizes, since a high surface-to-volume ratio of the sensor leads to significantly shorter diffusion pathways and thus to an enhanced sensor performance.[91] ZnO is the pivotal component of variable resistors, so-called "varistors", where its non-linear current-voltage correlation is utilized. The origin of this non-ohmic resistance of ZnO is still not fully understood, but is frequently attributed to grain boundary effects.[86]

Besides its transparency which is addressed in the subsequent subsection, ZnO also provides other useful optical properties, such as room-temperature emission in the UV band and in the visible regime which makes it suitable for light emitting diode (LED) applications. While the UV emission at about 380 nm can be attributed to exciton recombination near the band edge, the origins of the visible band is controversially discussed.[83,84] It is assumed that intrinsic defects, such as vacancies or interstitials in the crystal lattice are the causes for some visible emission bands, however this still is highly uncertain.[83] Other emission bands were attributed to impurities like substitutional Cu_{Zn} (green emission) or Li and Na (red to yellow emission).[83] Moreover, ZnO features strong optical nonlinearities due to which it can be used as an optical modulator.[92]

87) Mitra P, Chatterjee AP, Maiti HS, *J. Mater. Sci. – Mater. Electron.* **1998**, *9*, 441-445.
88) Chatterjee AP, Mitra P, Mukhopadhyay, *J. Mater. Sci.* **1999**, *34*, 4225-4231.
89) Vijayan TA, Chandramohan R, Valanarasu S, Thirumalai J, Subramanian SP, *J. Mater. Sci.* **2008**, *43*, 1776-1782.
90) Lokhande CD, Gondkar PM, Mane RS, Shinde VR, Han S-H, *J. Alloys Compd.* **2009**, *475*, 304-311.
91) Ahmad M, Zhu J, *J. Mater. Chem.* **2011**, *21*, 599-614.
92) Van de Walle CG, *Phys. Status Solidi B* **2002**, *1*, 221-228.

ZnO provides high thermal conductivity, thus it can serve as substrate for deposition of other materials such as GaN, to which it has a very small lattice mismatch.[92] Furthermore, the bandgaps of wurtzite GaN and ZnO are similar (3.44 and 3.37 eV at room temperature) which led to substantial research efforts trying to replace GaN in optoelectronic applications by ZnO.[86] The availability of large single crystals and its good etchability favor ZnO, however, controlling the p- and n-type conductivity is still a problem.[86] One of the properties of ZnO which has also arisen much interest, is its semiconductivity coupled with its transparency in the visible regime. It is exactly these properties, which characterize the group of transparent conductive oxides (TCOs), which are indispensable for many optoelectronic devices. The properties as well as the technological importance of TCOs are addressed in detail in subsection 2.2.2

While ZnO can be used in classical photovoltaic cells as a transparent conductor to dissipate the electrical charge, it can also play an additional role in dye-sensitized solar cells (DSSCs). DSSCs, so-called Grätzel cells, are a new class of solar cells with an entirely different working principle.[84] In a broader sense, DSSCs are mimicking natural photosynthesis.[84] The DSSC setup consists of a dye-sensitized photoanode and a platinum or carbon cathode, separated by an electrolyte layer sandwiched between transparent conductor coated glass plates (see Figure 19). Irradiation excites the dye molecules, which then transfer electrons to the photoanode and into the electrical circuit. Excited dye molecules are reduced to the ground state by a redox couple (e.g. I_3^-/I^-) that in turn is reduced at the cathode by electrons from the electrical circuit.[84]
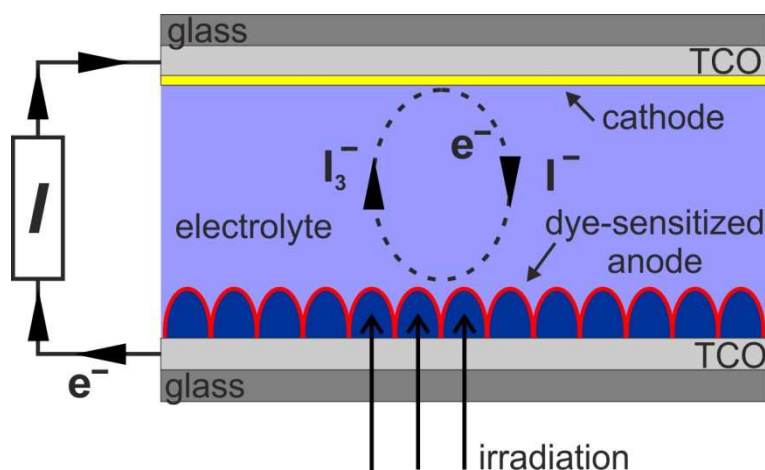

Fig. 19 Scheme of the working principle of a dye-sensitized solar cell (DSSC) (adopted from [84]).

The anode material, which is typically based on semiconducting TiO_2 nanoparticles, is crucial for the whole process. However, ZnO is expected to have considerable advantages over TiO_2 in terms of higher electron mobility, less recombination losses, and a huge variety of morphologies and synthesis routes.[84,93] Especially ZnO nanorod arrays have awaken much interest as a potential photoanode material.[94]

93) Kovalenko A, Pourroy G, Crégut O, Gallart M, Hönerlage B, Gilliot P, *J. Phys. Chem C* **2010**, *114*, 9498-9502.
94) Guo M, Diao P, Wang X, Cai S, *J. Solid State Sci.* **2005**, *178*, 3210-3215.

ZnO Thin Film Deposition

ZnO films have been prepared by various methods, among these are diverse physical deposition techniques, such as laser ablation,[95-97] magnetron sputtering,[98] and chemical vapor deposition (CVD).[99,100]

CVD has been extensively used for the preparation of ZnO nanostructures.[101] It can either proceed via a vapor-liquid-solid (VLS) or vapor-solid (VS) mechanism. The latter is based on vaporization of precursors followed by condensation onto a substrate at lower temperature.[82] The VLS mechanism, in contrast, is a catalyst-assisted process during which the vapor phase dissolves within the catalyst thus forming alloy droplets. Finally, upon supersaturation of the droplets, precipitation occurs and the film grows.[82]

While physical methods yield high-quality films and are well-established, they have the disadvantages of high-cost equipment and limitations regarding up-scaling.[5,6,102] Wet-chemical approaches, such as sol-gel,[103] successive ionic layer adsorption and reaction (SILAR),[104] electrodeposition,[105] and chemical bath deposition (CBD)[106] overcome those disadvantages and have emerged as alternative techniques.

Furthermore, solution-based deposition methods allow the processing of large area substrates and substrates which might not tolerate elevated temperatures.[90,107] Deposition is possible even on porous and complex substrate structures via infiltration, as solution-based approaches do not rely on line-of-sight principle as physical methods.[107,108]

The growth of ZnO films by solution based approaches and by chemical bath deposition in particular is addressed in subsection 2.2.3.

95) Jin BJ, Im S, Lee SY, *Thin Solid Films* **2000**, *366*, 107-110.
96) Bentes L, Ayouchi R, Santos C, Schwarz R, Sanguino P, Conde O, Peres M, Monteiro T, Teodoro O, *Superlattices Microstruct.* **2007**, *42*, 152-157.
97) Vinodkumar R, Navas I, Chalana SR, Gopchandran KG, Ganesan V, Philip R, Sudheer SK, Pillai VPM, *Appl. Surf. Sci.* **2010**, *257*, 708-716.
98) Kim D-K, Kim H-B, *J. Alloys Compd.* **2012**, *522*, 69-73.
99) Barnes TM, Leaf J, Fry C, Wolden CA, *J. Cryst. Growth* **2005**, *274*, 412-417.
100) Pflitsch C, Nebatti A, Brors G, Atakan B, *J. Cryst. Growth* **2012**, *348*, 5-9.
101) Cao B, Cai W, *J. Phys. Chem. C.* **2008**, *112*, 680-685.
102) Minami T, *Semicond. Sci. Technol.* **2005**, *20*, 35-44.
103) Caglar Y, Caglar M, Ilican S, *Curr. Appl. Phys.* **2012**, *12*, 963-968.
104) Shishiyanu ST, Shishiyanu TS, Lupan OI, *Sens. Actuators B* **2005**, *107*, 379-386.
105) Khajavi MR, Blackwood DJ, Cabanero G, Tena-Zaera R, *Electrochim. Acta* **2012**, *69*, 181-189.
106) Baxter JB, Schmuttenmaer CA, *J. Phys. B* **2006**, *110*, 25229-25239.
107) Niesen TP, De Guire MR, *J. Electroceram.* **2001**, *6*, 169-207.
108) Parikh H, De Guire MR, *J. Ceram. Soc. Jpn.* **2009**, *117*, 228-235.

2.2.2 Transparent Conductive Oxides

Transparent, electrically conductive films are an essential part of optoelectronic devices, such as photovoltaic cells and flat panel displays. The coexistence of transparency and conductivity can be achieved with different materials e.g. extremely thin metal films of silver, gold, or copper.[109] The first report of a non-metallic transparent conductive film dates back to 1907. Badeker and co-workers deposited a thin metallic cadmium film that became transparent upon incomplete oxidation while retaining its conductivity.[110,111] During the last 50 years, these so-called transparent conductive oxides (TCOs) have been established in manifold applications such as flat panel displays and photovoltaic cells.[109] The most prominent among them is tin-doped indium oxide (also called indium-tin oxide or ITO).

This section addresses general aspects how transparency and conductivity in TCOs coexist, highlights the advantages and disadvantages of the different TCOs and provides some application examples.

General Aspects

Usually, inorganic solids with wide band-gaps are classified as electrical insulators and are thus widely used as electrical shielding materials.[112] Due to the strong ionic character between metal cations and oxide ions, the 2p states of the oxide ions lie far below the valence orbitals of metallic cations, and consequently, many metal oxides feature a wide band-gap.[112] This strong ionicity suppresses the promotion of electrons to the conduction band (CB) and thus leads to high electrical resistivities.[112]

However, oxides and mixed oxides of the p-block metal cations with ns0 configuration (where n is the principle quantum number) such as ZnO, CdO, In_2O_3, Tl_2O_3, SnO_2 and so forth, can be doped to yield n-type conductivity.[112] The two main characteristics of TCOs, their transparency and conductivity are addressed in the following: The transmission window of TCOs, typically between 400 to 1500 nm, is confined by two borders, the near-UV and the near-IR region, respectively.[113] The near-UV region is limited due to the fundamental band-gap E_g of the TCO, and consequently, photons with the same or higher energy quantum are absorbed. For this reason, the fundamental band-gap should be at least 3.1 eV (approx. 400 nm) for most TCO applications. This limitation does not refer to TCOs with indirect band gaps, such as CdO.

109) Granqvist CG, Hultåker A, *Thin Solid Films* **2002**, *411*, 1-5.
110) Lewis BG, Paine DC, *MRS Bull.* **2000**, *25*, 22-27.
111) Liu H, Avrutin V, Izyumskaya N, Özgür Ü, Morkoç H, *Superlattices Microstruct.* **2010**, *48*, 458-484.
112) Kawazoe H, Yanagi H, Ueda K, Hosono H, *MRS Bull.* **2000**, *25*, 28-36.
113) Coutts TJ, Young DL, Li X*, MRS Bull.* **2000**, *25*, 58-65.

In this case the band gap is only approx. 1 eV; however, it is indirect and thus absorption of photons is unlikely which causes CdO's transparency.[114] The near-IR region is confined due to the plasma edge of the material. Reflection occurs, when the striking photons resonate with the electrons in the valence band.[111] The plasma wavelength is linked to the effective electron mass and electron concentration in the valence band of the material and decreases with increasing electron concentration.[6] Consequently, as shown in Table 1, high carrier concentrations in the valence band, responsible for low resistivities of the material, simultaneously impair the optical transmittance of the material at higher wavelength – a phenomenon which can be observed in the reflectance of metals. The gold-color reflections of TiN, a TCO whose plasma edge is very close to the optical spectrum, can be frequently seen on glass facades of large office building, where it is used to reflect IR irradiation for cooling purposes.[6]

Table 1: Approx. minimum resistivities and plasma wavelengths of some TCOs (according to [6]).

material	resistivity / $\mu\Omega$*cm	plasma wavelength / nm
Ag	1.6	400
TiN	20	700
In_2O_3:Sn (ITO)	100	>1000
ZnO:Al (AZO)	150	>1300
SnO_2:F (FTO)	200	>1600
ZnO:F	400	>2000

Typical transmittances of TCO films are about 85% when averaged from 400 to 1100 nm and weighted by the solar spectrum.[110]

Despite the extensive use of TCOs nowadays, the origin of their conductivity is still not fully understood.[114] As mentioned previously, TCOs feature wide band-gaps which makes electron transitions from the valence band (VB) into the conduction band (CB) via absorption of phonons impossible. Consequently, due to a lack of charge carriers in the VB, those materials display moderate conductivities. For this reason, TCOs are usually impurity doped, resulting in charge carrier concentrations in the order of 10^{20} cm^{-3}.[102] In contrast to semiconducting silicon for chip production, doping levels of TCOs are much higher, usually in the range of a few percent, to obtain those charge concentrations. In case of ZnO, impurity doping can be achieved by replacing Zn^{2+} with cations of higher valence e.g. with group III or IV elements, such as boron, aluminum, gallium, germanium, titanium and so forth, or substitution of O^{2-} by F^-.[115]

114) King PDC, Veal TD, *J. Phys. Condens. Matter* **2011**, *23*, 334214.
115) Minami T, *MRS Bull.* **2000**, *25*, 38-44.

Such dopants act as shallow donors, i.e. they create electron-occupied states just below the CB of the host (see Figure 20). Those extra electrons are easily excited into the CB which increases the free charge carrier concentration and, consequently, decreases the resistivity.[8] The introduction of additional charge carriers by donor impurities is referred to as n-type doping. The effect of different n-type dopants on the charge carrier concentration and resistivity of ZnO films is shown in Table 2.

Table 2: Resistivities and charge carrier concentrations of ZnO films doped with different impurities (according to [115]).

dopant	dopant content / at.%	resistivity / $10^{-4}\ \Omega^{*}cm$	carrier concentration / $10^{20}cm^{-3}$
Al	1.6-3.2	1.3	15.0
Ga	1.7-6.1	1.2	14.5
B	4.6	2.0	5.4
In	1.2	8.1	3.9
Ti	2.0	5.6	6.2
F	0.5	4.0	5.0

Various TCOs such as ZnO feature an unintentional n-type conductivity whose origin is still under debate. Traditionally, this n-type conductivity was attributed to native point defects.[92] However, recent investigations indicate that the conductivity stems from substitutional hydrogen on oxygen sites; hydrogen is present in almost all deposition methods.[8,92]

Contrarily to n-type, p-type doping does not create additional charge carriers in the conduction band, but introduces defect levels proximate to the VB (see Figure 20).[116] In this case, electron holes which are strongly localized and at deeper energy levels than the VB, represent the majority of charge carriers.[117] Charge transport in p-type conductors is considered as a positive hole movement, although actually it is not the virtual holes which move. p-type conductivity for a TCO, namely NiO, was first reported in 1993, and has recently been found in materials such as $CuAlO_2$, $CuGaO_2$, $SrCu_2O_2$, $AgInO_2$, ZnO:N, and ZnO:P.[102,109,118] So far, there is no p-type TCO thin film in practical use.[102] Reasons for this may be that p-type films exhibit considerably lower conductivity than n-type films, owing to strong localization of positive holes, and problems concerning the reproducibility and stability of p-type conductivity in some cases.[7,116]

116) Exarhos GJ, Zhou X-D, *Thin Solid Films* **2007**, *515*, 7025-7052.
117) Pasquarelli RM, Ginley DS, O'Hayre R, *Chem. Soc. Rev.* **2011**, *40*, 5406-5441.
118) Fang X, Li J, Zhao D, Shen D, Li B, Wang X, *J. Phys. Chem. C.* **2009**, *113*, 21208-21212.
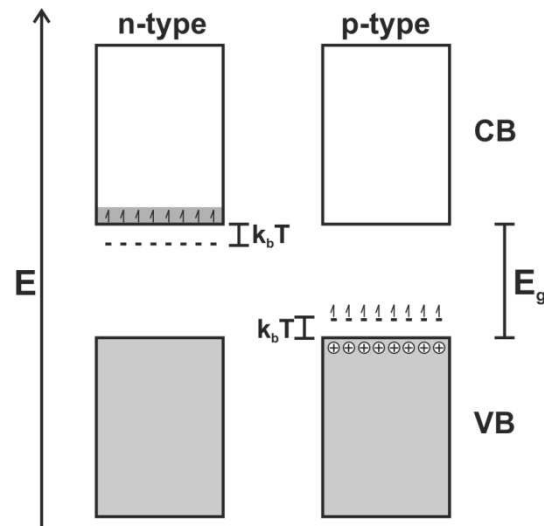
Fig. 20 Schematic band structures of n- and p-type semiconductors.

Important parameters, which define the conductivity or resistivity of a material, respectively, are the free carrier density, depending on the extra carriers introduced by the dopant, and the carrier mobility, which is governed by their effective mass and scattering mechanisms.[116] The mobility (μ) of a charge carrier is linked to the average scattering time (τ) and the effective mass (m*) as shown in the equation:[117]

$$\mu = \frac{e\tau}{m*}$$

(with e as the elementary charge)

Electron scattering in the CB can occur by thermal vibration of the lattice (phonons), structural defects (vacancies, stacking faults, etc.), grain boundaries, and ionized impurities.[111] The ionized impurities, or in other words the dopants, are the major scattering mechanism limiting the electron mobility in TCOs.[111] This can be considered as a "double-edged sword". Increasing the free electron density by introducing large amounts of dopants leads to an increase of scattering events and consequently, to low electron mobilities and high resistivities. Furthermore, high electron densities in the CB decrease the plasma wavelength, as mentioned above. Contrarily, introduction of fluoride dopants does not lead to relevant increase of scattering. Whereas the VB of a TCO typically results from oxygen 2p states, the CB of TCO is mainly derived from metal states. Thus, the CB will receive strong perturbations due to metal ion doping, whereas fluoride substitutes on   oxygen   positions,

which perturbs states in the VB, leave the CB unaffected.[6] The effective electron mass is linked to the dispersion of the CB, i.e. the higher the dispersion, the lower the effective mass.[119] In p-type TCOs, the oxygen 2p orbitals are strongly localized, resulting in large effective masses of the holes, and consequently, low carrier mobilities and high resistivities.[117] Due to a lack of fundamental knowledge, research efforts on improving TCO properties were mainly carried out empirically in the last 60 years.[116] Freeman and co-workers formulated empirical conditions to confine the class of TCOs: i) a highly dispersed s band at the bottom of the CB, ii) VB and CB are separated by a fundamental bandgap large enough to exclude visible absorption and iii) band conditions such as the plasma wavelength is above the visible range.[119] Just to increase film thickness in order to obtain better resistivities is not straightforward, since this results in reduced transparency. A practical method to judge the performance of TCO films is the ratio of the electrical conductivity σ to the visible absorption coefficient α.[6] Those figures of merit of common TCOs films are given in Table 3, in which high values are indicative on an enhanced performance.

Table 3: Figures of merit for some TCOs (according to [6]).

material	sheet Resistance Ohm*sq	vis. absorption coefficent	figure of merit
ZnO:F (FZO)	5	0.03	7
ZnO:Al (AZO)	3.8	0.05	5
In_2O_3:Sn (ITO)	6	0.04	4
SnO_2:F (FTO)	8	0.04	3
ZnO:Ga (GZO)	3	0.12	3
ZnO:B	8	0.06	2
SnO_2:Sb	20	0.12	0.4
ZnO:In (IZO)	20	0.20	0.2

*values are given for the best samples; prepared via chemical vapor deposition

Despite material related differences in terms of electrical and optical performance of TCOs, the deposition method and condition, as well as post-treatment, and even the substrate may influence the figures of merit.[102] Figure 21 displays the improvement of the electrical performance of three TCOs over the years.

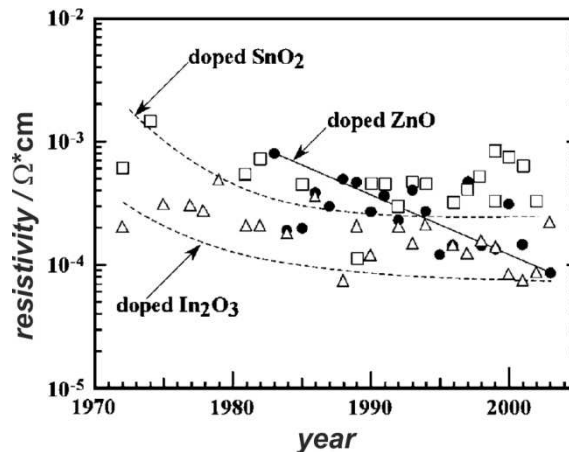119) Freeman AJ, Poeppelmeier KR, Mason TO, Chang RPH, Marks TJ, *MRS Bull.* **2000**, *25*, 44-51.

Fig. 21 Annually reported minimum resistivities of TCO films.[102]

It is noteworthy that when comparing the TCO resistivities in Figure 3, the resistivity of doped ZnO films continuously decreased during the last two decades, whereas those of doped SnO_2 and ITO films remained almost constant.

Applications of TCOs
There is a huge variety of TCO applications and thus it is not surprising that there is no perfect TCO for all applications. TCO materials can strongly differ in terms of electrical and optical performance, and price. Contrary to the common belief, the majority of TCOs is not consumed for flat panel displays (FPD) but for low emissivity ("low-e") glass.[111] In this application, the IR reflectivity of TCOs is utilized for thermal managements, such as oven windows that are safe to touch and architectural glass for large window facades which permit a pleasant interior climate.[6] Most suitable for "low-e" glass is SnO_2:F owing to its short plasma wavelength, and most importantly due to its low price and good durability.[6] Large amounts of glass are coated with SnO_2:F by cost-efficient direct-spray pyrolysis.[110] In hot climates, TiN with its shorter plasma wavelength (compare Table 1) is preferred for architectural glass applications.[6]

Unlike to the above-mentioned passive applications, in which the electrical conductivity of TCOs is not relevant, TCOs are also used for active functional glasses. Those applications include defrosting of vehicle windows and electrochromic windows in which transparency or color can be controlled via electrically induced redox reactions of an interlayer.[110] Other smart window applications are security circuits or antennas, implemented invisibly in the glass.[6]

For application in FPDs, both, very low resistivity and high optical transparency is required. Although the construction of FPDs can differ significantly, the role of TCOs remains the same.[110] The TCO is used to apply an electrical field to orientate liquid crystals which are sandwiched between two glass plates.[110] Thereby, each pixel can be individually addressed through an etched structure of the TCO.[110] Thin films for FPD application require more than 90% transparency in the visible regime and resistivities in the range of 1-3*10^{-4} Ω*cm (typical sheet resistances of < 15 Ω/sq.).[110] ITO is the best candidate for fitting those criteria, and is deposited for best electrical performance by dc-magnetron sputtering on hot (300-400 °C) substrates.[110] In the dated technology of cathode-ray tubes, TCOs were used for electromagnetic shielding. Relatively moderate sheet resistances of 2 kΩ/sq were achieved by either sputtering or spin-coating of ITO suspensions.[110]

Another important application for TCOs are photovoltaic cells where they serve as the front electrode dissipating the electrical charge.[6] Depending on cell design SnO_2:F or ZnO:Al films serve this market for reasons of low price, and in case of SnO_2:F for excellent hydrogen and temperature resistance, necessary for device fabrication.[5,111,115] ZnO doped with Ga(III) or Al(III) has gained much interest as a transparent contact in GaN-based light emitting diodes (LEDs) due to its low lattice mismatch with GaN which permits epitaxial growth.[111] TCOs are also an essential part in touch-panel displays for, e.g. ATM or smart phone screens. This application only requires moderate sheet resistances up to 100 Ω/sq., making low cost SnO_2:F with its outstanding durability the best TCO for this application.[6]

The FPD market is the fastest-growing market for TCOs, and although ITO fits the demanding criteria best at the moment, researchers put a lot of effort in finding alternatives.[110] This effort is motivated by the scarcity and high price of indium whose annual supply is about 574 metric tons (in 2010)[120] of which about 80% go into FPD production.[110,111] There are no indium mines; indium is a byproduct of lead and zinc mining, and thus its availability strongly depends on the production of these metals.[6] It should be mentioned that indium is recyclable to a large extent (approx. 80-90%)[111] and the price of indium in a common LCD TV amounted only 50 $ cents in 2003.[121] However, strong price fluctuations appear due to reduced zinc degradation rates and an increasing demand of ITO in FPDs. Thus it is expected that indium becomes a strategic resource.[111] Present developments aim at replacing   ITO   with   low   coast   TCOs   such   as   doped   ZnO.

120) Tolcin AC, *U.S. Geological Survey, Mineral Commodity Summaries* **2011**.
121) George MW, *U.S. Geological Survey, Minerals Yearbook* **2003**.

Gallium and aluminum doped ZnO (GZO and AZO) seems to be a promising alternatives to ITO, especially in terms of the continuing improvement of their electrical performance (also compare Figure 21).[102]

Other research efforts aim at developing flexible electronic devices such as "e-papers", flexible displays, solar cells, light-emitting devices and so forth, which require TCOs capable of accommodating large strains.[110] The currently available ITO on flexible plastic substrate displays a resistivity of $10^{-3} \, \Omega \text{*cm}$ which is about an order of magnitude higher than ITO on glass.[122] Graphene layers on flexible substrates show excellent strain resistances and can be bent-up to 138°, whereas ITO films in contrast are irreversibly damaged when bent more than 60°.[117] However, resistivity of graphene is several hundred times higher than that of ITO at comparable transmittances.[117] Alternatives may be carbon nanotubes (CNTs) and conductive polymers such as poly(3,4-ethylenedioxythiophene) (so-called PEDOT).[111,117]

Another promising research field is the development of p-n junctions entirely made up of TCOs, which allows the fabrication of transparent electronic devices.[5] Recently, the fabrication of LEDs based on a p-n ZnO:P/ZnO homojunction or on a NiO/ZnO heterojunction have been reported.[118,123]

2.2.3 Chemical Bath Deposition of ZnO

Chemical bath deposition (CBD) encompasses the solution-based growth of a ceramic material on substrates at temperatures below 100 °C in a single immersion step.[107] The produced films are polycrystalline or amorphous, and provide film thicknesses typically in the range of 100 to 1000 nm with deposition rates from 2 to 20.000 nm/h.[107] CBD, was originally used for the deposition of chalcogenide films, but has also been extensively used for oxide films since the 1980s.[107] It has attracted much interest for the deposition of ZnO films, since CBD is capable of low-cost deposition on large area substrates. Besides CBD, there are several related solution-based techniques such as successive ionic layer adsorption and reaction (SILAR), electroless deposition, and liquid-phase deposition (LPD).[107] Research efforts concerning CBD growth of ZnO are largely focused on the growth of ZnO nanorod arrays rather than dense films. Here, CBD growth of nanorod arrays is addressed as well. Recent publications on chalcogenide and oxide films prepared via CBD and their bath conditions are listed in a review article by Pawar and co-workers.[124]

122) Lee A-N, Hsu SF, Hwang SW, Chen CH, *Curr. Appl. Phys.* **2004**, *4*, 651-654.

123) Lee GJ, Min S-K, Oh C-H, Lee Y, Lim H, Cheong H, Nam HJ, Hwangbo CK, Min S-K, Han S-H, *J. Nanosci. Nanotechnol.* **2011**, *11*, 511-517.

124) Pawar SM, Pawar BS, Kim JH, Joo O-S, Lokhande CD, *Curr. Appl. Phys.* **2011**, *11*, 117-161.

General Aspects

Bath solutions for oxide deposition contain at least one metal salt, OH^- for hydrolysis, and usually a complexing agent (ligand).[107] The overall process during CBD can be described as an interplay between the different stabilities of species in solution and in the solid.

Upon addition of a Zn(II) salt to an aqueous solution the salt dissociates and the Zn(II) ions are immediately solvated by water molecules. Due to the amphoteric character of Zn(II) several hydroxyl species can exist, whose stability is governed by the solution pH.[125] Considering that initially the hexaaqua complex $[Zn(H_2O)_6]^{2+}$ is formed, this complex can be deprotonated to $[Zn(H_2O)_5OH]^+$ and further to insoluble $[Zn(H_2O)_4(OH)_2]_{(s)}$ complexes. The latter is commonly written as $Zn(OH)_{2(s)}$. When increasing the pH of the solution, $Zn(OH)_{2(s)}$ dissolve again, forming the negatively charged $[Zn(OH)_4]^{2-}_{(aq)}$ complex. When ammonia is used as base, it cannot only deliver OH^- ions, but it can also serve as a ligand, forming the $[Zn(NH_3)_4]^{2+}_{(aq)}$ ammonia complex. However, at elevated temperatures, this ammonia complex is unstable and the hydroxyl complex is formed.[126]

The driving force for ZnO film formation is a decrease in the stability of the Zn(II) complexes through pH adjustments and/or temperature increase, which then causes supersaturation and hence precipitation of $Zn(OH)_2$. Finally, ZnO is formed by dehydration of $Zn(OH)_2$ and the films can continue to grow through condensation of Zn(II) species.[126,126]

Two possible mechanisms can take place during CBD, heterogeneous nucleation at low degrees of supersaturation leading to the condensation of Zn(II) species at the substrate/solution interface, and homogeneous nucleation at very high degrees of supersaturation whereby colloidal particles precipitate in bulk solution followed by attachment at the substrate.[127-130] While homogenous nucleation yields well-adhering and dense films, heterogeneous nucleation predominantly produces porous, poorly-adhering films.[108,127] In homogeneous nucleation, the film density and particle sizes are dictated by the degree of supersaturation.[108]

125) Greene LE, Yuhas BD, Law Matt, Zitoun D, Yang P, *Inorg. Chem.* **2006**, *45*, 7535-7543.

126) Jacobs K, Balitsky D, Armand P, Papet P, *Solid State Sci.* **2010**, *12*, 333-338.

127) Ortega-López M, Avila-García A, Albor-Aguilera ML, Resendiz VMS, *Mater. Res. Bull.* **2003**, *38*, 1241-1248.

128) Drici A, Djeteli G, Tchangbedji G, Derouiche H, Jondo K, Napo K, Bernède JC, Ouro-Djobo S, Gbagba M, *Phys. Status Solidi A* **2004**, *201*, 1528-1536.

129) Wang M, Kim EJ, Hahn SH, Park C, Koo K-K, *Cryst. Growth Des.* **2008**, *8*, 501-506.

130) Kawano T, Imai H, *J. Ceram. Soc. Jpn.* **2010**, *118*, 969-976.

Parameters Influencing CBD

There are several factors that govern the deposition and morphology of CBD-grown ZnO films and nanorod arrays. Important parameters include complexing ligands, Zn(II) sources, substrates, solution pH, ionic strength, and growth time.

Ligands

Complexing agents or ligands such as ethylenediamine,[128,131,132] triethenamine (TEA),[133,134] dimethylamine-borane,[101,135] and hexamethylenamine (HMTA)[106,125,136-139] are frequently used in CBDs. The general role of these ligands is to keep the supersaturation at low levels by competing for the coordination sites of the Zn(II) species, and thereby decreasing the formation rate of the solid phase.[107,130,140] One of the most often utilized ligands is HMTA, which itself is a weak ligand for Zn(II), but slowly decomposes (independently from ZnO formation) into formaldehyde and ammonia.[140] Ammonia in turn acts as source of OH$^-$ and complexing agent, as already discussed above.[136] McPeak and co-workers showed in an infrared spectroscopy study that HMTA cannot play a further additional role in specific adsorption on crystal faces, as often proposed.[141] However, there is a certain linkage between the used ligand and the yielded ZnO morphologies. Baths containing ethylenediamine tend to precipitate ZnO crystals with star-like morphologies, while those containing HMTA yield ZnO rods, and those containing TEA spherical aggregates.[140] Kumar and co-workers investigated the influence of different concentrations of TEA. Whereas at low TEA concentrations random aggregation occurs, leading to spindle-like structures, high concentrations promote an oriented aggregation leading to flower-like structures.[134] A distinct influence of different concentrations of *N,N,N′,N′*-tetramethylethylenediamine on the alignment and nanorod diameters was observed by Fragalà and co-workers. Higher concentrations of the ligand led to almost intergrown ZnO films.[142]

131) Shishiyanu ST, Lupan OI, Monaico EV, Ursaki VV, Shishiyanu TS, Tiginyanu IM, *Thin Solid Films* **2005**, *488*, 15-19.

132) Querfelli J, Regragui M, Morsli M, Djeteli G, Jondo K, Amory C, Tchangbedji, Napo K, Bernède JC, *J. Phys. D: Appl. Phys.* **2006**, *39*, 1954-1959.

133) Wang R, Xin JH, Tao XM, Daoud WA, *Chem. Phys. Lett.* **2004**, *398*, 205-255.

134) Kumar PS, Raj AD, Mangalaraj D, Nataraj D, Ponpandian N, Li L, Chabrol G, *Appl. Surf. Sci.* **2011**, *15*, 6678-6686.

135) Cao B, Cai W, Li Y, Sun F, Zhang L, *Nanotechnol.* **2005**, *16*, 1734-1738.

136) Ashfold MNR, Doherty RP, Ndifor-Angwafor G, Riley DJ, Sun Y, *Thin Solid Films* **2007**, *515*, 8679-8683.

137) Chu D, Hamada T, Kato K, Masuda Y, *Phys. Status Solidi A* **2009**, *206*, 718-723.

138) Eskandari M, Ahmadi V, Ahmadi SH, *Physica E* **2010**, *42*, 1683-1686.

139) Hsu C-H, Chen W-S, Lai C-H, Yan S-F, *Adv. Mater. Res.* **2011**, *194-196*, 2254-2258.

140) Govender K, Boyle DS, Kenway PB, O'Brien P, *J. Mater. Chem.* **2004**, *14*, 2575-2591.

141) McPeak KM, Le TP, Britton NG, Nickolov ZS, Elabd YA, Baxter JB, *Langmuir* **2011**, *27*, 3672-3677.

142) Fragalà ME, Aleeva Y, Malandrino G, *Superlattices Microstruct.* **2010**, *48*, 408-415.

Zn(II) Precursors

With otherwise constant bath conditions, the use of different Zn(II) sources often results in different film morphologies which may arise through different kinetics and/or promoting or inhibiting effects of the counter ion.[140] A special case is the volatility of some counter ions such as carboxylates.[140] The effect of sulfate, nitrate, and acetate precursors on the morphology of CBD grown ZnO was investigated by Chu and co-workers.[137] Whereas hexagonal nanorods and columns were grown using nitrate and acetate precursors, respectively, sulfate precursors led to nanodisks (see Figure 22). The authors pointed out, that the different morphologies may result from slight differences in supersaturation or adsorption phenomena.[137]
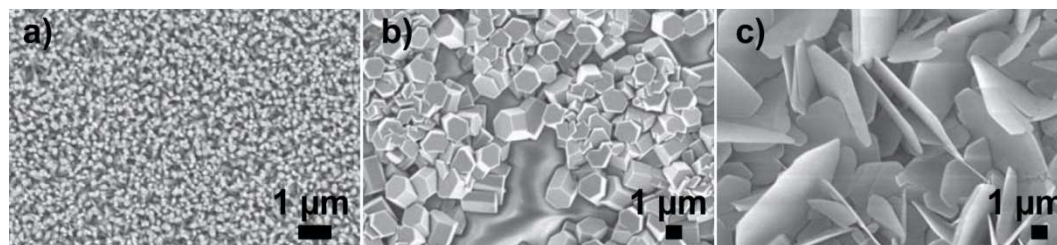

Fig. 22 SEM micrographs of ZnO films grown in CBD with different Zn(II) precursors: a) nitrate, b) acetate and c) sulfate.[137]

Substrate

The role of the substrate can be crucial for film properties such as adhesion, crystallographic orientation, and density. In general, deposition can be performed either non-epitaxial on bare substrates, homoepitaxial on ZnO or ZnO-seeded substrates, or heteroepitaxial. First of all, the substrate has to be cleaned thoroughly in a first step to ensure homogeneous film growth and film adhesion. Depending on the group, cleaning procedures vary. Cleaning can be accomplished for instance with piranha solution followed by rinsing with water,[101,143] or sequentially washing with water, ethanol, and acetone,[129] or cleaning in an ultrasonic bath[7]. Under otherwise identical bath conditions, the morphologies of the films can differ significantly depending on the substrate. Also the diameter of nanorods grown via CBD is linked to the substrate used.[140] Growth condition are very narrow for CBD on bare substrates which do not promote epitaxial growth, thus seeding has been widely established to enhance film quality.[7]

143) Hoffmann RC, Jia S, Jeurgens LPH, Bill J, Aldinger F, *Mater. Sci. Eng. C* **2006**, *26*, 41-45.

Prior seeding, i.e. application of nucleation sites on the substrate, is frequently used in physical as well as solution-based approaches to obtain films and nanorod arrays. Seeding can significantly change the crystallographic orientation through epitaxial growth or geometrical selection, and thus the density of the film or nanorod array as well.[125,130] Furthermore, a seed layer can enhance crystal growth by lowering the activation energy, hence lower levels of supersaturation are necessary for film growth.[130,133] This in turn efficiently separates nucleation from growth, whereby a better uniformity and control of morphology is gained.[130,144] It should be noted that seeding can enable the deposition even under bath conditions which otherwise would not support the growth.[107] Tao and co-workers utilized radio-frequency magnetron sputtering for seed layer deposition. Altering the oxygen partial pressure during sputtering and in a post annealing step, they could influence crystallization and alignment of subsequently grown nanorods. Using a standard lithographic technique, they were furthermore able to grow ZnO in certain pattern (see Figure 23).[145]
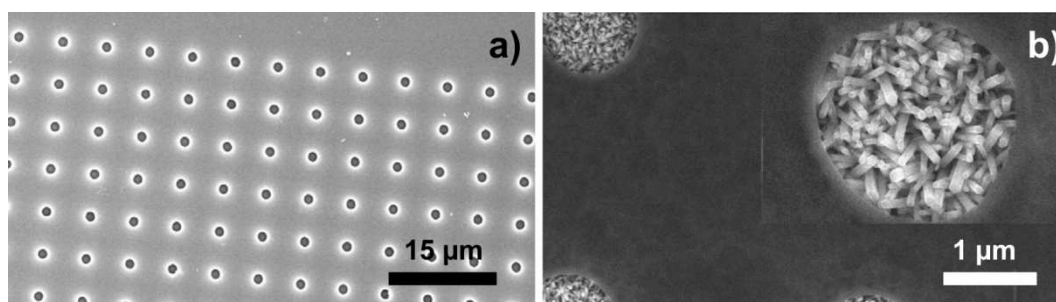

Fig. 23 SEM micrographs of a) patterned seed layer and b) nanorod arrays grown on patterned seed layer (inset shows higher magnification).[145]

The crystallinity of the seed layer strongly influences CBD growth. Greene and co-workers developed a general seeding route based on the thermal decomposition of zinc acetate to ZnO on the substrate at elevated temperatures. This so-called "acetate seed" generates highly *c* axis-textured ZnO seeds, on which epitaxial growth leads to well-aligned ZnO nanorods. Furthermore, these authors investigated different annealing temperatures for the "acetate seed" and found the critical temperature to be higher than 200 °C. Temperatures below 200 °C significantly impair nanorod alignment, i.e. the nanorods became randomly orientated.[146] In addition, smaller seeds resulted in smaller diameters of nanorods.[125] The effect of magnetron sputtered ZnO and ZnO:Ag seeds were studied by Lee and co-workers.[123]

144) Sugunan A, Warad HC, Boman M, Dutta J, *J. Sol-Gel Sci. Technol.* **2006**, *39*, 49-56.
145) Tao Y, Fu M, Zhao A, He D, Wang Y, *J. Alloys Compd.* **2010**, *489*, 99-103.
146) Greene LE, Law M, Tan DH, Montano M, Goldberger J, Somorjai G, Yang P, *Nano Lett.* **2005**, *5*, 1231-1236.

SEM micrographs exhibited that nanorod alignment and density on the substrate can be improved using ZnO seeds, due to higher seed crystallinity compared to the ZnO:Ag seeds.[123] The efficiency of seeding was impressively demonstrated by Wang and co-workers, who were able to grow ZnO nanorods even on cotton fibers (see Figure 24).[133]
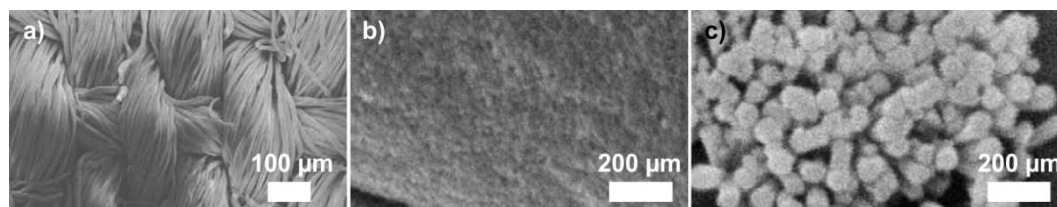

Fig. 24 SEM micrographs of a) untreated cotton fibers, b) seeded fibers, and c) ZnO grown on seeded fibers.[133]

Instead of crystalline seeds, Hoffmann and co-workers used self-assembled monolayers (SAMs) on silicon to direct the growth of ZnO.[143] Another attempt is heteroepitaxial growth on substrates displaying particular crystal faces. For instance, Mu and co-workers utilized Si(001) which led to a tilted growth of ZnO nanospears. This tilt relative to the substrate was attributed to a reduction of lattice mismatch.[147]

Solution pH
The film morphology is strongly governed by the degree of supersaturation of the zinc species in solution, which in turn depends on the pH. Consequently, varying the pH value allows to control film deposition.[130] Yan and co-workers analyzed the influence of the pH on the density of ZnO nanorod arrays grown on seeded substrate. They found less dense arrays to be grown at low pH values, which they argue was due to partial ZnO seed dissolution, consequently leading to less spots for epitaxial growth (see Figure 25).[148]

---

147) Mu G, Gudavarthy V, Kulp EA, Switzer JA, *Chem. Mater.* **2009**, *21*, 3960-3964.
148) Yan X, Li Z, Chen R, Gao W, *Cryst. Growth Des.* **2008**, *8*, 2406-2410.
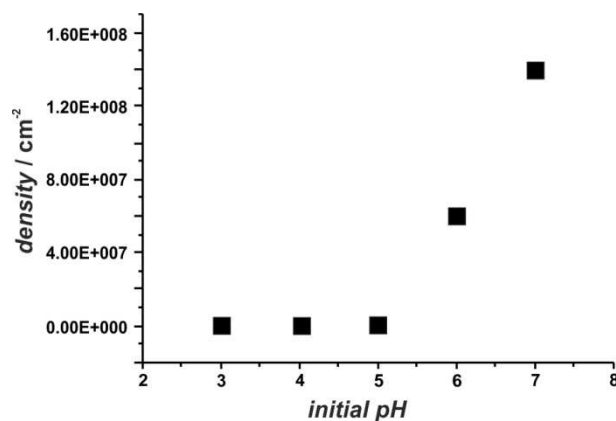
Fig. 25 Plot of nanorod density as function of initial bath pH (adopted from [148]).

Also in an HMTA-zinc nitrate system on seeded substrate, Chu and co-workers found that array density and nanorod diameter strongly depended on the solution pH.[137] However, it should be noted that the authors used acetic acid to adjust the pH value, thus influences of the counter ion cannot be excluded.

Solvent

The influence of the solvent composition on the film morphology was investigated by Wang and co-workers. They compared ZnO films grown in various mixtures of water with ethanol, methanol, and 2-propanol. With increasing alcohol content, the *c* axis growth of ZnO on the substrate was gradually suppressed and the crystallite orientation became increasingly tilted (see Figure 26).[129] This resulted in more intergrown ZnO film instead of nanorod arrays obtained in water solely. The authors presumed either selective adsorption of alcohol on distinct crystal planes or solvent-surface effects to cause suppression of *c* axis growth.[129] The influence of the addition of ethanol was also investigated by Seo and co-workers in a HMTA-zinc acetate system on seeded substrate.[149] They obtained slightly tilted hexagonal rods in CBD systems using water as the only solvent. In contrast, addition of a certain amount of ethanol led to a so-called "shell-like" morphology with rounded corners.[149]

149) Seo S-W, Lee D-H, Kim YS, Chae H, Cho SM, *Phys. Status Solidi A* **2010**, *207*, 724-729.
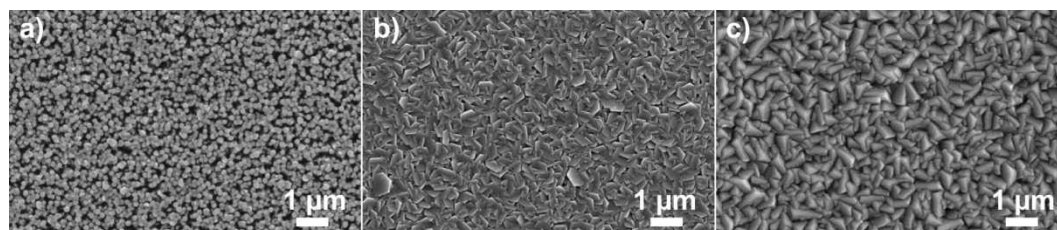
Fig. 26 SEM micrographs of ZnO films grown with different solvent composition. Increasing ethanol content from a) 0%, b) 25% to c) 50%.[129]

Precursor Concentration and Ionic Strength

Zinc precursor and complexing agent concentrations in CBD are typically below 0.1 mol/L but also much higher concentrations have been reported. The precursor concentration directly influences the degree of supersaturation and thus the CBD growth as discussed above. In general, the growth rate is dictated by the degree of supersaturation and consequently, by the precursor concentrations as well. Higher supersaturation leads to higher growth rates but ultimately to thinner films, this effect is the other way around at lower degrees of supersaturation.[107] It should be noted that the CBD process suffers from a lack of efficiency, i.e. approximately only 2% of the starting material is deposited on the substrate, whereas the rest remains in solution, is deposited on the reaction vessel, or precipitates in bulk solution.[127] The influence of the ionic strength appears to be complex, i.e. an increase of the ionic strength decreases the activity of the ions in solution and thus the solubility of the solid phase e.g. ZnO is increased.[140] Govender and co-workers investigated the influence of the addition of KCl on the CBD and found the diameter of ZnO nanorods to be decreased. When KCl concentration was above 0.2 mol/L no deposition occurred at all.[140]

Growth Time

To our knowledge, there is no detailed study on the time dependency of the deposition rate. However, Greene and co-workers measured in an electron microscopy study the nanorod diameters and lengths in dependence of the bath immersion time (see Figure 27).[150] It can be seen in Figure 27 that the diameter,as well as the length roughly increase linearly with reaction time and that there is no evidence of a decrease of deposition rate. This finding is also supported by gravimetric measurements of the CBD by Gurav and co-workers.[151]
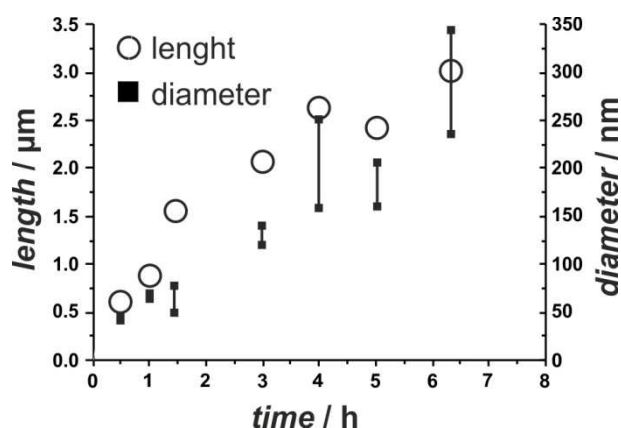

Fig. 27 Plot of nanorod length and diameter as a function of growth time (adopted from [150]).

Bath temperature

Chu and co-workers investigated the influence of the CBD bath temperature in the range of 60 to 90 °C and found that nanorod diameters slightly decrease with increasing temperature. This effect was attributed by the authors to faster nucleation rates at elevated temperatures.[137] Again, Sugunan and co-workers only found negligible influences of the temperature on the CBD process.[144]

150) Greene LE, Law M, Goldberger J, Kim F, Johnson JC, Zhang Y, Saykally RJ, Yang P, *Angew. Chem. Int. Ed.* **2003**, *42*, 3031-3034.
151) Gurav KV, Patil UM, Pawar SM, Kim JH, Lokhande CD, *J. Alloys Compd.* **2011**, *509*, 7723-7728.

Doped ZnO Films via CBD

Doping of ZnO films has been frequently reported for films grown with vapor phase methods. However, there are only few reports on successful doping of ZnO films and nanorod arrays via CBD (see Table 4). The purpose of doping can vary widely as doping can result in enhanced photocatalytic[152] and conductivity properties,[139,153] ferromagnetic behavior,[155] and photoluminescence[131] for instance. In aqueous systems, the major problem of doping is that the metal ion dopants can form stable complexes, which prevent their incorporation in the films.[125] Moreover, the dopant ions can form insoluble particles or gels under the given synthesis conditions.

Table 4: Doped ZnO films grown via chemical bath deposition.

dopant	CBD system	film morphology	features	ref.
Al	nitrate, diethylentriamine	nanorods	conductivity	[153]
I	nitrate, ethanolamine	flowerlike	photocatalytic	[152]
Ti	acetate, HMTA	-	conductivity	[139]
B	nitrate, DMAB	-	conductivity	[155]
Al	sulphate, ethylenediamine	nanorods	luminescence	[131]
Al	nitrate, HMTA	nanorods	-	[138]
Ni	nitrate, NaOH	nanorods	-	[156]
K	acetate, NaOH	nanorods, collums	conductivity	[157]
Al	nitrate, HMTA	nanorods and -sheets	morphology	[158]
Mn	nitrate, HMTA	nanorods	luminescence	[159]
Mn	nitrate, DMAB	collums	magnetic, conductivity	[154]

152) Barka-Bouaifel F, Sieber B, Bezzi N, Benner J, Roussel P, Boussekey L, Szunerits S, Boukherroub R, *J. Mater. Chem.* **2011**, *21*, 10982-10989.
153) Hsu C-H, Chen D-H, *Nanotechnol.* **2010**, *21*, 285603.
154) Fang JS, Luo WH, Hsu CH, Yang JC, Tsai TK, *J. Electron. Mater.* **2012**, *41*, 122-129.
155) Izaki M, Katayama J, *J. Electrochem. Soc.* **2000**, *147*, 210-213.
156) Gayen RN, Rajaram A, Bhar R, Pal AK, *Thin Solid Films* **2010**, *518*, 1627-1636.
157) Tay CB, Chua SJ, Loh KP, *J. Phys. Chem. C.* **2010**, *114*, 9981-9987.
158) Chandramohan R, Vijayan TA, Arumugam S, Ramalingam HB, Dhanasekaran V, Sundaram K, Mahalingam T, *Mater. Sci. Eng. B* **2011**, *176*, 152-156.
159) Lang J, Han Q, Li C, Yang J, Li X, Yang L, Wang D, Zhai H, Gao M, Zhang Y, Liu X, Wei M, *Appl. Surf. Sci.* **2010**, *256*, 3365-3368.

Influence of Additives on the Morphology of CBD Grown ZnO

Additives such as polymers and organic molecules are frequently used to alter crystal growth and morphology.[160-165] In general, adsorption of the additive on specific crystal faces promotes or inhibits the respective growth rates and thus determines the final morphology. This is important since different morphologies significantly influence the material/film properties.[6,137] However, the use of additives is only rarely reported for ZnO films via CBD. Tian and co-workers were the first ones to report an additive-mediated CBD for the preparation of ZnO films. By addition of citrate to the bath solution, they were able to control the aspect ratio of ZnO nanorods, i.e. increasing amounts of citrate suppressed the *c* axis growth (see Figure 28). The authors attributed this to growth inhibiting effects of adsorbed citrate on the (001) faces. By different amounts of citrate during a first, second, and third bath immersion, they produced a variety of nanostructures, which displayed superior photocatalytic activities.[166]
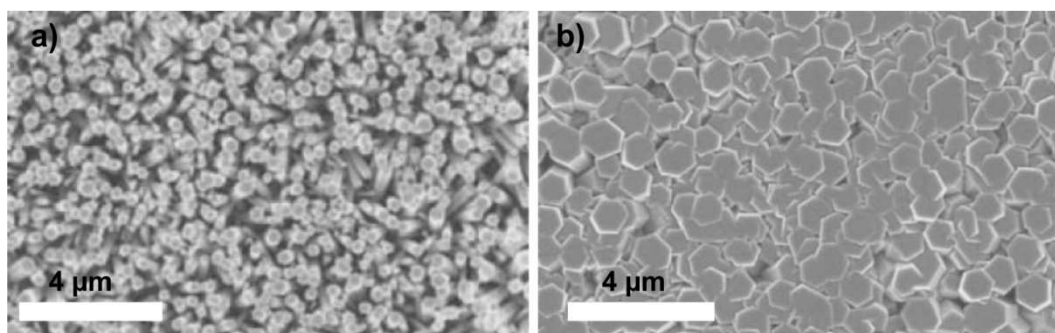

Fig. 28 SEM micrographs of nanorod arrays grown a) without an additive and b) after an additional growth process with addition of citrate (adopted from [166]).

Greene and co-workers could drastically increase the aspect ratio of CBD grown ZnO nanorods from 30 to over 125 by the addition of poly(ethylenimine) (PEI).[125] Hoffmann and co-workers used polyvinylpyrolidone (PVP) and yielded a granular film morphology caused by preferential growth of ZnO in crystallographic [002] and [100] directions.[143]

160) Raula M, Rashid H, Paira TK, Dinda E, Mandal TK, *Langmuir* **2010**, *26*, 8769-8782.
161) Yao KX, Sinclair R, Zeng HC, *J. Phys. Chem. C* **2007**, *111*, 2032-2039.
162) Liang J, Bai S, Zhang Y, Li M, Yu W, Qian Y, *J. Phys. Chem. C* **2007**, *111*, 1113-1118.
163) Cho S, Jung S-H, Lee K-H, *J. Phys. Chem. C* **2008**, *112*, 12769-12776.
164) Yin J, Lu Q, Yu Z, Wang J, Pang H, Gao F, *Cryst. Growth Des.* **2010**, *10*, 40-43.
165) Taubert A, Palms D, Weiss Özlem, Piccini M-T, Batchelder DN, *Chem. Mater.* **2002**, *14*, 2594-2601.
166) Tian Z, Voigt JA, Liu J, McKenzie B, McDermott MJ, Rodriguez MA, Konishi H, Xu H, *Nat. Mater.* **2003**, *2*, 521-526.

The same group investigated the influence of varying ratios of amino acids and dipeptides on the CBD. They obtained different morphologies such as films, spheres, sponges, nets, sheets, cubes, and ribbons, as well as different crystal phases (ZnO and a layered basic zinc salt with incorporated additive). According to the authors, these morphologies stem from different complexation behaviors of the used additives.[167] The same group also produced uniform porous films on silicon functionalized with self-assembled monolayers (SAMs) by addition of PVP. The addition of PVP inhibited further growth of the ZnO crystallites in solution which then attached in an oriented fashion to the negatively charged substrate surface. This resulted in c axis-textured nanocrystalline films with grain sizes of 6 to 9 nm (see Figure 29).[168]
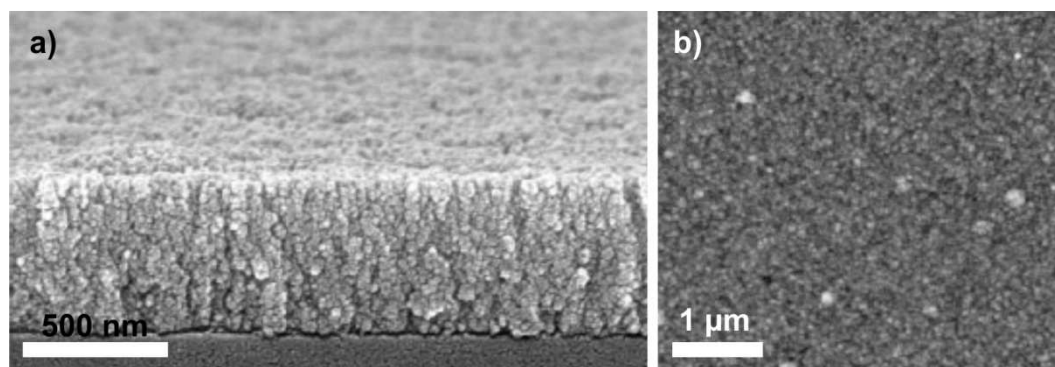

Fig. 29 SEM micrographs of a) and atomic force microscope image b) of ZnO film deposited from solution containing PVP (adopted from [168]).

PVP as an additive in CBD was also used by Wei and co-workers. They found that an increasing content of PVP led to smaller ZnO nanorod diameters, an effect which they attributed to the adsorption of PVP on the columnar facets, and a decrease in the nanorod density probably caused by an increasing viscosity and thus restricted diffusion and growth.[169] Zhang and co-workers performed secondary additive-mediated CBD on orientated ZnO nanorods substrates. Secondary CBD with diaminopropane as additive induced the growth of branches on the columnar facets of the nanorods. In contrast, addition of citrate induced the growth of nanoplates on the columnar facets. Furthermore, they performed a tertiary growth with citrate addition on diaminopropane induced structures and *vice versa* (see Figure 30).[170]

167) Gerstel P, Lipowsky P, Durupthy O, Hoffmann RC, Bellina P, Bill J, Aldinger F, *J. Ceram. Soc. Jpn.* **2006**, *114*, 911-917.
168) Lipowsky P, Hoffmann RC, Welzel U, Bill A, Aldinger F, *Adv. Funct. Mater.* **2007**, *17*, 2151-2159.
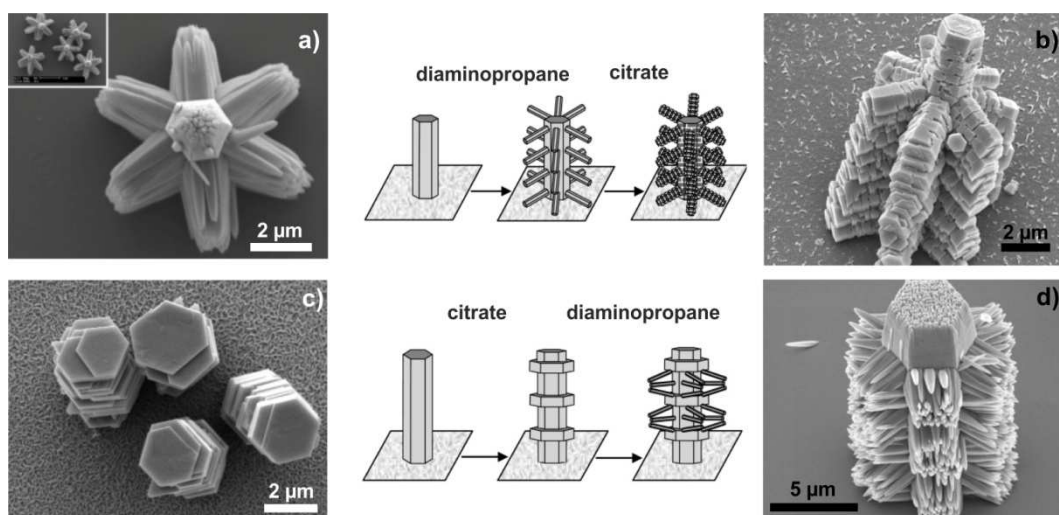
Fig. 30 SEM micrographs of ZnO nanostructures grown on nanorods in baths containing a) diaminopropane and c) citrate, and after a subsequent growth with b) citrate on nanostructures obtained with diaminopropane and d) with diaminopropane on nanostructures obtained with citrate. Scheme in the center illustrates the growth sequence (adopted from [170]).

Polyvinyl alcohol (PVA) was used by Zhu and co-workers to induce a centripetal growth of ZnO nanorods leading to top-assembled structures.[171] Liu and co-workers employed gelatin in CBD and yielded an array of ZnO microplatelets which were orientated in an unusual fashion, i.e. with their *c* axes parallel to the substrate.[172]

171) Zhu D, He Q, Chen Q, Fu Y, He C, Shi L, Meng X, Deng C, Cao H, Cheng, J, *Nano* **2011**, *5*, 4293-4299.
172) Liu X, Afzaal M, Badcock T, Dawson P, O'Brien P, *Mater. Chem. Phys.* **2011**, *127*, 174-178.

3 Magnesium Fluoride Suspensions for Corrosion Protection

3.1 Preface

This chapter contains a published article dealing with the corrosion prevention of magnesium welding joints by a novel hybrid tool employing suspensions of nanocrystalline MgF_2. The motivation for this study was the lack of a process for welding magnesium parts avoiding the risk of an increase of the corrosion susceptibility at the joints as a result of the processing. To overcome the corrosion problem at the material joints, a hybrid tool consisting of a TIG torch and a SPS was developed which allows joining and coating in one process step. The work described here and which is presented in the article was performed within the project "*Innovative Methods for Manufacturing of Multifunctional Surfaces*" financed by the Volkswagen foundation. The work can be divided in two parts: The design and construction of the hybrid tool, and the preparation of suitable suspensions for the SPS. Whereas Mark A. Swider was responsible for the first part, I conducted all experiments regarding the MgF_2 suspension development and preparation. For MgF_2 preparation I could use experiences in polyol-mediated syntheses of nanocrystalline CeF_3:Eu. This work was published with Dr. Falk Heinroth as first author.[173,174] For the work presented here, all syntheses of MgF_2 as well as suspension formulation were performed by myself. I also characterized the products by means of PXRD, DLS, EDX, SEM, UVVis spectroscopy, zeta potential determination, and viscosity measurements. The first version of the manuscript was written by me and I also integrated complementary sections and corrections from the co-authors. Results from following other techniques were obtained by the co-authors: Fluorescence spectroscopy – Dr. Matthias Adlung, Prof. Dr. Claudia Wickleder group; TEM and cross-section preparation for SEM – Priv.-Doz. Dr. Armin Feldhoff; corrosion tests – Mark A. Swider and Petra Hoyer; SPS – Martin Erne and Dr. Kai Möhwald.

173) Heinroth F, Waltz F, Wiebke M, Behrens P, *Z. Anorg. Allg. Chem.* **2008**, *634*, 2045.
174) Heinroth F, Gruss D, Müller S, Waltz F, Martynczuk J, Feldhoff A, Behrens P, Wiebcke M, *J. Mater. Sci.* **2010**, *45*, 1595.

The results of the work on MgF_2 nanoparticles were also presented orally at the DGM Magnesium conference 2009 in Weimar, on the Nanoday 2010 in Hannover and on the 2nd Symposium on Functional Surfaces 2011 in Aachen.[175-177] In association with the Weimar conference, we have also produced and published an invited book contribution.[178] Also upon invitation, the researchers from the Leibniz University Hannover have authored a more popular version in the Unimagazin.[179]

175) Hassel T, Swider MA, Waltz F, Möhwald K, Bach F-W, *Talk on the 8th International Conference on Magnesium Alloys and their Application*, Oct. 25-28, **2009** Weimar.
176) Waltz F, Swider MA, Hoyer P, Hassel T, Erne M, Möhwald K, Feldhoff A, Adlung M, Wickleder C, Bach F-W, Behrens P, *Talk on the Nanoday*, Sept. 30, **2010**, Hannover.
177) Swider MA, Waltz F, Hoyer P, Hassel T, Erne M, Möhwald K, Behrens P, Bach F-W, *Talk on the 2nd International Conference on Functional Surfaces*, Sept. 14-15, **2011**, Aachen
178) Magnesium: 8th International Conference on Magnesium Alloys and their Application, Hassel T, Swider MA, Waltz F, Möhwald K, Bach F-W, Behrens P, Wiley VCH **2009**, 872-878, ISBN-10:3527327320.
179) Bach F-W, Behrens P, Waltz F, Swider MA, Hassel T, *Unimagazin Leibniz Universität Hannover*, **2011**, *1/2*, 48-51.

3.2 Publication

Synthesis of highly stable magnesium fluoride suspensions and their application in the corrosion protection of a Magnesium alloy

Florian Waltz, Mark A. Swider, Petra Hoyer, Thomas Hassel, Martin Erne, Kai Möhwald, Matthias Adlung, Armin Feldhoff, Claudia Wickleder, Friedrich-Wilhelm Bach, and Peter Behrens

4 Zinc Oxide Self-Assembled Superstructures

4.1 Preface

This chapter contains an article dealing with the influences of polysaccharides on the morphology of ZnO precipitates. Motivated by the search for alternatives to well-established but expensive physical application methods for transparent conductive films, ZnO was found to be well-suited as it can be deposited as a thin film via simple approaches based on aqueous solutions. In addition, aqueous solutions allow the application of additives which can have a huge impact on crystal morphology and thus on the crystal and film properties as well. Therefore, we employed natural polysaccharides (PSs) in ZnO precipitation experiments to investigate their influence on ZnO crystal morphology. Already in previous biomimetic experiments, in which PSs were employed in precipitation experiments of silica, these polysaccharides had indicated strong morphology-directing properties. This previous study had been accomplished by Dr. Britta Hering in her diploma thesis, and I had worked on this project within my focus practical course supervised by her. In the further course of the presented thesis, the results and expertises gained within this precipitation study supported the work on ZnO films which is presented in chapter 5.

Basic preparative experiments for the precipitation study were performed by Gesa Wißmann and Jann Lippke during their focus practical courses under my supervision. Major analytical investigations as PXRD and SEM, additional precipitation and staining experiments were executed by me. I have also written the first version of the manuscript, performed the corrections and guided the paper to a large part through the publishing. Priv.-Doz. Dr. Stefanie Eiden and Dr. Andreas M. Schneider have provided valuable suggestions and advice. The other co-authors have contributed with their respective expertises as follows: TEM investigations – Frank Steinbach and Priv.-Doz. Dr. Armin Feldhoff; confocal microscopy – Hans-Christoph Schwarz; DLS Jann Lippke and Britta Hering. Results regarding this work were also presented as a poster on the Nanoday 2011.[180]

---

180) Waltz F, Schwarz H-C, Wißmann G, Lippke J, Schneider AM, Behrens P, Nanoday, Sept. 29, **2011**, Hannover.

4.2 Publication

Evolution of the Morphologies of Zinc Oxide Mesocrystals Under the Influence of Natural Polysaccharides

Florian Waltz, Gesa Wißmann, Jann Lippke, Andreas M. Schneider, Hans-Christoph Schwarz, Stefanie Eiden, and Peter Behrens

The final article is available online at
http://pubs.acs.org/doi/abs/10.1021/cg3002674

Supporting information available in the Appendix (chapter 8) and online at
http://pubs.acs.org/doi/suppl/10.1021/cg3002674

CRYSTAL GROWTH & DESIGN

Evolution of the Morphologies of Zinc Oxide Mesocrystals Under the Influence of Natural Polysaccharides

Florian Waltz,[†,§] Gesa Wißmann,[†,§] Jann Lippke,[†,§] Andreas M. Schneider,[†,§] Hans-Christoph Schwarz,[†,§] Armin Feldhoff,[‡,§] Stefanie Eiden,[#] and Peter Behrens*[,†,§]

[†]Leibniz Universität Hannover, Institut für Anorganische Chemie, Callinstrasse 9, 30167 Hannover, Germany
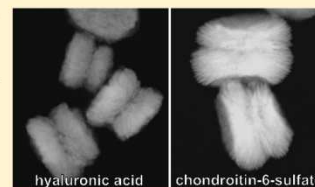[‡]Leibniz Universität Hannover, Institut für Physikalische Chemie und Elektrochemie, Callinstasse 3A, 30167 Hannover, Germany
[§]Leibniz Universität Hannover, ZFM-Center for Solid-State Chemistry and New Materials, Hannover, Germany
[#]Bayer Technology Services GmbH, 51368 Leverkusen, Germany

S *Supporting Information*

ABSTRACT: In the present investigation, we have analyzed the influence of naturally occurring negatively charged polysaccharides on the morphology of zinc oxide obtained in low-temperature precipitation experiments. Performing detailed analyses of scanning electron microscopy (SEM) micrographs, we inferred the morphology of individual nanocrystals as well as the construction of their aggregates. X-ray and electron diffraction were used to identify directions of preferred growth. Whereas addition of hyaluronic acid (HYA) to the synthesis batch resulted in a rod-like morphology of the primary crystallites, addition of chondroitin-6-sulfate (C6S) leads to platelet-like crystallites. Despite their different shapes, the respective subunits aggregated in similar ways, with perfect orientation with regard to their $a-b$ planes, thus leading to symmetrical superstructures. Further growth proceeded, via different mechanisms, that is, subunit growth or further aggregation of subunits, dependent on whether the precipitation was performed in the presence of HYA or C6S. These details were elucidated by testing different concentrations and reaction times. The formation of the morphological characteristics could be attributed to subtle differences in the nature of the two polysaccharides. Understanding how to direct the formation of mesocrystal morphologies is important for enhancing material properties, especially for highly demanding applications of zinc oxide, such as semiconducting films.

■ INTRODUCTION

Zinc oxide (zincite, ZnO) is a material showing a diverse range of morphologies. Its uniaxial hexagonal crystal system allows for the formation of platelet-like, isometric, or column-shaped crystals. Such differently shaped crystallites can attain a variety of morphologically different aggregation forms: Spherical, star- and flower-like to doughnut-shaped aggregates have been reported.[1−10] Furthermore, zinc oxide is an industrially important material, used in a variety of applications, for example, as piezoelectric transducer and actuator, chemical sensor, phosphor, and photocatalyst.[6,11−16] Current interest focuses on its promising properties as a wide band gap semiconductor which can be employed for diverse electronic applications. Doped with boron or aluminum, zinc oxide may be used in transparent conducting layers for, for example, solar cells and thin film-based displays. Especially for the latter applications, controlling size and morphology of the crystallites is an important tool for tailoring material properties.

Different wet chemical methods have been applied for the synthesis of zinc oxide on substrates, for example, sol−gel and chemical bath deposition (CBD) methods.[17−21] In recent years, many researchers have focused on CBD methods due to the high reproducibility and comparably moderate effort. Furthermore, CBD methods are usually performed at temperatures below 100 °C and are thus very energy efficient. Also, sensitive

organic or biological molecules can be added in order to influence the deposition process. In the CBD of zincite, hexamethylenetetramine (HMTA) is often used. It is assumed that HMTA acts as a slow and continuous source of hydroxide ions, keeping the ZnO crystallization under thermodynamic control.[22]

Because of the polar character of ZnO crystallites, charged molecules can easily attach electrostatically to the charged crystallite faces, especially to the oppositely charged basal planes. Thus, the presence of such molecules can either promote or inhibit further growth of different faces. Mediating growth of ZnO by the use of such additives is very promising in order to obtain various morphologies of nanostructured ZnO aggregates under mild conditions and has consequently been reported previously by a number of groups. A large variety of ZnO aggregate structures has been obtained with additives such as ethylene diamine and citrate,[23] ascorbate,[24] poly(ethylene glycol),[25] cetyltrimethylammonium bromide (CTAB),[26] citrate, and diaminopropane,[27] Tween-85,[28] malate,[29] poly(sodium 4-styrenesulfonate),[30] poly(ethylene oxide-*block*-methacrylic acid) and poly(ethylene oxide-*block*-styrene sulfonic acid)

diblock copolymers,[31] and poly(styrene-acrylic acid).[32] A special case is the use of naturally occurring additives, for example, amino acids, peptides,[1,33,34] or gelatin.[35] Very recently, peanut-like ZnO structures have been obtained through a hydrothermal approach in the presence of pectin, a naturally occurring polysaccharide.[36] When biopolymers such as gelatin or pectin are employed, the deposition processes might in certain aspects resemble biomineralization processes.[37] However, although there has been some effort to investigate the formation mechanisms, information on how crystallite and aggregate morphologies are formed is still scarce. It has been proposed that aggregate formation might be driven by a templating effect of the polymer[26,36] or an electrical-field-driven arrangement of the subunits.[30]

Here we present the results of precipitation experiments of ZnO under the influence of two different naturally occurring and thus environmentally friendly biopolymers, namely, hyaluronic acid (HYA) and chondroitin-6-sulfate (C6S) (see Figure 1). Both are polysaccharides (PSs) with a rather similar chemical structure, making comparisons of their influences on ZnO deposition especially interesting.
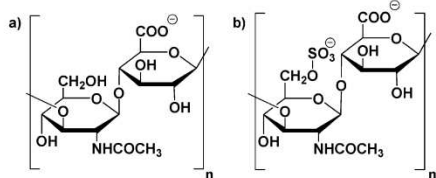

Figure 1. Structures of the polysaccharides (PSs) used as additives in this work: (a) hyaluronic acid (HYA), (b) chondroitin-6-sulfate (C6S).

Both PSs consist of linked alternating units of β-D-glucopyranuroic and β-D-N-acetylgalactosamine, of which the latter ones are sulfated in the case of C6S. Depending on the polysaccharide and its concentration, we have prepared zincite composite structures with different habiti of the primary zincite crystallites and with different aggregate morphologies, as observed by scanning electron microscopy (SEM) and deduced from powder X-ray diffraction (PXRD) and electron diffraction (ED) patterns. Combining these observations with the results from additional physicochemical characterization methods allows us to propose mechanisms for the generation of the different morphologies by the two PSs.

■ EXPERIMENTAL SECTION

Precipitation. All chemicals were used without further purification, and micropore filtered water (water was filtered with a Clear UV, SG Wasseraufbereitung und Regenerierungsstation GmbH Hamburg, to a conductivity of 0.055 μS/cm) was used in all experiments. The experiments were carried out with zinc nitrate hexahydrate (Aldrich) and hexamethylenetetramine (HMTA, Aldrich) in a fixed molar ratio of 1:1 to examine the influence of the polysaccharides only. Hyaluronic acid (HYA, Aldrich, sodium salt from *Streptococcus equi*, ~1600 kDa) and chondroitin-6-sulfate (C6S, Gerbu Biochemicals GmbH, sodium salt from shark cartilage, ~20 kDa) were used as polysaccharides with varying molar ratios calculated on the basis of the sodium salts of the repeating units (see Figure 1a,b above). For precipitation experiments, 10 mL of a zinc nitrate solution (25 mM) at room temperature was added rapidly to 40 mL of a solution of HMTA and a polysaccharide which had been preheated to 85 °C for ca. 5 min. The combined solutions were stirred at 85 °C in a screw-cap bottle for 300 min.

However, in order to investigate the formation mechanism in further detail, in some batches, samples were taken from the reaction mixture after 15, 30, 60, 180, and 1440 min. The whitish precipitates were isolated by centrifugation at 18000g with a benchtop centrifuge Multifuge X3 from Thermo Fisher Scientific Inc. (Waltham, USA). For purification, the precipitate was redispersed in water, centrifuged again, and dried at 60 °C overnight.

Characterization. Powder X-ray diffraction (PXRD) patterns were recorded on a STOE StadiP diffractometer (Darmstadt, Germany) with Ge(111)-monochromatized Cu Kα radiation in transmission mode. The diffraction patterns were measured with a step width of 0.1° and 25 s on each step in a 2θ range of 20−60°. All presented diffraction patterns were normalized regarding intensity. The full width at half-maximum (fwhm) of the peaks was used to calculate the crystallite sizes according to the Scherrer's equation with a value of 0.9 for the shape factor K. In order to eliminate instrumental peak broadening, a silicon standard was used. SEM micrographs were taken on a JEOL JSM-6700F FE-SEM (Tokyo, Japan) with an acceleration voltage of 2 kV and a working distance of 3 mm. A JEM-2100F-UHR field-emitting transmission electron microscope from JEOL (Tokyo, Japan) equipped with a 1k-CCD camera. An accelerating voltage of 200 kV was used for FE-TEM and selected area electron diffraction (SAED) investigations. For electron microscopy analyses, the solid material was dispersed in ethanol and spotted on a carbon-block or a carbon-supported copper-grid. Measurements of zeta-potentials with varying pH values were performed using a Zetasizer Nano from Malvern Instruments Ltd. (Worcestershire, UK) equipped with an MPT-2 autotitrator. The surface area of selected materials was determined via N$_2$ physisorption measurements at 77 K with an Autosorb 3 from Quantachrome GmbH & Co. KG (Odelzhausen, Germany). Thermogravimetric analyses were carried out with a Simultaneous Thermal Aanalyzer 429 from Netzsch (Selb, Germany) with a heating rate of 5 °C/min up to 1000 °C in air.

■ RESULTS AND DISCUSSION

Influence of Polysaccharides on ZnO Precipitation. Zincite crystals, with a wurtzite structure (hexagonal, space group $P6_3mc$), are polar along the c axis and feature a positively charged (001) face, terminated by Zn^{2+} ions, and a negatively charged (00$\bar{1}$) face, terminated by oxide ions. In this study, we employed the naturally occurring polysaccharides (PSs), hyaluronic acid (HYA), and chondroitin-6-sulfate (C6S). The structures of these polymers are shown in Figure 1. Both PSs were used as sodium salts. The carboxylic acid groups of the glucopyranoic acid residues and also the sulfate group of the acetylgalactosamine residue in C6S will to a large part be deprotonated over wide ranges of the pH value so that these polymers feature strongly negative zeta-potentials (see Figure S1 in the Supporting Information). In the pH range of the synthesis, the zeta potential is ca. −30 mV for HYA and ca. −50 mV for C6S. Thus, strong interactions of the PSs with the (001) faces of zincite crystals are expected; that is, the negatively charged polymers will probably adsorb mainly onto the (001) face and thus influence the growth in c direction; however, adsorption to other faces, that is, prism faces, cannot be excluded.

Under the synthesis conditions described in the Experimental Section, HMTA slowly decomposes and continuously delivers hydroxide ions, which are necessary for the formation of the zincite phase.[22] A pure zincite phase is confirmed for all precipitates obtained after a 300 min reaction time, irrespective of the addition of a PS (Figure 2). It is interesting to note that whereas the pattern of HYA-ZnO appears in all respects similar to the diffraction pattern of pure zincite (prepared in the absence of PSs, blank sample), the C6S-ZnO sample exhibits a
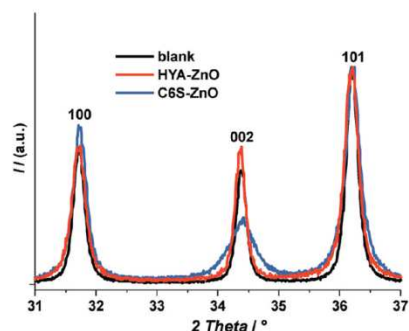
Figure 2. PXRD patterns of zincite prepared in the absence of additives (blank) and of zincite precipitated in the presence of C6S or HYA. The PS:Zn ratio was (1/8):1 and the reaction time was 300 min.

strong broadening of the (002) reflection, indicating a diminished size along the c axis of the zincite crystals.

Morphology of ZnO Aggregates. Electron microscopy investigations of the precipitates which were collected after 300 min are displayed in Figure 3. In the absence of a PS (blank
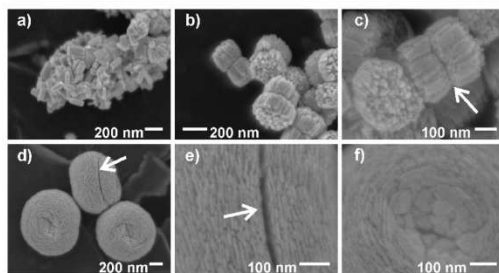

Figure 3. SEM images of ZnO samples collected after 300 min: (a) pure zincite (blank sample); (b) HYA-ZnO (1/8):1; (c) HYA-ZnO (1/8):1 in higher magnification; (d) C6S-ZnO (1/2):1; (e, f) higher magnifications of C6S-ZnO (1/2):1. The arrows in c, d, and e mark the equatorial constrictions of the PS-ZnO superstructures.

sample), hexagonal rod-shaped crystals of approximately 100 nm length were formed (Figure 3a). This morphology is in agreement with the reported growth rates of zincite faces: $[\bar{1}00] > [\bar{1}01] > [001] \approx [00\bar{1}]$.[38] When a certain amount of PS is present during the synthesis, a pure zincite phase is still obtained, but the morphology differs significantly from the blank sample. Under the influence of HYA, aggregates of zincite crystals with an "asparagus bundle"-like morphology are formed (Figure 3b). They apparently consist of rod-shaped subunits aligned along their long axis (Figure 3c) with two of such bundles fused together at a central plane. Total aggregate sizes varied between 200−300 nm (Figure 3b). The other PS employed, C6S, led to larger aggregates with sizes around 900 nm. Again, these aggregates consist of two opposite halves, which, however, have a concave bowl-like shape (Figure 3d). At higher magnification (Figure 3e,f), it can be seen that these spherical aggregates are assembled from thin platelets, which are stacked in an orderly fashion, in contrast to the rods observed as primary crystallites in the HYA-ZnO samples.

It is intriguing that both kinds of precipitates, synthesized with HYA or with C6S as organic additives, consist of two halves, one of which is larger than the other. At the borderline between the two halves, there is a pronounced "equatorial" constriction (arrows mark the constrictions in Figure 3c−e). This indicates that the formation of these aggregates does not proceed via the classical ion-attachment mechanism, but by the oriented aggregation of small primary subunits, as proposed by Cölfen and co-workers.[39] Organic polymers are frequently incorporated in such structures during their formation and growth. Indeed, performing thermogravimetric analyses, we found that the precipitates contained approximately 5−8% organic material (see Figure S2 in the Supporting Information).

The presence of equatorial constrictions has already been reported for zincite aggregates precipitated in the presence of other polymers.[2,31,40,41] Wang and co-workers found a convex-concave morphology in the polymer-driven precipitation of calcite, very similar in shape to the C6S-ZnO aggregates presented in this study. According to them, such a morphology, which is contradictive to Ostwald ripening, is strong evidence for a long-range dipolar field driven alignment of subunits.[42] Furthermore, restrictions can be caused by twinning of initially formed subunits, followed by dipolar field driven alignment.[30,40] In this case, the aggregates should exhibit either positively or negatively charged surfaces caused by displaying (001) or (00$\bar{1}$) faces, respectively. Liu and co-workers substantiated this finding via electrostatic staining of the aggregates; onto their products, only a positively charged dye was adsorbed selectively.[30] In their work, the particles were much larger and thus easily visible with optical microscopy. For our staining experiments, we used positively or negatively charged latex beads with sizes of about 30−50 nm and investigated their adsorption behavior via SEM. Only the positively charged latex beads adsorbed on the surface of the C6S-ZnO and HYA-ZnO aggregates, which therefore must feature a negative charge on their surface (see Figure S3 in the Supporting Information). In line with the results of Liu and co-workers,[30] we conclude that the aggregates are twinned along the equatorial constriction, probably caused by an initial alignment of (001) to (001) faces (mediated by a negatively charged PS), from which the mesocrystals grow in the (00$\bar{1}$) direction in both parts of the superstructure.

In order to exclude that differences in molecular mass of the two PSs (C6S $\sim$ 20 kDa; HYA $\sim$ 1600 kDa) cause the described differences in morphology, we performed a comparative experiment with low-molecular mass HYA (10−50 kDa). SEM micrographs of the ZnO superstructures obtained with this PS sample display the typical morphology HYA-ZnO which is also observed with high-molecular mass HYA (see Figure S4 in the Supporting Information). Therefore, it can be stated that differences in the HYA and C6S systems are caused by the additional sulfate group of C6S at C6 position.

We have performed experiments with ratios of PS to Zn(II) ranging from (1/128):1 up to 1:1. Even at very low PS:Zn ratios, effects on the growth of ZnO can be observed. These variations in the size and habit of the subunits and in the shape of the aggregate structures were monitored by PXRD and SEM investigations. PXRD patterns were evaluated with regard to the widths of the (100) and the (002) reflections. From the full widths at half-maximum (fwhms) of these reflections, the sizes of the coherently scattering domains in the a and the c directions, D_a and D_c, were calculated using the Scherrer equation (Table 1). We furthermore define the aspect ratio

Table 1. Sizes of Subunits after 300 min Reaction Time as a Function of the Concentration of the Added PS[a]

PS:Zn	HYA			C6S		
	D_a	D_c	AR	D_a	D_c	AR
1:1	74	60	1.23	48	15	3.20
(1/2):1	53	61	0.87	48	15	3.20
(1/4):1	71	90	0.79	49	16	3.06
(1/8):1	50	82	0.61	47	17	2.77
(1/16):1	55	72	0.76	58	24	2.42
(1/24):1	63	117	0.54	51	22	2.32
(1/32):1	63	92	0.69	54	22	2.46
(1/64):1	67	103	0.65	52	28	1.86
(1/128):1	74	99	0.75	72	34	2.12

[a]Crystallite sizes D_a and D_c were deduced from the reflection broadening of the (100) and (002) reflections of zincite using Scherrer's equation. PS:Zn denotes the molar ratio of the PS repeat unit and Zn(II) (with the Zn(II) content fixed to 1).

$AR = D_a/D_c$. AR is used to describe the anisotropy of the shape of the crystalline subunits of the aggregates (i.e., the coherently scattering domains). A high value of AR indicates platelet-like subunits, a low AR indicates a rod-like crystal habitus.

A ZnO sample prepared in the absence of any additive under otherwise identical conditions provides an AR of 0.75. AR values of samples precipitated under the influence of varying amounts of HYA are in the same range with a slight increase of AR at higher HYA concentrations (Table 1 and Figure 4). Consequently, the zincite subunits of the aggregates formed in the presence of HYA show rod-like habiti. This finding is in good agreement with the SEM images (Figures 3b,c and 4).

The change in the aspect ratio can be attributed to a variation of the crystallite size in the c direction: Whereas D_a fluctuates roughly between 50 and 70 nm, a trend of increasing D_c with decreasing HYA content is evident: At high HYA concentrations, D_c is ca. 60 nm, whereas at low HYA contents it is ca. 100 nm. This indicates that only high concentrations of HYA suppress the c axis growth.

In contrast to the relatively small AR values observed in the HYA-ZnO system which vary only slightly with HYA concentration, the samples precipitated with C6S show considerably larger AR values between 1.9 and 3.2. This is caused by a strongly diminished growth along the c axis, resulting in a pronounced platelet-like shape of the subunits. Again, this finding is in good agreement with the SEM images which also showed platelet-like subunits (Figures 3e,f and 4). In the C6S system, the size in the a direction D_a is about 50 nm at
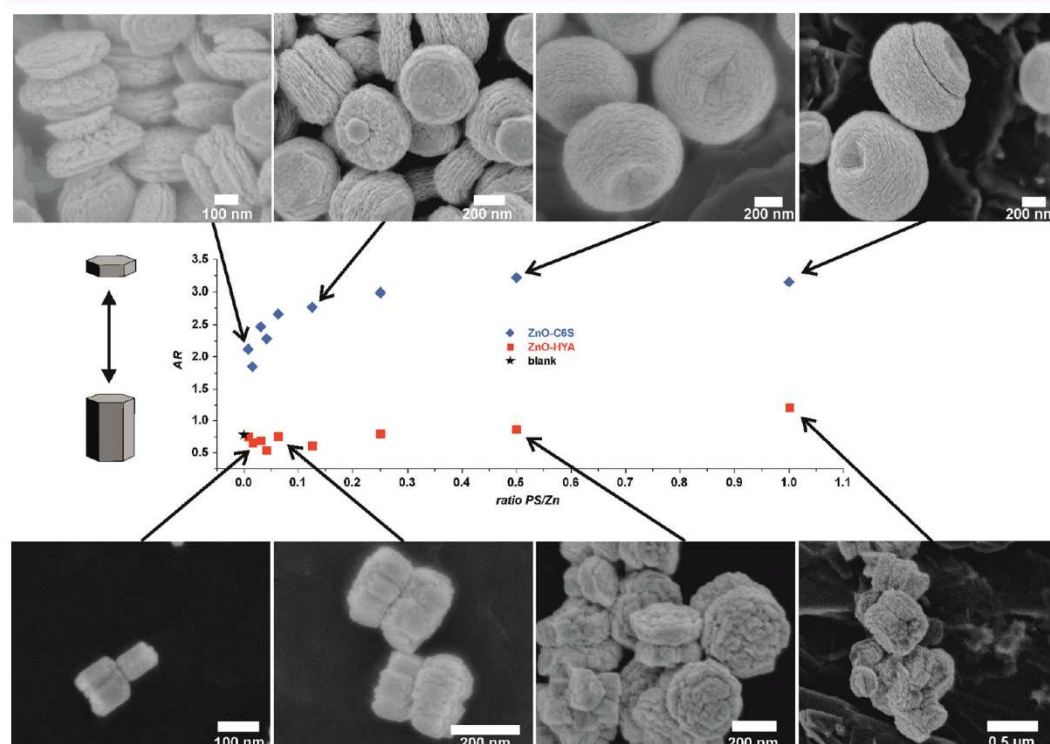

Figure 4. Aspect ratio $AR = D_a/D_c$, calculated from reflection broadening of the (100) and (002) reflections, respectively, as a function of the ratio of PS:Zn, that is, the molar ratio of the PS repeat unit and zinc ions in solution. The inset visualizes that larger values of AR are caused by platelet-like subunits, whereas rod-like subunits lead to small ARs. The asterisk marks the AR value of a blank ZnO sample. The SEM images illustrate the morphologies of some of the precipitates.

most concentrations and increases to 70 nm only at very low C6S content. The depression of the growth in the *c* direction is much stronger than in the *a* direction. With decreasing C6S content, the size of the crystallites along the *c* axis more than doubled from 15 nm at the 1:1 ratio to 34 nm at the (1/128):1 ratio. It is also noteworthy that the influence of C6S on the dimensions and on the aspect ratio is much stronger than that of HYA.

Comparing the SEM images of the products obtained under variation of the concentration of the PS, we found a strong correlation between the morphology of the superstructures and the PS to Zn(II) ratio (Figure 4). The characteristic "asparagus-bundle"-like morphology typically described for the HYA system is present at PS:Zn ratios of 1:1 to (1/32):1. However, at a ratio of 1:1, the superstructures have a less pronounced equatorial constriction and are more cylindrical. Figure 4 and Table 1 already showed that AR slightly increases at high HYA content. This is accompanied by an increase of the size of the HYA-ZnO superstructures. HYA-ZnO superstructures obtained with ratios below (1/32):1 consisted of fewer subunits, and thus the morphology became less well-defined.

Nearly spherical aggregates, consisting of two parts of different sizes, are found in the C6S-ZnO system in the range of PS:Zn from (1/4):1 up to 1:1. At lower C6S contents, both hemispheres of the aggregates are rather open. At very low contents of C6S, this leads to a morphology that corresponds to a sandwich-like double disk.

Surface areas of the products grown with (1/4):1 ratio for 300 min were determined with nitrogen physisorption at 77 K (see Figure S5 in the Supporting Information). BET surface areas for HYA-ZnO and C6S-ZnO samples are in the range of 20 m^2 g^{-1}. Considering the very dense alignment of the subunits, visible in the SEM micrographs, such small surface areas are not surprising and point to a dense stacking of the ZnO crystallites, possibly with polysaccharide molecules present in small gaps between the crystallites.

TEM investigations can provide further insight into the structural morphology of the products (Figure 5). These investigations were performed on samples grown for 180 min

with a PS:Zn of (1/4):1 ratio because of their relatively small size, which was suitable for TEM analyses. Figure 5a,b displays TEM micrographs of HYA-ZnO superstructures in two different orientations: Figure 5a provides a view into the equatorial constriction of the "asparagus-bundle"; Figure 5b gives a view onto the plane defined by that constriction. At the edges of the HYA-ZnO superstructure in Figure 5b, a hexagonal shape is partially visible. With the electron beam perpendicular to the constriction plane of the HYA-ZnO aggregate, the SAED pattern consists of a reflection pattern with hexagonal symmetry, corresponding to the [001] zone axis of zincite (Figure 5c).

The results of the TEM investigations of C6S-ZnO aggregates are shown in Figure 5d,e. As for the HYA-ZnO superstructures, an SAED pattern with the electron beam perpendicular to the equatorial constriction plane reveals the hexagonal symmetry of the [001] zone axis (Figure 5f). For both types of superstructures, the TEM images thus indicate that the zincite crystallites in the aggregates are stacked with their *a*−*b* planes mainly parallel (at least at this growth stage at 180 min). Astonishingly, the sharp (*hk*0) diffraction spots in the SAED patterns revealed that the individual subunits also align their *a* and *b* axes in the *a*−*b* planes. When the oriented stacking is very similar in both types of aggregates, the differences in the appearance of the superstructures can be attributed mainly to the different shapes of the primary crystallites, that is, rod-like crystallites in the HYA-ZnO system and platelet-like ones in the C6S-ZnO system.

The degree of orientational alignment of the subunits in the inner parts of the aggregates can be evaluated from STEM micrographs (see Figure S6 in the Supporting Information). C6S-ZnO aggregates show an increasing angle of inclination from the inside to the outside of the aggregates with regard to the *c* axes of the individual platelets.

Another way to gain a view into the construction of the inner parts of the superstructures of the PS-ZnO aggregates is to grind the powder material obtained in the syntheses. SEM micrographs of such samples show broken aggregates (Figure 6). Figure 6a,b displays HYA-ZnO aggregates which were
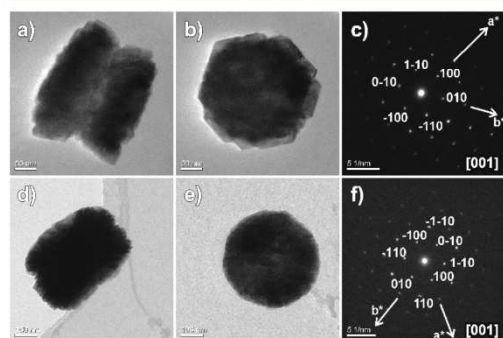

Figure 5. TEM micrographs and SAED patterns of PS-ZnO superstructures prepared with a PS:Zn ratio of (1/4):1 after 180 min reaction time; (a−c) HYA-ZnO structures; (d−f) C6S-ZnO structures. (a, d) View side-on onto the equatorial constriction of the aggregates; (b, e) view onto the plane defined by the equatorial restriction. (c, f) SAED patterns taken with the orientation of the images in (b) and (e), respectively.
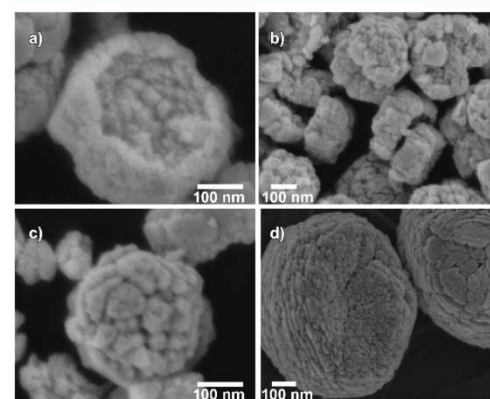

Figure 6. SEM micrographs of PS-ZnO superstructures which had been fractured by grinding. (a−c) HYA-ZnO grown for 300 min with a HYA:Zn ratio of (1/4):1; (d) C6S-ZnO grown for 1440 min with a C6S:Zn ratio of (1/4):1.

cleaved along the equatorial constriction. The larger halves of the aggregates appear to overlap with the smaller ones. Comparing the relatively small size of the subunits inside (Figure 6a) to the size of the crystallites on the outer parts (Figure 6c), one can assume a wedge-shaped morphology for these subunits, tapering toward the inside, even though the hexagonal shape is only rudimentarily visible (Figure 6c). An image of an equatorially disrupted C6S-ZnO aggregate (shown in Figure 6d next to an undestroyed one) also revealed an increase in the size of the platelet-like zincite subunits from the center of the superstructure to the outer parts.

We also performed competition experiments in which we used both PSs (in equal amounts) together in one synthesis batch. The resulting superstructures appear very similar to those observed when using only C6S (see Figure S7 in the Supporting Information). Thus, the interaction of C6S with the forming aggregates is much stronger than that of HYA.

Time-Dependent Evolution of the Aggregate Morphology. In order to clarify the formation mechanisms of these self-assembled PS-ZnO superstructures, we performed ex-situ SEM and PXRD investigations on both systems on samples prepared with a (1/4):1 PS:Zn ratio. Samples were removed from the synthesis batch after defined time intervals.

Focusing first on the individual crystallites, we provide their diameters in the a and c direction as well as the AR values in Table 2. After 15 min of reaction in the HYA-ZnO system, a

Table 2. Sizes of Subunits as a Function of Reaction Time[a]

	HYA			C6S		
time (min)	D_a	D_c	AR	D_a	D_c	AR
15	51	31	1.65			
30	41	44	0.93			
60	56	69	0.81			
180	54	76	0.71	50	17	2.94
300	71	90	0.79	49	16	3.06
1440	75	99	0.76	63	20	3.15

[a]Crystallite sizes D_a and D_c were deduced from the reflection broadening of the (100) and (002) reflections of zincite using Scherrer's equation. All samples were prepared with a (1/4):1 PS:Zn ratio.

pure zincite phase is observed in the XRD pattern (see Figure S8 in the Supporting Information). The subunits display platelet-like habiti, in contrast to the final rod/wedge-like appearance, with D_a of 51 nm and D_c of 31 nm. This causes a relatively large AR of 1.65. If not removed from the reaction mixture, the subunits grow further in both directions. However, growth in the c direction dominates; that is, the AR value decreases with time and subunits become rod-like. After 60 min the AR of the subunits is 0.81. Growth of the subunits seems to be completed after 300 min of reaction as diameters for D_a and D_c did not exceed 80 and 100 nm, respectively.

In the C6S-ZnO system, PXRD data show a much slower crystallization of zincite. Initially, a zinc nitrate hydroxide phase ($(Zn_5(OH)_8(NO_3)_2$, JCPDS No. 25-1028; observed after 15 min) with very low crystallinity is dominant (see Figure S8 in the Supporting Information). While the signals of the zinc nitrate hydroxide phase decrease with time, those of zincite increase. The transformation of $Zn_5(OH)_8(NO_3)_2$ to zincite has been described in the literature, although under harsher conditions (hydrothermal treatment at 160 °C).[43] The presence of the zinc nitrate hydroxide phase precludes the

determination of crystallite sizes via X-ray diffraction broadening due to overlap of the reflections of both phases. After 180 min of reaction time, pure zincite is present and crystallite size determination becomes possible. Thereafter, zincite subunits in the C6S-ZnO system display a large AR of 2.94 which is typical for this system as mentioned above. In contrast to the HYA-ZnO system, the growth of the subunits is almost completed after 180 min reaction time.

The evolution of the aggregate morphology in both superstructure systems was monitored via ex-situ SEM investigation and is presented together with the plot of AR vs time (Figure 7). The formation of the "asparagus bundle"-like HYA-ZnO superstructure proceeded within a relatively short time interval, the typical morphology becoming visible after 15 min (Figure 7a). At this stage, the superstructures had sizes of approximately 100 nm. When allowed to react further (30–300 min), the subunits increased in size, leading to a growth of the HYA-ZnO aggregates, with dimensions of up to 0.5 μm after 1440 min (Figure 7c). However, the number of crystallites in an aggregate appears to be constant. Therefore, growth of the superstructures seems to be accomplished rather by growth of the individual crystallites than by further attachment of subunits.

SEM images taken in the C6S-ZnO system after 15 min reaction time already show a morphology indicative of the product, with two discs, one larger than the other, united at a constriction plane (Figure 7d). At this stage, the diameter of the aggregates is approximately 180 nm. Those superstructures seem to consist of very small (<10 nm) subunits, the shape of which cannot be inferred from the SEM image (Figure 7d). With increasing reaction time, these subunits (while transforming into the pure zincite phase) form platelet-like crystallites which grow preferentially in the $a–b$ directions as deduced from the AR values in the later stages of the reaction. After 180 min, the typical morphology of two merged disks is observed (Figure 7g). The alignment along the c axes of the crystallites is apparently rather high at this stage; that is, the subunits lie mainly parallel to each other (compare the TEM images in Figure 6d,e as well as the SAED pattern in Figure 6e). When allowed to react further, the C6S-ZnO superstructures grow to more than 1 μm after 300 min and display a more spherical morphology (Figure 7h). The growth of these superstructures seems to be completed after 300 min as their size did not increase anymore after a longer reaction time (Figure 7i). Unlike in the HYA system, the drastical growth of the superstructures in the time interval between 180 and 300 min cannot be caused by a growth of the individual subunits, as the crystallite sizes D_a and D_c showed almost no increase in size (Table 2). Further growth of the C6S-ZnO aggregates therefore seems to be accomplished by the generation or adjoining of additional crystallites (Figure 7g–i). Additional subunits attach in a more and more inclined arrangement, leading to increasingly spherical aggregates (Figure 7h,i). These aggregates, however, did not close to spheres within a reaction time of 1440 min.

Formation Mechanisms of ZnO Aggregates. According to the results presented above, we postulate a formation mechanism for both types of PS-mediated superstructures (Figure 8).

Because of their negative charges, the PSs should strongly interact with the zinc(II) ions in solution, thus leading to local accumulations of zinc ions (Figure 8, HYA-1 and C6S-1). Crystallization starts within these local accumulations where the
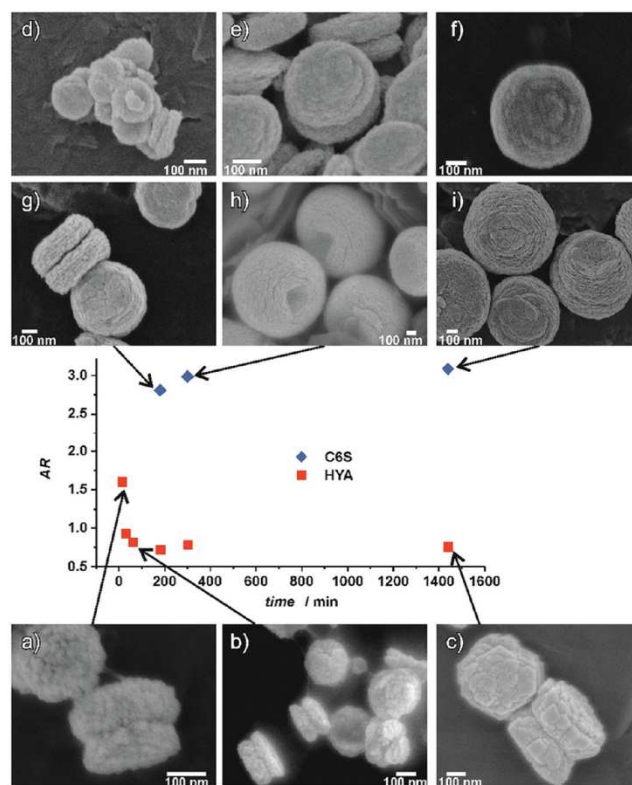
Figure 7. Aspect ratio AR = D_a/D_c, calculated from reflection broadening of the (100) and (002) reflections, as a function of reaction time; the molar ratio of the PS repeat unit and zinc ions in the solution was fixed to (1/4):1. Corresponding SEM images display the morphology of the collected precipitates: (a−c) HYA-ZnO; (d−i) C6S-ZnO. The SEM micrographs d−f correspond to non-phase-pure precursors of C6S-ZnO precipitates after 15, 30, and 60 min, respectively.

supersaturation is high (Figure 8, HYA-2 and C6S-2). Whereas in HYA-affected precipitation the formation of an intermediate phase is not observed, in the C6S-ZnO system a moderately crystalline zinc nitrate hydroxide phase is formed intermittently. This phase then transforms to zincite, probably via a dissolution−recrystallization process (Figure 8, C6S-2). It can be anticipated that the formation of this intermediate phase is driven by the higher charge density of C6S as compared to HYA, leading to a higher local supersaturation. In both reaction systems, zincite crystallites appearing early will typically have no specific shape and exhibit a variety of faces.

Upon development of more defined crystal faces, adsorption of the PS proceeds (Figure 8, HYA-3 and C6S-3). C6S with its high negative charge will interact predominantly with the positively charged (001) faces of the crystals. Although HYA, with its smaller negative charge, will also favor adsorption on these faces, the discrimination versus the {100} faces is much less pronounced. Thus, C6S strongly impedes growth along the c axis of the zincite crystals, leading to hexagonally shaped platelets. HYA also decreases growth along the c axis, but the effect is much weaker and becomes visible only for initially formed subunits or under reaction conditions with high concentrations of this PS (Tables 1 and 2). The ZnO

crystallites thus mainly retain the rod-like morphology typical of ZnO precipitated in the absence of any additive. The observation that the hexagonal morphology of the crystallites in their a−b plane appears somewhat disturbed in the HYA-ZnO system (see Figure 6c), an effect which is less pronounced for crystallites from the C6S-ZnO system could be explained by the fact that the adsorption of HYA is less specific; that is, the interaction of this PS with the {100} prism faces is relatively stronger, thus interfering with their growth. Also the observation that in competition experiments the influence of C6S dominates over that of HYA can be attributed to the stronger adsorption, as described above.

The structure of these aggregates and evidence from the staining experiments suggests that initially a "twinning" occurs by the attachment of crystallites via their (001) faces (see Figure 8, HYA-3 and C6S-3), as has been proposed before.[1,30,31,40,41] This twinning is allowed due to the adsorption of the polymers which counterbalance and possibly overcompensate the like charges on these faces. Further self-assembly of the subunits may proceed via the stacking of their polar faces of opposite charge facing each other, that is, (001) on (00$\bar{1}$) (Figure 8, HYA-4 and C6S-4).
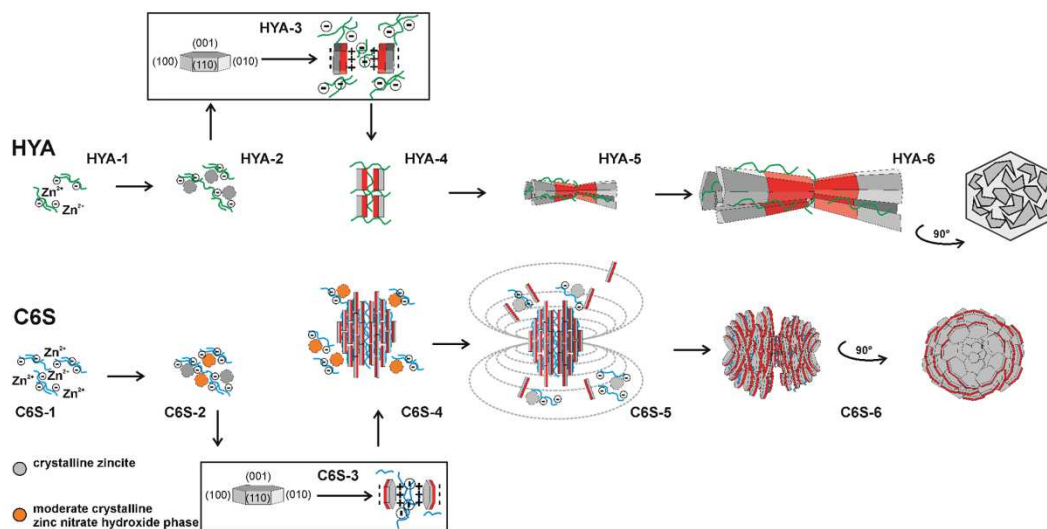
Figure 8. Scheme of the proposed formation mechanisms of PS-ZnO particles and aggregates: Formation pathway for HYA-ZnO particles and aggregates: (HYA-1) local accumulation of Zn(II) ions and HYA polymer strands; (HYA-2) nucleation of zincite crystallites without specific shape; (HYA-3) formation of crystal faces and, concomitantly, preferred adsorption of HYA on (001) faces, leading to a "twinning" in the arrangement of the subunits; (HYA-4) aggregation of subunits; (HYA-5) aggregation of subunits stops at an early stage; the superstructures grow by the growth of the subunits, leading to a bundle-like morphology, until, (HYA-6) the final HYA-ZnO superstructure is obtained. Formation pathway for C6S-ZnO particles and aggregates: (C6S-1) local accumulation of Zn(II) ions and C6S polymer strands; (C6S-2) initial nucleation of a disordered zinc nitrate hydroxide phase which slowly transforms into zincite crystallites without specific shape by a dissolution-recrystallization process; (C6S-3) formation of crystal faces and, concomitantly, preferred adsorption of C6S on (001) faces, leading to a "twinning" in the arrangement of the subunits; (C6S-4) stacking of subunits with parallel c axes and formation of sandwich-like double disk superstructure; at this stage, the zinc nitrate hydroxide phase is still present; (C6S-5) further formation of zincite platelets which become attached to the superstructures under the influence of the dipolar field of the aggregates; (C6S-6) the final C6S-ZnO superstructure is obtained.

In the HYA-ZnO system the initial subunits have platelet-like habiti and stack nearly in a parallel fashion with regard to their c axes (Figure 8, HYA-4). Evidence from ex-situ XRD peak broadening analysis and SEM investigations showed that no further addition of subunits occurs; that is, aggregates consist of a nearly constant number of subunits. Further growth of the superstructures can therefore be attributed to the growth of the subunits (Figure 8, HYA-5). This growth occurs relatively unimpeded and predominantly in the c axis direction of the crystallites, thus forming the typical "asparagus bundle"-like morphology composed of uncompleted hexagonal rods (Figure 8, HYA-6).

In the C6S-ZnO system, the zincite subunits initially also stack with their c axes parallel and form a sandwich-like double disk morphology. It should be noted that the twinning and the first aggregation of the zincite subunits occur while the less crystalline zinc nitrate hydroxide phase is still present (Figure 8, C6S-4). Probably by a dissolution recrystallization process, this phase completely transforms to zincite within the first 180 min of reaction time.

In principle, the shape of the forming zincite crystallites could also be determined by the preceding zinc nitrate hydroxide phase, if its morphology was preserved during the transformation. However, an earlier study came to the conclusion that the transformation occurs according to a non-morphology-retaining dissolution−recrystallization mechanism.[43] We therefore assume that the platelet shape of the zincite crystallites is not determined by the precursor phase, but

due to the action of C6S during precipitation. This is also supported by the fact that not only the initially formed zincite subunits show the platelet shape, but also those appended to the aggregate at later stages. In contrast to the HYA-ZnO system, growth of the ZnO subunits almost completely stops at an early stage of the superstructure formation as can be deduced from the ex-situ XRD analysis. Consequently, growth of the superstructures at later stages probably proceeds via continuous adjoinment of additional platelet-like subunits which possibly nucleate and grow in the solution. Possibly by electric fields built up during aggregate formation due to the polar character of ZnO, these platelets adjoin with an increasingly steeper angle of inclination the nearer they are to the rim of the aggregates; that is, they align according to the electrical field of the superstructures (Figure 8, C6S-5).[30,42] Thus, with increasing reaction time, the two disks evolve toward a more and more concave morphology, resulting in spherical superstructures (Figure 8, C6S-6). With continuous aggregation of the subunits, the two halves start to close until a point is reached at which this process stops, possibly due to the strong dipolar field developed by the growing aggregates and the repulsive interactions of the ($00\bar{1}$) faces of the converging zincite platelets (Figure 8, C6S-6).

■ CONCLUSION

The naturally occurring polysaccharides hyaluronic acid and chondroitin-6-sulfate exert substantial influences on the morphology of precipitating zinc oxide mesocrystals. This

influence can be attributed to their strong (HYA) and very strong (C6S) interactions with the surfaces of growing zincite crystals, resulting in different selective adsorption phenomena. These adsorption phenomena lead to different shapes of the primary ZnO crystallites, namely, to rod- and platelet-like nanocrystals, in the HYA-ZnO and in the C6S-ZnO system. These nanoscale subunits align in an orderly fashion, which is initially similar for both systems. However, the superstructure growth follows different mechanisms depending on whether the process is HYA- or C6S-mediated. In the HYA-ZnO system, after the initial aggregation, further growth of the super-structures is due to the growth of the individual subunits. In contrast, in the C6S-ZnO system further growth proceeds by continuous adjoinment of additional subunits, a process that is governed by the electric field developed by the aggregates. The different influences of the two polysaccharides may be exploited in the designed construction of ZnO nanoscale devices, for example, in the preparation of thin films.

■ ASSOCIATED CONTENT

Ⓢ Supporting Information

Zeta-potential versus pH graph, thermogravimetric data of HYA-ZnO and C6S-ZnO samples, SEM micrographs of latex beads staining, comparative SEM micrographs of HYA(1600 kDa)-ZnO and HYA(10–50 kDa)-ZnO, nitrogen physisorption measurements at 77 K, STEM micrographs of HYA-ZnO and C6S-ZnO, SEM micrographs of precipitate obtained in mixed HYA/C6S experiments, ex-situ PXRD pattern of HYA-ZnO and C6S-ZnO after different time intervals.

This information is available free of charge via the Internet at http://pubs.acs.org/.

■ AUTHOR INFORMATION

Corresponding Author

*Phone +49511-762/3660. Fax: +49511-762/3006. E-mail: Peter.Behrens@acb.uni-hannover.de. Web: www.aci.uni-hannover.de.

Notes

The authors declare no competing financial interest.

■ REFERENCES

(1) Tomczak, M. M.; Gupta, M. K.; Drummy, L. F.; Rozenzhak, S. M.; Naik, R. R. *Acta Biomater.* **2009**, *5*, 876–882.

(2) Peng, Y.; Xu, A.-W.; Deng, B.; Antonietti, M.; Cölfen, H. *J. Phys. Chem. B* **2006**, *110*, 2988–2993.

(3) Cao, X.; Wang, N.; Wang, L.; Guo, L. *J. Nanopart. Res.* **2010**, *12*, 143–150.

(4) Cho, S.; Jang, J.-W.; Lee, J. S.; Lee, K.-H. *Langmuir* **2010**, *26*, 14255–14262.

(5) Gan, Y.; Gu, F.; Han, D.; Wang, Z.; Guo, G. *J. Nanomater.* **2010**, 289173, doi:10.1155/2010/289173.

(6) Raula, M.; Rashid, M. H.; Paira, T. K.; Dinda, E.; Mandal, T. K. *Langmuir* **2010**, *26*, 8769–8782.

(7) Sepulveda-Guzman, S.; Reeja-Jayan, B.; de la Rosa, E.; Torres-Castro, A.; Gonzalez-Gonzalez, V; Jose-Yacaman, M. *Mater. Chem. Phys.* **2009**, *115*, 172–178.

(8) Wang, Z. L. *J. Phys.: Condens. Matter* **2004**, *16*, 529–858.

(9) Ashtaputre, S; Marathe, S; Kulkarni, S. J. *Mater. Sci.* **2007**, *42*, 9990–9994.

(10) Yan, X; Li., Z; Zou, C.; Li, S.; Yang, J.; Chen, R.; Han, J.; Gao, W. *J. Phys. Chem. C* **2010**, *114*, 1436–1443.

(11) Kon, K.; Brauer, C. N.; Hidaka, K.; Löhmannsröben, H.-G.; Karthaus, O. *Langmuir* **2010**, *26*, 12173–12176.

(12) Su, Y. K.; Peng, S. M.; Ji, L. W.; Wu, C. Z.; Chen, W. B.; Liu, C. H. *Langmuir* **2010**, *26*, 603–606.

(13) Chang, S.-P.; Chang, S.-J.; Lu, C.-Y.; Li., M.-J.; Hsu, C.-L.; Chiou, Y.-Z.; Hsueh, T.-J.; Chen, I.-C. *Superlattices Microstruct.* **2010**, *47*, 772–778.

(14) Das, S. N.; Kar, J. P.; Choi, J.-H.; Lee, T. I; Moon, K.-J.; Myoung, J.-M. *J. Phys. Chem. C* **2010**, *114*, 1689–1693.

(15) Jiao, Y.; Zhu, H. J.; Zhou, M. J.; Wang, X. F.; Li, Q. *J. Phys. Chem. C* **2010**, *114*, 208–211.

(16) Fei, P.; Yeh, P.-H.; Zhou, J.; Xu, S.; Gao, Y.; Song, J.; Gu, Y.; Huang, Y.; Wang, Z. L. *Nano Lett.* **2009**, *9*, 3435–3439.

(17) Lee, J.-H.; Park, B.-O. *Thin Solid Films* **2003**, *426*, 94–99.

(18) Lee, G. J.; Min, S.-K.; Oh, C.-H.; Lee, Y.; Lim, H.; Cheong, H.; Nam, H. J.; Hwangbi, C. K.; Min, S.-K.; Han, S.-H. *J. Nanosci. Nanotechnol.* **2011**, *11*, 511–517.

(19) Govender, K.; Boyle, D. S.; Kenway, P. B.; O'Brien, P. *J. Mater. Chem.* **2004**, *14*, 2575–2591.

(20) Yi, S.-H.; Choi, S.-K.; Jang, J.-M.; Kim, J.-A.; Jung, W.-G. *J. Colloid Interface Sci.* **2007**, *313*, 705–710.

(21) O'Brien, P.; Saeed, T.; Knowles, J. *J. Mater. Chem.* **1996**, *6*, 1135–1139.

(22) McPeak, K. M.; Le, T. P.; Britton, N. G.; Nickolov, Z. S.; Elabd, Y. A.; Baxter, J. B. *Langmuir* **2011**, *27*, 3672–3677.

(23) Cho, S.; Jung, S.-H.; Lee, K.-H. *J. Phys. Chem. C* **2008**, *112*, 12769–12776.

(24) Raula, M.; Rashid, M. H.; Paira, T. K.; Dinda, E.; Mandal, T. K. *Langmuir* **2010**, *26*, 8769–8782.

(25) Liu, X.; Afzaal, M.; Ramasamy, K.; ÒBrien, P.; Akhtar, J. *J. Am. Chem. Soc.* **2009**, *131*, 15106–15107.

(26) Cong, H.-P.; Yu, S.-H. *Adv. Funct. Mater.* **2007**, *17*, 1814–1820.

(27) Zhang, T.; Dong, W.; Keeter-Brewer, M.; Konor, S.; Njabon, R. N.; Tian, Z. R. *J. Am. Chem. Soc.* **2006**, *128*, 10960–10968.

(28) Yao, K. Y.; Sinclair, R.; Zeng, H. C. *J. Phys. Chem. C* **2007**, *111*, 2032–2039.

(29) Liang, J.; Bai, S.; Zhang, Y.; Li, M.; Yu, W.; Qian, Y. *J. Phys. Chem. C* **2007**, *111*, 1113–1118.

(30) Liu, Z.; Wen, D.; Wu, X. L.; Gao, Y. J.; Chen, H. T.; Zhu, J.; Chu, P. K. *J. Am. Chem. Soc.* **2009**, *131*, 9405–9412.

(31) Taubert, A.; Palms, D.; Weiss, Ö.; Piccini, M.-T.; Batchelder, D. N. *Chem. Mater.* **2002**, *14*, 2594–2601.

(32) Muñoz-Espí, R.; Jeschke, G.; Lieberwirth, I.; Gómez, C. M.; Wegner, G. *J. Phys. Chem. B* **2007**, *111*, 697–707.

(33) Wu, Q.; Chen, X.; Zhang, P.; Han, Y.; Chen, X.; Yan, Y.; Li, S. *Cryst. Growth Des.* **2008**, *8*, 3010–3018.

(34) Gerstel, P.; Lipowsky, P.; Durupthy, O.; Hoffmann, R. C.; Bellina, P.; Bill, J.; Aldinger, F. *J. Ceram. Soc. Jpn.* **2006**, *114*, 911–917.

(35) Liu, Y.; Afzaal, M.; Badcock, T.; Dawson, P.; ÒBrien, P. *Mater. Chem. Phys.* **2011**, *127*, 174–178.

(36) Wang, A.-J.; Liao, Q.-C.; Feng, J.-J.; Zhang, P.-P.; Li, A.-Q.; Wang, J.-J. *CrystEngComm* **2012**, *14*, 256–263.

(37) Behrens, P.; Baeuerlein, E. In *Handbook of Biomineralization: Biomimetic and Bioinspired Chemistry*; Behrens, P.; Baeuerlein, E., Eds.; Wiley-VCH: Weinheim, 2007; Vol. 2.

(38) Li, W.-J.; Shi, E.-W.; Zhong, W.-Z.; Yin, Z.-W. *J. Cryst. Growth* **1999**, *203*, 186–196.

(39) Cölfen, H.; Antonietti, M. *Angew. Chem., Int. Ed.* **2005**, *44*, 5576–5591.

(40) Jia, L.; Cai, W.; Wang, H.; Zeng, H. *Cryst. Growth Des.* **2008**, *8*, 4367–4371.

(41) Tseng, Y.-H.; Lin, H.-Y.; Liu, M.-H.; Chen, Y.-F.; Mou, C.-Y. *J. Phys. Chem. C* **2009**, *113*, 18053–18061.

Crystal Growth & Design   Article

(42) Wang, T. X.; Cölfen, H.; Antonietti, M. *Chem.—Eur. J.* **2006**, *12*, 5722−5730.
(43) Musić, S.; Dragčević, Đ.; Popović, S. *J. Alloys Compd.* **2007**, *429*, 242−249.

5 Zinc Oxide Films via Polysaccharide-Mediated Chemical Bath Deposition

5.1 Preface

This chapter contains a manuscript dealing with the growth of zinc oxide films wherein the morphology of the films is controlled by the addition of hyaluronic acid. This manuscript has been submitted as a full paper to *Thin Solid Films*.[181] The submitted manuscript of this full article is presented here in subsection 5.2. The study and the work were motivated by the high potential of ZnO as transparent conductive oxide (TCO) in film applications and benefited from the expertise gained in the study on ZnO precipitation under the influence of polysaccharides (PSs), see subsection 4. Principles of growth control of ZnO precipitates with PSs addition were successfully transferred to ZnO film deposition experiments. In this way, ZnO films with very high qualities in terms of electrical conductivity and transparency could be prepared.

The general interest of industry in such high-quality films of TCOs is expressed by the co-authorship of Priv.-Doz. Dr. Stefanie Eiden from Bayer Technology Services GmbH. The initial work promoted the installation of the BMBF-funded project Carbofilm within the research initiative Inno.CNT.

The deposition experiments as well as the FE-SEM study, conductivity measurements, XRD and UVVis investigations were all performed by myself, with the assistance of Hans-Christoph Schwarz. Priv.-Doz. Dr. Stefanie Eiden and Dr. Andreas M. Schneider have provided valuable suggestions and advice. The results presented in this manuscript were presented on a poster on the conference Inno.CNT 2011 and also served as the basis of a submitted patent application.[182,183]

181) Waltz F, Schwarz H-C, Schneider AM, Eiden S, Behrens P, submitted to *Thin Solid Films* on March 12, **2012**. As of June 11, 2012 the status is still reported as "under review" on the website of the journal.
182) Behrens P, Benecke C, Eiden S, Reusch T, Schneider AM, Waltz F, Inno.CNT, Jan. 25-27, **2011**, Ettlingen.
183) Behrens P, Schneider AM, Waltz F, Nasschemisches Verfahren zur Herstellung leitfähiger Beschichtungen basierend auf transparenten Oxiden, patent application submitted to the European patent office on Oct. 23, **2011**.

5.2 Publication
Morphology Control of Zinc Oxide Films via Polysaccharide-Mediated Low-Temperature Chemical Bath Deposition

Florian Waltz, Hans-Christoph Schwarz, Andreas M. Schneider, Stefanie Eiden, and Peter Behrens

As presented here, the manuscript was slightly re-edited as compared to the submitted file. In order to enhance the legibility for the readers, the number of columns, and the placement of the tables and figures were changed.

Morphology Control of Zinc Oxide Films via Polysaccharide-Mediated Low-Temperature Chemical Bath Deposition

Florian Waltz,[1] Hans-Christoph Schwarz,[1] Andreas M. Schneider,[1] Stefanie Eiden,[2] Peter Behrens[1]*

[1]Institut für Anorganische Chemie, Leibniz Universität Hannover, Callinstr. 9, D-30167 Hannover, Germany, and ZFM - Center for Solid-State Chemistry and New Materials, Leibniz Universität Hannover

[2]Bayer Technology Services GmbH, 51368 Leverkusen, Germany

*Phone: +49511/762-3360
Fax: +49511/762-3006
E-mail: peter.behrens@acb.uni-hannover.de

Abstract

In this study we present a three-step process for the low-temperature chemical bath deposition of crystalline ZnO films on glass substrates. The process consists of a seeding step followed by two chemical bath deposition steps. In the second step (the first of the two bath deposition steps), the addition of a natural polysaccharide, namely hyaluronic acid, is used to manipulate the morphology of the films. The influence of hyaluronic acid and the time of its addition on the ZnO film morphology were investigated. By elaborate adjustment of the parameters in this step, the film morphology can be tailored to provide an optimal growth support for the third step (a subsequent chemical bath deposition step), in which the film is sealed to give a dense layer of ZnO. The optimized procedure leads to a dramatic decrease of the electrical resistivity of the ZnO films. The films were characterized by means of electron microscopy, X-ray diffraction and measurements of the electrical conductivity.

transparent conductive oxide, zinc oxide, polysaccharide, chemical bath deposition, thin film

1. Introduction

Zinc oxide is a unique material with a number of interesting properties such as piezo- and pyroelectricity [1,2], high optical transparency [3], catalytic activity [4,5], and chemical sensing [6-8]. It is also one of the most promising candidates for the replacement of indium tin oxide (ITO) in transparent conductive oxide (TCO) applications [9,10]. Hence, ZnO films are a key research area in industry as well as in academia with more than 3200 publications in 2011 (Thomson Reuters, Web of Knowledge). Several methods have been used to apply ZnO on different substrates, e.g. pulsed laser deposition (PLD) [11], chemical vapor deposition (CVD) [12,13], as well as wet chemical approaches like sol-gel synthesis [14] and chemical bath deposition (CBD) [15-18]. Among these, CBD methods have gained increasing interest since they allow the deposition of ZnO films in large-scale applications at low temperature, on a number of different substrates with minor laboratorial effort.

ZnO is a semi-conducting ceramic material with a direct band gap of 3.37 eV and an exciton binding energy of 60 meV [19]. Although ZnO is reported to be an n-type semiconductor, caused most likely by the hydrogen impurities which act as a shallow donor, it is a challenging task to control its conductivity [20]. In general, in applications where highly conductive

materials are required, e.g. solar cells and light emitting diodes (LEDs), ZnO has to be doped.

Several groups have reported about the successful doping of ZnO films with dopants like magnesium [21], iodine [22], boron [23,24], titanium [25], manganese [26], and aluminium [27-29]. These films are grown via CBD or related techniques (e.g. double dip or hot water dipping), respectively. In CBD processes hexamethylenetetramine (HMTA) is usually dissolved in a solution containing Zn(II) ions. At a certain temperature, HMTA decomposes and thus delivers hydroxide ions forcing the formation of crystalline ZnO [30]. Doping is carried out by the simple addition of the corresponding dopant salt to the deposition solution. In addition to doping, the microstructure of a thin film, which involves crystallite size, aspect ratio morphology and intergrowth, has a decisive influence on many applications, e.g. in sensors and catalysts [8,31].

As the wurtzite structure of ZnO is polar, crystals of the substance feature two differently charged surfaces, the oxygen terminated (00-1) and the zinc terminated (001) faces, on which charged molecules can be chemisorbed by electrostatic interaction. In addition, the uncharged {100} faces of ZnO can support the physisorption of molecules. Such adsorption phenomena can influence the growth rate of the corresponding faces, leading to different habiti of the crystals.

Solvent-based chemical deposition processes are particularly suited for the addition of molecules that may control the morphology of ZnO crystals and their aggregates as well as ZnO films. Molecules like citrate [31,32], histidine [33], polyvinylpyrrolidone[34], malate [35], ascorbate [36], diaminopropane [37] and cetyltrimethylammonium bromide (CTAB) [38] have already been successfully applied in this respect. Recently, we have investigated the influence of two polysaccharides, hyaluronic acid (HYA) and chondroitin-6 sulfate (C6S), on the morphology of primary ZnO crystallites

and on their aggregates, as they are formed in precipitation experiments [39]. Whereas C6S leads to a pronounced platelet-like morphoplogy of the primary crystallites, HYA leads to the growth of small wedge-like particles and the aggregation of these particles to bundles. We have surmised that this influence of HYA might be beneficial to the quality of deposited thin ZnO films by increasing the number of primary crystallites, which should lead to finer structured films with more strongly intergrown crystals, thus enhancing electrical conductivity and optical transparence. Therefore, we have undertaken the study presented here, where ZnO films have been prepared in a three-step process, starting with a seeding step, followed by two CBD steps (Figure 1).
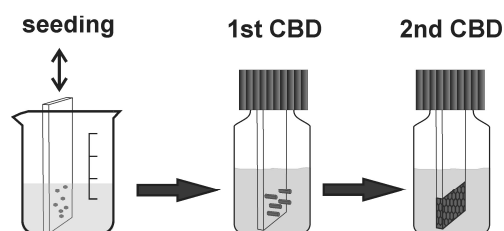

Figure 1. Scheme of the three-step ZnO film deposition process. Seeds were deposited on glass slides by immersion in Zn(II) solutions followed by annealing. In the first CBD, different ZnO morphologies can be grown depending on the point-of-time of HYA addition. In the second CBD a dense film is formed.

In the first of the two CBDs, HYA was added at different times in order to optimize the quality of the obtained films. The properties of the obtained films have been studied by means of field emitting scanning electron microscopy (FE-SEM), X-ray diffractometry (XRD), UVVis spectroscopy and measurements of electrical conductivity.

2. Experimental Details

2.1 Film Deposition

All experiments were performed with micro-pore filtered water (Clear UV, SG Wasseraufbereitung und

Regenerierungsstation GmbH, Hamburg) up to a conductivity of 0.055 µS/cm). Films on glass slides were prepared in three steps according to Figure 1.

i. First step: seeding. Crystalline precursors were deposited on glass slides by a protocol according to Greene and co-workers [40]. For this purpose, the glass slides were immersed in a 5 mM Zn(II)-acetate dihydrate (reagent grade, Aldrich) ethanolic solution for 10 seconds, then cleaned with ethanol. This procedure was repeated five times. Afterwards the films were annealed at 350 °C for 20 min. The whole procedure was repeated once [40].

ii. Second step: first CBD. The deposition of ZnO on the seeded glass slides was performed in 100 mL screw cap bottles containing 0.75 g zinc nitrate hexahydrate (purum, Aldrich) and 0.35 g hexamethylentetramine (HMTA, puriss, Aldrich) dissolved in 75 mL water. The mixture was vigorously stirred until a nearly clear solution was obtained. The seeded glass slides were immersed into this solution and fixed in a vertical position by using a holding device machined from Teflon. This corresponds to the start of the time measurement. The reaction was initiated by rapid heating to 90 °C while stirring gently. 83 mg of hyaluronic acid (HYA, sodium salt from *Streptococcus equi*, MW ~ 1600 kDa, Aldrich) was dissolved in 25 mL water under vigorous stirring and added to the solution described above after a certain time (0, 15, 30 and 45 min, resp.). The amount of HYA added corresponds to a molar ratio of (1/12):1 with regard to the repeating unit of HYA (M = 401.3 g/mol) and the Zn(II) ion concentration. The combined solutions were kept at 90 °C for one hour in total. Afterwards, the glass slides were taken out of the screw cap, rinsed with water, washed carefully with ethanol in an ultrasonic bath, and dried at 60 °C.

iii. Third step: second CBD. The second CBD was performed according to reaction conditions reported by Baxter and Schmuttenmaer [41]. 2.97 g Zinc nitrate hexahydrate (purum, Aldrich) and 1.405 g hexamethylentetramine (HMTA, puriss, Aldrich) were dissolved in 100 mL water under vigorous stirring in a screw cap bottle until an almost clear solution was obtained. Glass slides which had been treated according to step 1 and 2 were dipped into this solution and arranged vertically by a Teflon holder. The reaction was initiated by heating the screw cap bottle rapidly to 85 °C under gentle stirring. After one hour the glass slides were removed from the screw cap bottle, rinsed with water, washed carefully with ethanol in an ultrasonic bath, and dried at 60 °C.

2.2 Characterization

X-ray diffraction patterns were recorded on a STOE (Darmstadt, Germany) Theta-Theta diffractometer in reflection geometry using monochromatized Cu-Kα radiation. SEM micrographs were taken on a JEOL (Tokyo, Japan) 6700F FE-SEM operating with an acceleration voltage of 2 kV and a working distance of 3 mm. For electron microscopy analyses glass slides with deposited ZnO were cut properly and fixed with silver paste (Plano GmbH, Wetzlar, Germany) on a copper block. The average film thicknesses were determined with the program ImageJ 1.43 based on cross section FE-SEM micrographs by measurement of at least four different locations. UVVis transmission measurements were performed on a Cary 5E spectrometer (Varian Inc., Palo Alto, USA) in order to determine the optical transparency of the ZnO films. To ensure that only the transmittance of the ZnO films is measured, the spectrum of a cleaned glass slide was used as background correction. Contact angle measurements of the ZnO films were carried out using a Surftens apparatus (OEG GmbH Frankfurt, Germany). Electrical conductivity measurements were performed with a 2100 Multimeter (Keithley Instruments Inc., Cleveland, USA). For conductivity measurements the films were contacted by

2 parallel lines of silver paste (Plano GmbH, Wetzlar, Germany) 1 cm in length and with 1 cm distance between them. Sheet resistivities of the fully processed films were recorded under UV irradiation (370 nm, 8 W power). Specific resistivity values were calculated as product of the sheet resistance with the thickness of the corresponding film.

3. Results and Discussion

ZnO films were prepared according to the three-step process described in the experimental section and depicted in Figure 1.

3.1 Step 1: Seeding

Solution-based growth of zincite in general requires prior application of crystalline seeds on the support. In our hands, the solution deposition procedure according to Greene and coworkers led reproducibly to high film quality in the final state [40].The seeding did not lead to any clouding of the glass slides, which would be observable with the naked eye. XRD patterns of glass slides seeded in this way display only a broad signal originating from the amorphous glass [data not shown]. FE-SEM also failed to visualize the seeds on the glass slides, probably due to their small size and the strong electric charging on the support.

However, indirect evidence for a successful seeding can be presented. Contact angle measurements show that the slides are slightly more hydrophobic after the seeding process, i.e. the contact angle of a seeded glass slide is about 58° in comparison to 46° of a clean glass slide. Furthermore, UVVis spectra of seeded glass slides show an absorption band in the UV range at about the energy of the band gap of ZnO (3.37 eV) [data not shown]. Final evidence lies in the efficient growth of ZnO on seeded slides; in contrast, unseeded slides did not properly support the growth of ZnO.

3.2 Step 2: First CBD

In the absence of hyaluronic acid (HYA), highly vertically aligned ZnO nanorods grow on priorly seeded glass slides, when the procedure described in the experimental section is applied. The growth of aligned ZnO nanorods arrays on different substrates has been reported before [15,17,40,42]. The scanning electron micrographs in Figure 2 show a nanorod array which had grown for 1 h.
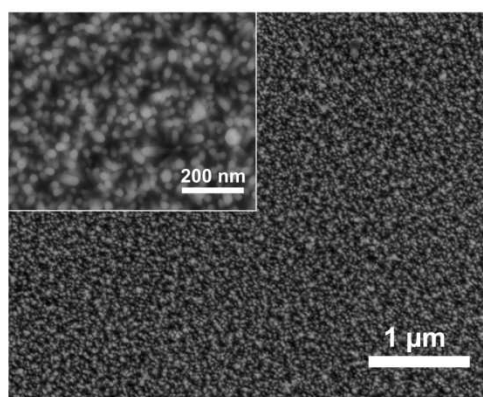

Figure 2. SEM micrographs of a ZnO nanorod array grown on a seeded glass slide for 1 h without the addition of HYA; inset shows higher magnification.

In X-ray diffraction experiments, arrays of this kind display only the (002) reflection of zincite due to the strong texture of the crystals with their c axis perpendicular to the support [Figure 3].
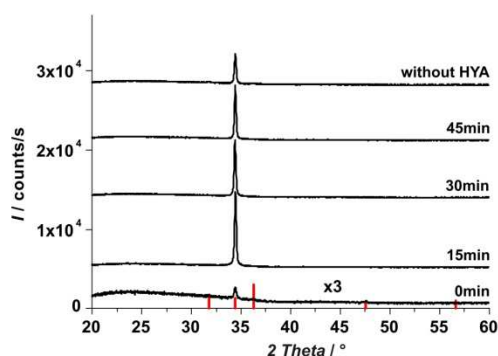

Figure 3. X-ray diffraction patterns of ZnO films after the first CBD. Growth was performed for 1 h in total with and without HYA addition. HYA was added after different

times as indicated in the figure. Bars represent the zincite reference [50].

As demonstrated previously, the addition of natural polysaccharides affects the morphology of ZnO crystallites precipitated from solution [39,43,44]. This occurs largely by the blocking of specific crystal faces during growth. In precipitation experiments, performed under conditions which are very similar in concentrations and temperatures to typical ZnO CBD processes, the addition of HYA led to the formation of well-defined and highly symmetric ZnO mesocrystals. The size of the individual ZnO particles was dramatically decreased from micrometers down to the nanometer scale [39].

In order to investigate the influence of HYA on the morphology of deposited zinc oxide, we added HYA dissolved in water during the first CBD after different time intervals (0, 15, 30 and 45 min, respectively). The growth of the ZnO nanorods (Figure 2) is assumed to proceed continuously on the seeded glass slides until HYA is added to the reaction mixture. Directly after its addition, HYA may affect the further deposition and growth of ZnO.

XRD patterns of films obtained after the first CBD (Figure 3) display only the (002) reflection of zincite, irrespectively of whether HYA was supplied or not. This finding proves the perpendicular alignment of the *c* axes of the ZnO crystallites with regard to the glass surface, which is unaffected by the addition of HYA.

However, the intensity of the (002) reflection is very weak for a film grown with instant addition of HYA, indicating a strong decrease in the deposited amount of ZnO. When the addition of HYA occurs at a later point in time (15, 30 and 45 min), the (002) signal becomes more intense, showing that more ZnO has grown on the substrate. These findings agree with the assumption that the presence of HYA decreases the ZnO deposition rate, for example by blocking the growth of certain crystal faces. Curiously, the sample

prepared without any HYA addition displays a weaker signal than samples with HYA added after 15, 30 and 45 min; this finding will be further discussed with regard to SEM investigations.

Whereas the crystallographic orientation of the ZnO crystallites on the support is not affected by the addition of HYA, the ZnO film morphology changes dramatically when the CBD is performed in the presence of HYA. This is exhibited in SEM micrographs providing views onto the plane of the deposited films (Figure 4).
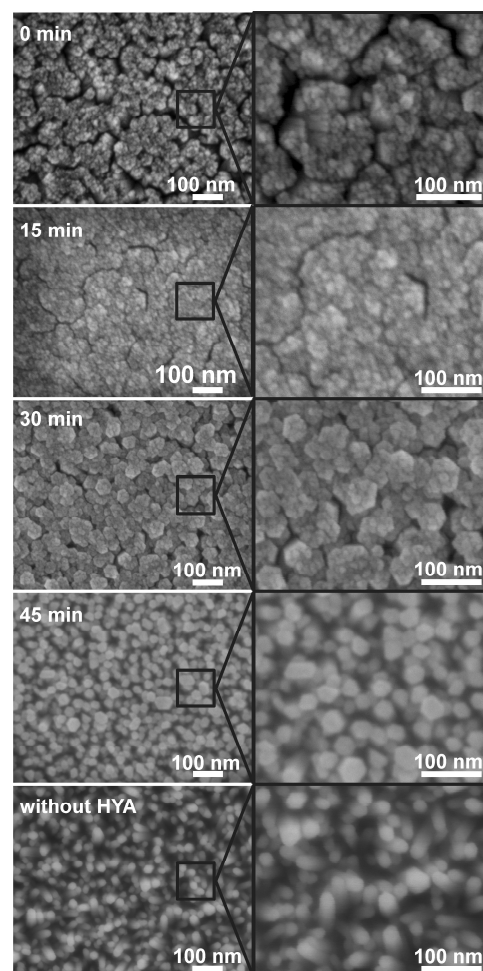

Figure 4. SEM micrographs of ZnO films after the first CBD. HYA was supplied after specific time intervals during the growth process as indicated.

In general, the diameter of the individual ZnO nanorods decreased strongly when the HYA is added within the first 30 min of reaction, i.e. much finer structures were obtained. However, the individual nanocrystallites align themselves to larger aggregates, i.e. the deposits can better be described as bundles of needles than as individual nanorods. This is comparable to precipitation experiments, in which HYA adsorbs onto ZnO crystallites during their growth and thereby influences their size and aspect ratio. Furthermore, those ZnO sub-units aggregate under the influence of HYA to highly ordered mesocrystals, which was proven via SEM investigations and selected area electron diffraction [39]. In the film deposition experiments described here, these aggregates even display a common hexagonal morphology, which can for example be seen in Figure 4 on the product prepared with HYA addition after 30 min. Such a kind of symmetrical aggregation is a hint for mesocrystal formation on the support. When HYA is added only after 45 min of reaction time, it has no significant influence on the morphology of the film; in fact, the SEM image of this sample is similar to that of the sample prepared without HYA addition. We assume that the zinc ions have almost been consumed after this reaction time and that growth has been completed. With regard to the increasing intensities of the (002) reflections in the XRD patterns of the films after 15, 30 and 45 minutes reaction, the SEM micrographs indicate that this increase is due to an increased lateral growth of the ZnO crystallites, which confirms that more ZnO was deposited when the HYA was added at a later point of time. On the contrary, the sample where HYA was added instantaneously, shows also a very dense lateral growth, whereas the XRD reflection intensity is very weak. We therefore assume, that the growth perpendicular to the support is inhibited by the instant HYA addition, which would lead to a lower mass of grown ZnO, and consequently to a less intense signal in the XRD pattern. This assumption will be further discussed with

support of cross section SEM investigations presented in section 3.3.

3.3 Step 3: Second CBD

During the first CBD, the morphology of ZnO grown on the seeded glass slides can be tailored by the addition of HYA: When no HYA is added or when it is added only after 45 min, nanorod arrays are formed. When HYA is added instantaneously or up to a reaction time of 30 minutes, finely structured bundles of needle-shaped ZnO crystals are observed. Since the crystalline domains of these small crystallites do not overlap very well after the bio-growth step, the electrical conductivity is only moderate. Sheet resistivities of films after the first CBD are typically in the range of $M\Omega/sq$. Therefore, an additional step is necessary to grow a dense ZnO film in order to yield low electrical resistance. Reaction conditions for this final growth step were adopted from Baxter and Schmuttenmaer, who obtained intergrown ZnO films after a reaction time of 3 h [41]. In our experiments, the reaction time could be reduced to 1 h due to the excellent growth conditions provided by the substrate during the first CBD. XRD patterns recorded after this third step show only (002) reflections (Figure 5), irrespective of the details of the first CBD step, proving that the growth of ZnO continues to proceed with the c axis perpendicular to the support.
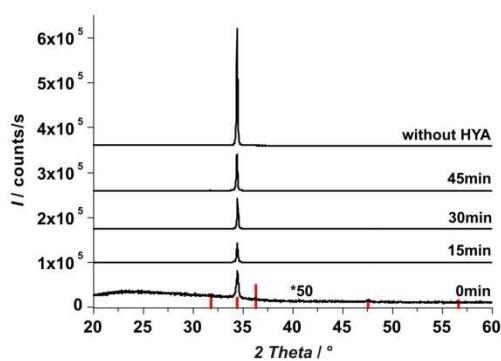

Figure 5. X-ray diffraction patterns of ZnO films after the second CBD. The films differ in the addition time of the HYA in the first CBD (from 0 min up to 45 min). Bars represent the zincite reference [50].

In general, the intensity of the (002) signal increased strongly after performing the third step compared with the ones obtained after the first CBD, indicating further successful deposition of ZnO. However, the intensities differ between the samples after the third step:

- The film which was grown in the first CBD with instant HYA addition shows the weakest signal, leading to the conclusion, that this film supports further ZnO growth the least.

- Samples prepared in the first CBD with HYA addition in the time interval from 15 to 45 min show a slight increase in the intensity of the (002) signal after the third step. The increase is stronger when HYA was added later.

- The film which was prepared with no HYA addition shows a 3-times higher signal than films grown with HYA in the first CBD, i.e. a higher amount of ZnO was deposited.

Obviously not only the growth of the films in the first CBD is affected by the HYA addition, but also the growth rate in the second CBD is strongly influenced.

The film morphology after the second CBD determines the final properties of the films. Figure 6 displays SEM micrographs of these films taken in plan view and as cross section. All films show hexagonal poles oriented perpendicular to the support with lateral sizes in the range of 200 nm. However, they differ strongly in the degree of intergrowth, depending upon the addition and the addition time of HYA during the first CBD. Whereas the films prepared with HYA addition exhibit highly intergrown crystallites – among these the effect is weakest for the film prepared with an addition time of 30 min – the crystallites on the film prepared without HYA display a much weaker crystallite intergrowth.
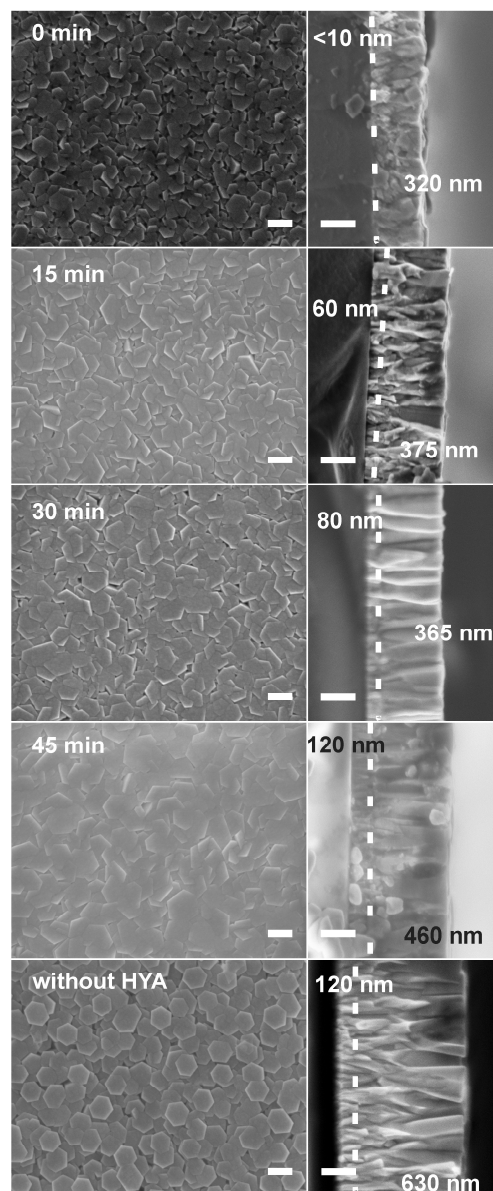

Figure 6. SEM micrographs in plan view (left) and corresponding cross sections (right) of ZnO films after the second CBD; films were prepared without HYA and with different addition times of HYA in the first CBD (scale bars 200 nm). The dotted lines indicate the interface between the ZnO grown in the first and the second CBD. The values in nm correspond to the film thicknesses of the ZnO grown within the first (to the left of the dotted line) and the second CBD (to the right of the dotted line), respectively.

The corresponding cross section SEM micrographs of the ZnO films affirm the results of the XRD analyses. The addition of HYA in the first CBD affects the amount of ZnO deposited in the second CBD. The maximum overall film thickness was achieved without addition of HYA, the film grew up to a thickness of approx. 750 nm. The earlier HYA had been added in the first CBD, the more the perpendicular growth was inhibited in the second CBD. Thus, the thinnest films (ca. 320 nm) are obtained by instant addition of HYA. Consecutively, the film thickness increases nonlinearly from 435 and 460 to 590 nm in the order of addition times of 15, 30 and 45 min. The cross section SEM images of the films (micrographs on the right of Figure 6) reveal further details of their morphology. A rod-like morphology can be assigned to zincite crystallites deposited during the first CBD whereas a more branching growth has obviously occurred during the second CBD (these two regions are separated by dotted lines in the micrographs in Figure 6). The individual film thicknesses taken from the cross section SEM micrographs are compiled in Table 1.

Table 1. Individual film thicknesses of ZnO films.

time of HYA addition during the first CBD	film thickness in nm	
	after first CBD	after second CBD
0 min	<10	320
15 min	60	375
30 min	80	365
45 min	120	460
no addition	120	630

Samples were grown in first CBD with different addition times of HYA and without addition, respectively. Individual film thicknesses of films grown in the first and in the subsequent CBD, respectively, were deduced from cross section SEM micrographs.

Obviously, the thickness of films grown in the first CBD varies strongly with the addition time of HYA during this step: The later HYA is added, the thicker the film grows during this step. The thickness increased from <10 nm for films prepared with instant HYA addition to 120 nm when HYA is added after 45 min during the first CBD. Noteworthy, the film grown with no HYA addition in the first CBD also displays a thickness of 120 nm, corroborating the finding that the growth of the ZnO film has already ceased at this point-of-time. We conclude that the addition of HYA strongly suppresses the growth of ZnO perpendicular to the support.

Film thicknesses of films grown in the second CBD on the layers formed in the first CBD also follow a certain trend, i.e. the films deposited during the first CBD step influence the thickness of the films after the second CBD. The earlier HYA is added during the first CBD, the thinner the films obtained after the second CBD are. ZnO film thicknesses increased from 320 nm (for films which were prepared with instant addition of HYA during the first CBD) to 460 nm (when the addition took place only after 45 min). The film grown on a substrate which was prepared in the first CBD without HYA addition displays the largest thickness of about 630 nm. This also demonstrates that the films obtained in the first CBD strongly influence the further ZnO deposition.

The transmittance of the films is not influenced by the addition of HYA. For films prepared with and without HYA addition, average transmittances of ca. 80% are observed in the visible range.

Joining the results from XRD and FE-SEM investigations to form a common picture, we propose the following mechanism for the film formation in the described process (Figure 7): Seeds deposited in the first step support the growth of ZnO. On such seeds, an array of highly vertically aligned ZnO nanorods grows under CBD conditions as reported earlier [15,17,40,42]; noteworthy, these nanorods do not overlap. Thus, although the thickness of such a nanorod array is quite large (120 nm), the actual

mass deposited (as inferred from the intensity of the XRD signal) is rather small.
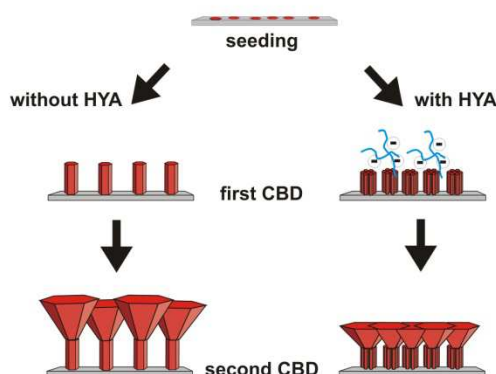

Figure 7. Scheme of the proposed mechanism of the three-step ZnO film deposition process described in this work.

During the subsequent CBD process, following the protocol of Baxter and Schmuttenmaer [41], these ZnO nanorods intergrow to a dense layer [41]. Compared to the films reported by Baxter and Schmuttenmaer, our films prepared in the presence of HYA appear more dense and regular at the surface. When HYA is added during the first CBD step, vertical growth is hampered. This effect is most noteworthy when HYA is added instantaneously and such film only has a thickness of less than 10 nm. When HYA is added at 15 or 30 min after the start of the CBD, the film thickness increases to 60 or 80 nm, respectively. However, according to the intensities observed in XRD, much more ZnO is deposited in these cases. This can be explained by an enhanced lateral growth of the nanorod bundles onto the support during the first CBD step, as judged from the SEM images in Fig. 4. The earlier HYA is added during this step, the more the individual nanorods overlap. These differences of the films then also lead to different growth characteristics in the subsequent CBD process. In general, the films become thinner and are more strongly intergrown after the final CBD when HYA was present in the first CBD. We surmise that due to the stronger lateral deposition of ZnO in the first CBD step, more supporting surface area for further ZnO growth during

the final CDB is available. This surface area is finely structured as it is based on bundles of thin zincite crystallites; each of the latter could possibly serve as nucleation center for crystal deposition during the subsequent CBD. Thus, the bundled ZnO rods which have grown preferably laterally during the first CBD allow the formation of a denser ZnO layer during the final CBD; consequently, as the materials supply is limited, axial growth is diminished, i.e. the films become thinner.

3.4. Electrical properties of the films

ZnO is a semiconductor with a direct bandgap of 3.37 eV [19]. At room temperature and in darkness, ZnO provides only very few charge carriers in the conduction band leading to an only moderate electrical conductivity [46]. Therefore, the sheet resistances of our films range above 10 MOhms/sq. The conductivity of ZnO increases dramatically when it is exposed to a light source. Improved conductivities can also be achieved via doping of ZnO [47-49], which is not the topic of the present paper. Here, electrical conductivity is used as an additional measuring technique to judge the quality of the films. In order to obtain reproducible and meaningful results, and to be able to compare the quality of our films, electrical properties were determined under UV irradiation corresponding to the bandgap energy (370 nm). The values of the sheet resistances as well as the specific resistivities of completely processed ZnO films after the second CBD are listed in Table 2.

Table 2. Electrical properties of ZnO films.

HYA added after / min	resistivity / Ω*cm	sheet resistance / kΩ per square
0	0.09	3.1
15	0.08	1.9
30	0.29	6.4
45	0.17	2.7
no addition	0.86	11.5

Comparison of resistivities and sheet resistances of ZnO films after the second CBD. Films were grown with different addition times of HYA during the first CBD. The films were exposed to UV irradiation during the measurement.

The film prepared without addition of HYA yielded a sheet resistance of 11.5 kΩ/sq; taking into account its thickness of ca. 750 nm, a specific resistivity of 0.86 Ω*cm results. All films prepared with addition of HYA showed lower sheet resistivities than the unmodified film, regardless of the time when HYA was added. The lowest sheet resistivities with values of 1.9 and 2.7 kΩ/sq are obtained for fully processed films when HYA is added after 15 or 45 min during the first CBD. Films prepared with early addition of HYA grow much thinner, as explained in detail in 3.3. Consequently, the films grown with instant HYA addition or with addition after 15 min displayed small resistivities of 0.09 and 0.08 Ω*cm. For comparable films, i.e. undoped ZnO films prepared via CBD methods, resistivities of 0.25 Ω*cm [41] and 0.648 Ω*cm [50] have been reported for as-grown and annealed films, respectively. We therefore claim that the application of the biological additive hyaluronic acid can improve the electrical conductivities and the general quality of zinc oxide films grown in CBD processes.

4. Conclusions

This study describes a three-step deposition process of ZnO films in solution at low temperature. The process consists of a seeding and two subsequent CBD steps. During the first CBD step hyaluronic acid –

a natural polysaccharide – is added. The moment of the addition strongly influences the morphology of the deposited ZnO. It can be tailored from individual rods to finer structures, consisting of bundles of rods. HYA suppresses the ZnO growth perpendicular to the support but enhances the lateral deposition of ZnO. In general, the earlier HYA is added in the first CBD, the finer the crystallites are and the denser and thinner the films grow. The films grown under the influence of HYA in the first CBD were used as supports in a third step, an additional CBD process where the films were "sealed". The film thickness and the degree of intergrowth after this CBD step strongly depend on the morphology of the support obtained after the first CBD. In general, films which are denser and more finely structured after the first CBD lead to thinner and more strongly intergrown layers in the final CBD. Both findings can be traced back to the availability of more nucleation sites on a finer structured and denser support.

Fully processed ZnO films deposited under the influence of HYA show significantly lower film sheet resistances and specific resistivities compared with ZnO films prepared without additives. These lower resistivities are most probably a result of enhanced crystal domain intergrowth caused by mediation of the deposition by hyaluronic acid. The introduction of this naturally occurring polysaccharide thus enhances the quality of chemical bath-deposited zinc oxide films.

References

[1] X. Wang, J. Song, J. Liu, Z.L. Wang, Science 316 (2007) 102-105.

[2] P.X. Gao, J. Song, J. Liu, Z.L. Wang, Adv. Mater. 19 (2007) 67-72.

[3] R.G. Gordon, Mater. Res. Bull. 25 (2000) 52-57.

[4] F. Lu, W. Cai, Y. Zhang, Adv. Funct. Mater. 18 (2008) 1047-1056.

[5] Q. Wan, T.H. Wang, J.C. Zhao, Appl. Phys. Let. 87 (2005) 083105.

[6] J. Kim, K. Yong, J. Phys. Chem. 115 (2011) 7218-7224.

[7] J. Huang, Y. Wu, C. Gu, M. Zhai, Y. Sun, J. Liu Liu, Sensors Actuators 115 (2011) 126-133.

[8] Y. Qiu, S. Yang, Adv. Mater. 17 (2007) 1345-1352.

[9] T. Minami, Thin Solid Films 516 (2008) 5822-5828.

[10] T. Minima, Thin Solid Films 516 (2008) 1314-1321.

[11] X.W. Sun, H.S. Kwok, J. Appl. Phys. 86 (1999) 408-411.

[12] H. Deng, J.J. Russell, R.N. Lamb, B. Jiang, Y. Li, X.Y. Zhou, Thin Solid Films 458 (2004) 43-46.

[13] T.M. Barnes, J. Leaf, C. Fry, C.A. Wolden, J. Cryst. Growth 274 (2005) 412-417.

[14] J.-H. Lee, B.-O. Park, Thin Solid Films 426 (2003) 94-99.

[15] G.J. Lee, S.-K. Min, C.-H. Oh, Y. Lee, H. Lim, H. Cheong, H.J. Nam, C.K. Hwangbi, S.-K. Min, S.-H. Han, J. Nanosci. Nanotechnol. 11 (2011) 511-517.

[16] K. Govender, D.S. Boyle, P.B. Kenway, P. O'Brien, J. Mater. Chem. 14 (2004) 25752591.

[17] S.-H. Yi, S.-K. Choi, J.-M. Jang, J.-A. Kim, W.-G. Jung, J. Colloid Interface Sci. 313 (2007) 705-710.

[18] P. O'Brien, T. Saeed, J. Knowles, J. Mater. Chem. 6 (1996) 1135-1139.

[19] M.H. Huang, S. Mao, H. Feick, H. Yan, Y. Wu, H. Kind, E. Weber, R. Russo, P. Yang, Science 292 (2001) 1897-1899.

[20] A. Janotti, C.G. van de Walle, Rep. Prog. Phys. 72 (2009) 126501.

[21] R. Chandramohan, J. Thirumalai, T.A. Vijayan, S. Valanarasu, S.E. Vizhian, M. Srikanth, V. Swaminathan, Adv. Sci. Lett. 3 (2010) 319-322.

[22] F. Barka-Bouaifel, B. Sieber, N. Bezzi, J. Benner, P. Roussel, L. Boussekey, S. Szunerits, R. Boukherroub, J. Mater. Chem. 21 (2011) 10982-10989.

[23] A.E. Rakhshani, J. Phys. D: Appl. Phys. 41 (2008) 015305.

[24] M. Izaki, J. Katayama, J. Electrochem Soc. 147 (2000) 210-213.

[25] C.-H. Hsu, W.-S. Chen, C.-H. Lai, S.-F. Yan, Adv. Mater. Res. 194-196 (2011) 2254-2258.

[26] J. Lang, Q. Han, C. Li, J. Yang, X. Li, L. Yang, D. Wang, H. Zhai, M. Gao, Y. Zhang, X. Liu, M. Wei, Appl. Surf. Sci. 256 (2010) 3365-3368.

[27] C.-H. Hsu, D.-H. Chen, Nanotechnol. 21 (2010) 285603.

[28] A.T. Shishiyanu, O.I. Lupan, E.V. Monaico, V.V. Ursaki, T.S. Shishiyanu, I.M. Tiginyanu, Thin Solid Films 488 (2005) 15-19.

[29] J.T. Chen, J. Wang, R.F. Zhuo, D. Yan, J.J. Feng, F. Zhang, P.X. Yan, Appl. Surf. Sci. 255 (2009) 3959-3964.

[30] K.M. McPeak, T.P. Le, N.G. Britton, Z.S. Nickolov, Y.A. Elabd, J.B. Baxter, Langmuir 27 (2011) 3672-3677.

[31] Z.R. Tian, J.A. Voigt, J. Liu, B. McKenzie, M.J. McDermott, M.A. Rodriguez, H. Konishi, H. Xu, Nat. Mater. 2 (2003) 821-826.

[32] H. Wagata, N. Ohashi, T. Taniguchi, K.-I. Katsumata, K. Okada, N. Matsushita, Cryst. Grow. Des. 10 (2010) 4968-4975.

[33] Q. Wu, X. Chen, P. Zhang, Y. Han, X. Chen, Y. Yan, S. Li, Cryst. Growth Des. 8 (2008) 3010-3018.

[34] S.F.Wei, J.S. Lian, Q. Jiang, Appl. Surf. Sci. 255 (2009) 6978-6984.

[35] J. Liang, S. Bai, Y. Zhang, M. Li, W. Yu, Y. Qian, J. Phys. Chem. C 111 (2007) 1113-1118.

[36] M. Raula, M.H. Rashid, T.K. Paira, E. Dinda, T.K. Mandal, Langmuir 26 (2010) 8769-8782.

[37] T. Zhang, W. Dong, M. Keeter-Brewer, S. Konar, R.N. Njabon, Z.R. Tian, J. Am. Chem. Soc. 128 (2006) 10960-10968.

[38] H.-P. Cong, S.-H. Yu, Adv. Func. Mater. 17 (2007) 1814-1820.

[39] F. Waltz, G. Wißmann, J. Lippke, A.M. Schneider, H.-C. Schwarz, A. Feldhoff, S. Eiden, P. Behrens, Cryst. Growth Des. [unpublished results]

[40] L.E. Greene, M. Law, D.H. Tan, M. Montano, J. Goldberger, G. Somorjai, P. Yang, Nano Lett. 5 (2005) 1231-1236.

[41] J.B. Baxter, C.A. Schmuttenmaer, J. Phys. Chem. B 110 (2006) 25229-25239.

[42] D. Chu, T. Hamada, K. Kato, Y. Masuda, phys. status solidi A 206 (2009) 718-723.

[43] A.-J. Wang, Q.-C. Liao, J.-J. Feng, P.-P. Zhang, A.-Q. Li, J.-J. Wang, Cryst. Eng. Comm. 14, (2012) 256-263.

[44] D. Mumalo-Djokic, W.B. Stern, A. Taubert, Cryst. Growth Des. 8 (2008) 330-335.

[45] JCPDS (Joined Committee on Powder Diffraction Standards)-ICPP (International Center for Diffraction Data) (1997) Card No. 36-1451.

[46] Y. Wang, Z. Liao, G. She, L. Mu, D. Chen, W. Shi, Appl. Phys. Lett. 98 (2011) 203108.

[47] T. Minami, T. Yamamoto, T. Miyata, Thin Solid Films 366 (2000) 63-68.

[48] H. Agura, A. Suzuki, T. Matsushita, T. Aoki, M. Okuda, Thin Solid Films 445 (2003) 263-267.

[49] H.T. Cao, Z.L. Pei, J. Gong, C. Sun, R.F. Huang, L.S. Wen Surf. Coat. Technol. 184 (2004) 84-92.

[50] H. Khallaf, G. Chai, O. Lupan, H. Heinrich, S. Park, A. Schulte, L. Chow, J. Phys. D: Appl. Phys. 42 (2009) 135304.

6 Conclusions and Outlook

Within the last decades, there has been an emerging interest of science and industry in nanotechnology. This work contributes to this field, investigating nanocrystalline and nano-structured films of different materials and for different purposes.

The first part of this thesis deals with the corrosion protection of magnesium – an old material, which is nowadays reconsidered for medical and construction purposes due to its superior biocompatibility and weight, respectively. Fast corrosion was and still is a major issue in magnesium applications. Different coating techniques are well-established and provide sufficient corrosion protection, but have some disadvantages, for example, often toxic elements are used. Coating techniques are usually applied in a subsequent step after manufacturing.[25] Here, we have presented a technique which combines manufacturing (in this case joining) and coating processes in one step. Such a combination can be very beneficial, as the exposure time of the most susceptible part of the workpiece to a corrosive surrounding is minimized. In the article presented in chapter 3, we address the combination of joining and coating using a new approach. We show that by applying a nanocrystalline film of MgF_2 on magnesium weld seams, the corrosion can be remarkably reduced. However, joining and coating in this study were performed in two separate process steps due to the fact that the construction of the hybrid tool had not been completed. Recently, we have performed a true test of the hybrid apparatus with simultaneous joining and coating. It became apparent that process parameters have to be chosen very carefully. For example, if the plasma torch operates too close to the substrate, the magnesium workpiece ignites. Short working distances, however, are necessary for simultaneous welding. Nevertheless, first tests could be successfully completed and resulted in welded and coated specimens. The corrosion properties of these hybrid-processed workpieces remain to be investigated. In the article the corrosion performance of the MgF_2-coated joint was only evaluated via potentiodynamic polarization measurements. Potentiodynamic polarization is frequently used for estimation of corrosion performances.[184-186]

---

184) Witte F, Fischer J, Nellesen J, Crostack H-A, Kaese V, Pisch A, Beckmann F, Windhagen H, *Biomater.* **2006**, *27*, 1013-1018.

185) da Conceicao TF, Scharnagl N, Blawert C, Dietzel W, Kainer KU, *Thin Solid Films* **2010**, *518*, 5209-5218.

186) Yan T, Tan L, Xiong D, Liu X, Zhang B, Yang K, *Mater. Sci. Eng. C* **2010**, *30*, 740-748.

However, there may be a systematic error as it underestimates the real corrosion rate of magnesium.[187,188] For this reason, additional corrosion tests based on the determination of mass losses or hydrogen evolution should be performed in the future. Another issue is the long-term stability of the coating. For applications such as in automobiles, the reliability of the coating is crucial. Therefore, additional investigations on coating adhesion and hardness have to be performed. Furthermore, coatings produced by this hybrid process have to compete with well-established processes such as Anomag or Magoxid.[25] Additionally, plasma spraying is an expensive process regarding equipment cost and is thus mainly used for high-value products such as turbine blades in aircrafts.[26] In addition, plasma spraying with the use of liquid feedstock is not yet established in industry. These circumstances result in the rather sobering conclusion that anti-corrosive coatings produced by SPS most probably will not reach marketability within the next years. However, coatings on magnesium could be used for niche applications, such as temporary medical implants. Studies showed that the corrosion rate of magnesium alloys *in vitro* and *in vivo* can be decreased by an MgF_2 layer produced by simple immersion in HF solution.[185,189] Furthermore, Lellouche and co-workers demonstrated that nanocrystalline MgF_2 coatings show an antibacterial effect which again could be beneficial for medical applications such as sterile surgical instruments.[45] Taken together, within the first part of this thesis, the feasibility of using a nanocrystalline MgF_2 suspension in an SPS process and thus producing corrosion-retarding coatings on magnesium was demonstrated.

The second part of this thesis deals with the morphology control of ZnO precipitates as well as of ZnO films via addition of polysaccharides. Similar to the reconsideration of magnesium, ZnO undergoes a revival nowadays which is caused by a huge variety of interesting properties. Of interest here is primarily the combination of transparency and conductivity. The properties of ZnO are linked to its size and morphology.[7,140] The first publication within this part addresses the morphology control of ZnO precipitates via addition of the natural polysaccharides hyaluronic acid and chondroitin-6-sulfate.

187) Shi Z, Atrens A, *Corros. Sci.* **2011**, *53*, 226-246.
188) Shi Z, Liu M, Atrens A, *Corros. Sci.* **2010**, *52*, 579-588.
189) Witte F, Fischer J, Nellesen J, Vogt C, Vogt J, Donath T, Beckmann F, *Acta Biomaterialia* **2010**, *6*, 1792-1799.

Additives have frequently been used to tailor the morphology of ZnO.[161,165,172,190-192] When additives are supplied, the growth mechanism of ZnO often differs from "classical" crystallization theory and can be described as a controlled alignment of sub-micrometer sub-units to highly ordered mesocrystals.[193] Such mesocrystal formation was also observed in this study. Both employed polysaccharides yielded in the formation of different mesocrystal morphologies. The origin of those morphologies could be attributed to subtle differences in the structure of the PSs, and hence diverging interactions with ZnO. Whereas chondroitin-6-suflate strongly suppresses the c axis growth of ZnO leading to platelet-like sub-units, hyaluronic acid (HYA) does not show such a strong suppressing effect and leads to the formation of ZnO rods.

The second publication in this part addresses the chemical bath deposition (CBD) of thin ZnO films for applications as a transparent conductor. Again, HYA was employed to tailor the morphology of ZnO. In general, HYA addition leads to more intergrown ZnO films, compared to films produced without addition of HYA. By optimizing the time point of HYA addition to the bath solution, the sheet resistances of the resulting films could be enhanced by almost one order of magnitude without affecting the optical transparency. Although the obtained conductivities could be enhanced by HYA addition, they still did not fit the requirements for TCO applications, especially considering the fact that the low resistivities could only be observed when the films were irradiated with light. Unfortunately, resistivity measurements are a general problem in scientific articles about solution based growth of ZnO films. Often, the conditions under which the electrical properties were measured are not given precisely.[129,133,140,153,194,195] However, this is crucial as the conductivity of ZnO is strongly influenced by light irradiation. Hans-Christoph Schwarz investigated this effect in his diploma thesis and found that low resistivities induced by light can persist for several hours in the dark.[196] Therefore, film resistivities in this work were measured under constant UV light irradiation to guarantee reproducibility and comparability.

190) Liu X, Afzaal M, Ramasamy K, O'Brien P, Akhtar J, *J. Am. Chem. Soc.* **2009**, *131*, 15106-15107.

191) Cong H-P, Yu S-H, *Adv. Funct. Mater.* **2007**, *17*, 1814-1820.

192) Wu Q, Chen X, Zhang P, Han Y, Chen X, Yan Y, Li S, *Cryst. Growth Des.* **2008**, *8*, 3010-3018

193) Song RQ, Cölfen H, *Adv. Mater.* **2010**, *22*, 1301-1330.

194) Rakhshani AE, *J. Phys. D: Appl. Phys.* **2008**, *41*, 015305.

195) Khallaf H, Chai G, Lupan O, Heinrich H, Park S, Schulte A, Chow L, *J. Phys. D: Appl. Phys.* **2009**, *42*, 135304.

196) Schwarz H-C, Diploma Thesis **2011**, Leibniz University Hannover.

For application as a TCO, ZnO films are usually doped to enhance the conductivity and to make the conductivity more consistent. This has also been reported for ZnO films grown via CBD.[139,153-155,157] However, the analytical proof for successful incorporation of the dopants in the ZnO host often seems to be questionable, and it is not clear whether the conductivities were measured on samples which had been stored for sufficient long times in the dark. These issues are currently further being followed by Hans-Christoph Schwarz within his doctoral thesis work and within the BMBF project Carbofilm. When we tried to reproduce results where enhanced conductivities were observed due to doping or some kind of post-treatment, this was not possible when conductivities were consequently measured in the dark. This raises the question whether doping of ZnO during CBD is possible at all. ZnO film deposition via CBD is a complex interplay of solubilities and stabilities of Zn(II) species in solution. Here, dopant ions such as Al(III) most probably display different stabilities and thus can precipitate in bulk or remain in solution as stable complexes.[125] Furthermore, CBD is a slow equilibrium process where dopant atoms which have become incorporated into the solid can easily redissolve and thus defect-free crystals can grow.

Another issue for advanced applications of ZnO films is the durability of ZnO films applied on flexible substrates. It has become apparent that ZnO films do not sustain upon application of a soft bending stress to the films.

Within the above-mentioned BMBF-funded project Carbofilm, Hans-Christoph Schwarz attends to incorporate carbon nanotubes (CNTs) into ZnO films via CBD. This promising approach attempts to combine the excellent conductivity and mechanical properties of CNTs with the optical transparency of ZnO films. Taken together, ZnO films deposited with CBD are a promising alternative to TCO films produced by expensive physical methods. However, doping of these films still has to be achieved for application as TCO which appears to be a challenging task. Nevertheless, structured ZnO films also have potential in applications such as sensors and catalysis due to their enormous surface areas.

From a more general point-of-view, this thesis has shown that the tailored synthesis of inorganic nanoparticles and the preparation of nanostructured thin films via different methods can lead to very interesting material properties. Importantly, even in approaches which are strongly related to engineering (as anticorrosion coatings based on suspension plasma spraying) or physics (as the electrical conductivity of semiconducting films), chemistry plays an important role.

7 Curriculum Vitae

Florian Waltz
Waldstr. 28
30163 Hannover

Date of birth	January 19, 1983
Place of birth	Hildesheim, Germany
Nationality	German
Focus	crystalline inorganic nanoparticles; transparent conductive films

Education

Since September 2008	**Dissertation** Institute of Inorganic Chemistry, Leibniz University Hannover, Prof. Dr. Peter Behrens' group
October 2003 – August 2008	**Study** of Chemistry (Diplom) Achieve of Diploma in August 2008 Final grade: magna cum laude Diploma thesis: „*Synthese und Charakterisierung von Nanopartikeln*" Institute of Inorganic Chemistry, Leibniz University Hannover, Prof. Dr. Peter Behrens' group
July 2002 – September 2003	**Basic military service**
August 1995 – June 2002	**Gymnasium [high school]** Sarstedt general qualification for university entrance
August 1993 – August 1995	**Middle school** Harsum
August 1989 – August 1993	**Elementary school** Lühnde

List of Publications

Original research articles and book sections
(*The publications marked with an asterisk are part of this thesis)

Morphology Control of Zinc Oxide Films via Polysaccharide-Mediated Low-Temperature Chemical Bath Deposition
Florian Waltz, Hans-Christoph Schwarz, Andreas M. Schneider, Stefanie Eiden, Peter Behrens
Submitted to *Thin Solid Films.**

Evolution of the Morphologies of Zinc Oxide Mesocrystals Under the Influence of Natural Polysaccharides
Florian Waltz, Gesa Wißmann, Jann Lippke, Andreas M. Schneider, Armin Feldhoff, Hans-Christoph Schwarz, Stefanie Eiden, Peter Behrens
Cryst. Growth Des. **2012**, *12*, 3066-3075.*

Synthesis of Highly Stable Magnesium Fluoride Suspensions and Their Application in the Corrosion Protection of a Magnesium Alloy
Florian Waltz, Mark A. Swider, Petra Hoyer, Thomas Hassel, Martin Erne, Kai Möhwald, Matthias Adlung, Armin Feldhoff, Claudia Wickleder, Friedrich-Wilhelm Bach, Peter Behrens
J. Mater. Sci. **2011**, *47*, 176-183.*

Modulated Synthesis of Zr-Based Metal-Organic Frameworks: From Nano to Single Crystals
Andreas Schaate, Pascal Roy, Adelheid Godt, Jann Lippke, **Florian Waltz**, Michael Wiebcke, Peter Behrens
Chem. Eur. J. **2011**, *17*, 6643-6651.

Protection of Magnesium Welds by the Combination of TIG Welding with a Simultaneous Suspension Plasma Spraying Process for the Application of Nanoscaled Magnesium Fluoride Layers to Prevent Corrosion
Thomas Hassel, Mark A. Swider, **Florian Waltz**, Kai Möhwald, Friedrich-Wilhelm Bach, Peter Behrens
Magnesium, 8th International Conference on Magnesium Alloys and their Applications,
Wiley VCH **2009**, 872-878; ISBN-10**:** 3527327320.

Synthesis, characterization, and evaluation of lubrication properties of composites of ordered mesoporous carbons and luminescent CePO$_4$:Tb nanocrystals
Falk Heinroth, Dominic Gruss, Sven Müller, **Florian Waltz**, Julia Martynczuk, Armin Feldhoff , Peter Behrens, Michael Wiebcke
J. Mater. Sci. **2009**, *45*, 1595-1603.

Luminescent CeF$_3$:Eu and CePO$_4$:Tb nanocrystals and composite materials with mesoporous carbon CMK-3
Falk Heinroth, **Florian Waltz**, Michael Wiebcke, Peter Behrens
Z. Anorg. Allg. Chem. **2008**, *634*, 2045.

Other articles

Nanokristallines Magnesiumfluorid: Ein Hightech-Korrosionsschutz für Magnesium
Friedrich-Wilhelm Bach, Peter Behrens, **Florian Waltz**, Mark A. Swider, Thomas Hassel
Unimagazin Leibniz Universität Hannover **2011**, *1/2*, 48-51.

Patents

Nasschemisches Verfahren zur Herstellung leitfähiger Beschichtungen basierend auf transparenten leitfähigen Oxiden
Behrens P, Schneider AM, **Waltz F**, patent application submitted to the European patent office on Oct. 23, **2011**.

Oral presentations

Joining and coating by the combination of welding and plasma spraying to define metallurgical conditions and to produce protective layers with powder and nanoscale materials
Mark A. Swider, **Florian Waltz**, Petra Hoyer, Thomas Hassel, Martin Erne, Kai Möhwald, Peter Behrens, Friedrich-Wilhelm Bach
2nd International Symposium on Functional Surfaces, Sept. 14-15, **2011**, Aachen.

From Magnesium Fluoride Suspensions to Corrosion Resistant Magnesium Welded Seams
Florian Waltz , Mark A. Swider, Petra Hoyer, Thomas Hassel , Martin Erne, Kai Möhwald, Matthias Adlung, Armin Feldhoff , Claudia Wickleder, Friedrich-Wilhelm Bach, Peter Behrens
Nanoday, Sept. 30, **2010**, Hannover.

Protection of Magnesium Welds by the Combination of TIG Welding with a Simultaneous SPS Process for the Application of Nanoscaled Magnesium Fluoride Layers to Prevent Corrosion
Thomas Hassel, Mark A. Swider, **Florian Waltz**, Kai Möhwald, Friedrich-Wilhelm Bach, Peter Behrens
8th International Conference on Magnesium Alloys and their Applications, Oct. 25-28, **2009**, Weimar.

Posters

Carbofilm – Development of Conductive Transparent and Flexible Composite Materials
Hans-Christoph Schwarz, Carsten Benecke, Stefanie Eiden, Thilo Reusch, Bibin T. Anto, **Florian Waltz**, Andreas M. Schneider, Peter Behrens
Inno.CNT **2012**, Bayreuth.

Nanoparticles and Aggregates of Zinc Oxide Grown Under the Influence of Natural Polysaccharides
Florian Waltz, Hans-Christoph Schwarz, Gesa Wißmann, Jann Lippke, Andreas M. Schneider, Peter Behrens
Nanoday **2011**, Hannover.

Carbofilm – Development of Conductive Transparent and Flexible Composite Materials
Peter Behrens, Carsten Benecke, Stefanie Eiden, Thilo Reusch, Andreas M. Schneider, **Florian Waltz**
Inno.CNT **2011**, Ettlingen.

Preparation of Dense Sodalite Layers on Top of Alumina Supported Silicalite-1 Membranes
Imke Bremer, Simon Münzer, Florian Waltz, Jürgen Caro, Peter Behrens
5th International Zeolite Membrane Meeting **2010**, Loutraki.

Preparation of Dense Sodalite Layers on Top of Alumina Supported Silicalite-1 Membranes
Imke Bremer, Simon Münzer, **Florian Waltz**, Jürgen Caro, Peter Behrens
Deutsche Zeolith-Tagung **2010**, München.

Synthesis of Nanocrystalline Magnesium Fluoride and its Application in the TIG Welding Process to Prevent Corrosion
Florian Waltz, Mark A. Swider, Thomas Hassel, Kai Möhwald, Friedrich-Wilhelm Bach, Peter Behrens
Nanoday **2009**, Hannover
The poster was acknowledged with the LNQE poster award.

Luminescent CeF_3:Eu and $CePO_4$:Tb nanocrystals and composite materials with mesoporous carbon CMK-3
Falk Heinroth, **Florian Waltz**, Michael Wiebcke, Peter Behrens
Festkörpertagung **2008**, Bayreuth.

8 Appendix
8.1 Supporting Information to chapter 4

Supporting Material:

Evolution of the Morphologies of Zinc Oxide Mesocrystals Under the Influence of Natural Polysaccharides

Florian Waltz,[1,3] Gesa Wißmann,[1,3] Jann Lippke,[1,3] Andreas M. Schneider,[1,3] Hans-Christoph Schwarz,[1,3] Armin Feldhoff,[2,3] Stefanie Eiden,[4] Peter Behrens*[1,3]

[1]Leibniz Universität Hannover, Institut für Anorganische Chemie, Callinstr. 9, 30167 Hannover, Germany [2]Leibniz Universität Hannover, Institut für Physikalische Chemie und Elektrochemie, Callinstr. 3A, 30167 Hannover, Germany [3]ZFM-Center for Solid-State Chemistry and New Materials, Leibniz Universität Hannover, Germany [4]Bayer Technology Services GmbH, 51368 Leverkusen, Germany

Figure S1. Zeta-potential vs. pH value graph from aqueous HYA and C6S solutions.

Figure S2. Thermogravimetric data of ZnO-HYA (red curve) and ZnO-C6S (blue curve) both with (1/16):1 after 300 min of reaction. The mass loss up to 1000 °C, approx. 5 and 8%, can be stated to the decomposition of the organic additives.
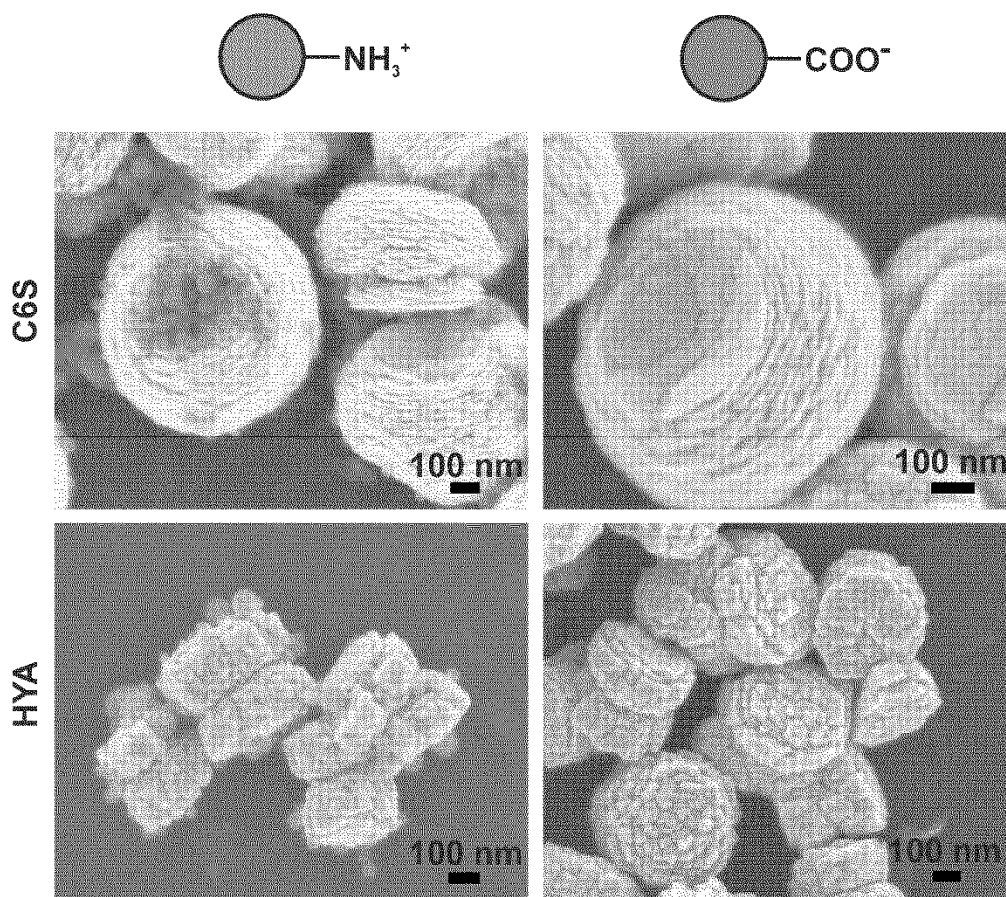
Figure S3. SEM micrographs of C6S-ZnO and HYA-ZnO after 1440 min reaction time and prepared with a (1/4):1 ratio. Prior to the SEM investigations, superstructures were stained according to the following protocol: 200 µL of a 2.5 wt.-% suspension of latex beads, either carboxyl- or amine-functionalized (Sigma-Aldrich), were suspended in 5 mL solution with defined pH values. Zeta-potential measurements showed +56 mV for amine-functionalized latex beads in a pH 3.2 solution and –63 mV for carboxyl-functionalized latex beads at pH 10.9. The corresponding PS-ZnO powder material was dispersed in 2 mL of the above mentioned suspensions by short ultrasonication; afterwards the material was separated by centrifugation. The received powder materials were again dispersed in 5 mL micro-pore filtered water and separately dropped on carbon blocks for the SEM investigation. Only the positive latex beads adsorbed on the PS-ZnO superstructures, indicating that these are negatively charged on the outside.
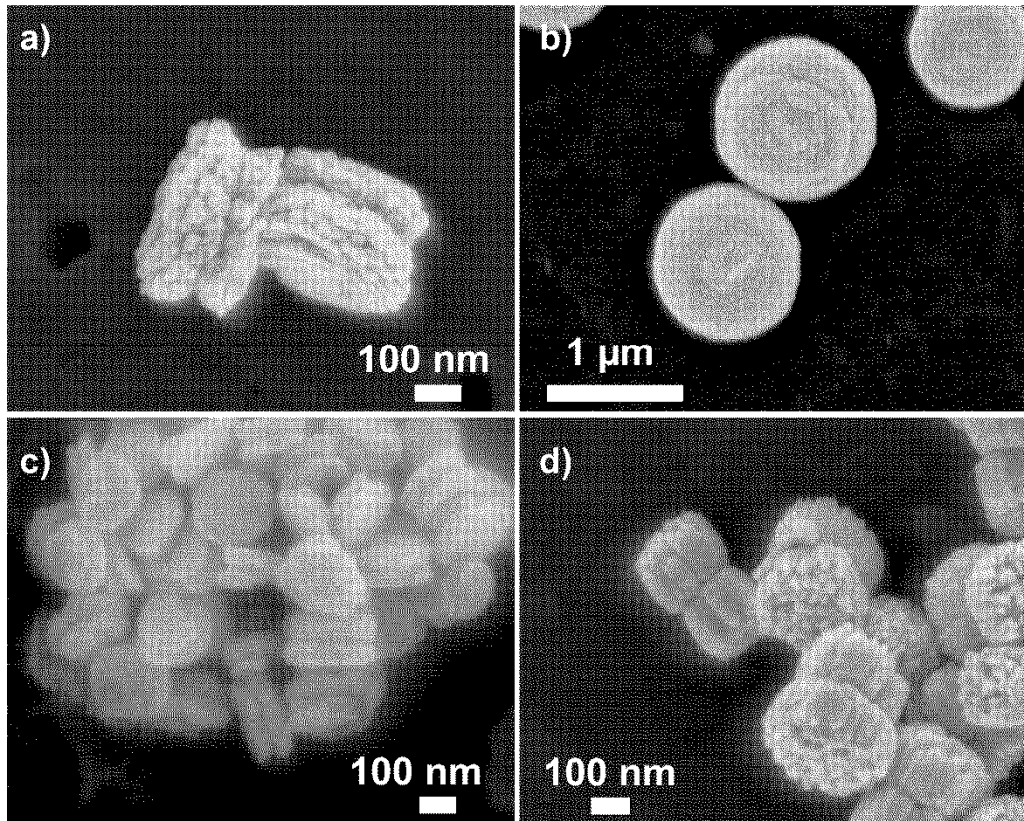
Figure S4: SEM micrographs of zincite superstructures grown under different conditions: a) with HYA (10-50 kDa molecular weight, GfN GmbH, Germany) (1/8):1 for 300 min; b) with C6S (~20 kDa) (1/8):1 for 300 min; c) with HYA (~1600 kDa) (1/4):1 for 30 min; d) with HYA (~1600 kDa) (1/8):1 for 300 min).
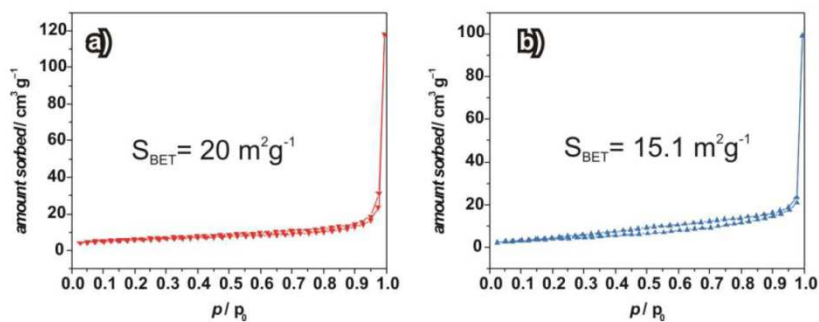
Figure S5. Nitrogen @ 77 K physisorption characteristics of ZnO-HYA a) and ZnO-C6S b); both samples obtained with PS:Zn ratio of (1/4):1 and after 300 min of reaction time.
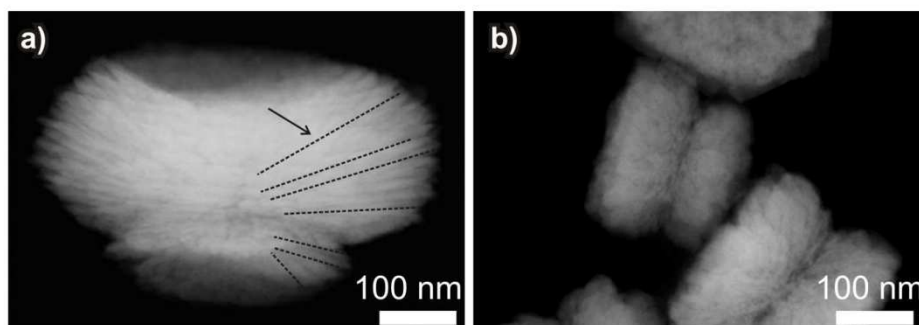

Figure S6: STEM micrographs of a) C6S-ZnO and b) HYA-ZnO superstructures grown for 180 min with PS:Zn ration of (1/4):1. The dotted lines in a) mark the orientation of the platelet-like zincite sub-units.

Figure S7: FE-SEM micrographs of zincite superstructures grown for 300 min in a mixed poly-sugar experiment. Both PSs were added in a HYA:C6S:Zn(II) ratio of (1/8):(1/8):1 and (1/16):(1/16):1, respectively.
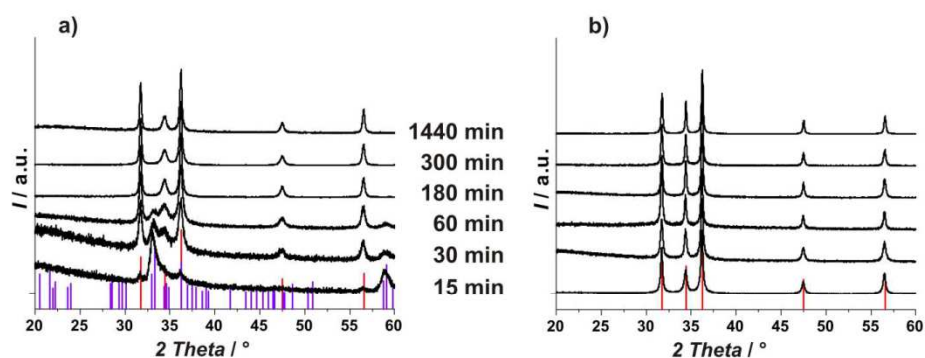

Figure S8: Ex-situ PXRD patterns taken from PS:Zn (1/4):1samples; a) C6S, b) HYA.
Red bars correspond to zincite (JCPDS # 36-1451), violet bars correspond to zinc nitrate hydroxide (JCPDS # 25-1028).